4-2016

Axonal transport and life cycle of mitochondria in Parkinson's disease model

Hyun Sung
Purdue University

Graduate School Form
30 Updated 12/26/2015

PURDUE UNIVERSITY
GRADUATE SCHOOL
Thesis/Dissertation Acceptance

This is to certify that the thesis/dissertation prepared

By Hyun Sung

Entitled

Axonal Transport and Life Cycle of Mitochondria in Parkinson's Disease Model

For the degree of Doctor of Philosophy

Is approved by the final examining committee:

Henry C. Chang
Chair

Peter J. Hollenbeck

Daniel Suter

Jean-Christophe Rochet

To the best of my knowledge and as understood by the student in the Thesis/Dissertation Agreement, Publication Delay, and Certification Disclaimer (Graduate School Form 32), this thesis/dissertation adheres to the provisions of Purdue University's "Policy of Integrity in Research" and the use of copyright material.

Approved by Major Professor(s): Peter J. Hollenbeck

Approved by: Richard J. Kuhn 4/12/2016

Head of the Departmental Graduate Program Date

AXONAL TRANSPORT AND LIFE CYCLE OF MITOCHONDRIA IN PARKINSON'S DISEASE MODEL

A Dissertation

Submitted to the Faculty

of

Purdue University

by

Hyun Sung

In Partial Fulfillment of the

Requirements for the Degree

of

Doctor of Philosophy

May 2016

Purdue University

West Lafayette, Indiana

ACKNOWLEDGEMENTS

I would like to express my thanks to my advisor, Dr. Peter Hollenbeck for his guidance and support throughout my Ph.D. study. Without his encouragement and motivation with his great effort to supervise me, I could not imagine how I accomplish my research and this thesis. I believe that his enthusiasm, immense knowledge and patience guide me tremendously as a graduate student and as a scientist. I also express my appreciation to my thesis committee members, Dr. Daniel Suter, Dr. Henry Chang, Dr. Chris Rochet and Dr. James Clemens for their insightful comments, suggestions and thoughtful feedback. I would like to thank the past and current Hollenbeck lab members, Swathi Devireddy, Pin-Chao Liao, Elisabeth Garland-Kuntz and Doris Kemler for their support and companionship as great lab members. I also would like to thank all the undergraduate students who were/are in Hollenbeck lab including Kenny Nguyen, Lauren Tandarich, Mazz Arif and Alex Liu, and thank all Suter lab members for their opened research discussion.

Many thanks go to my friends inside and outside of Purdue. I would like to thank members in PKLSG (Purdue Korean Life Sciences Group) and KPCP (Korean Presbyterian Church of Purdue) who enhance and shine my life at Purdue.

Last but not least, my greatest thanks go to my family who always give me the best love. I appreciate the endless love and prayer from my parents and my sister. I also appreciate the best support and love from my parents-in-law and sister-in-law. I specially appreciate my dear son, 건, who came into my life. Above all, I am especially grateful to my wife, Yumi, who comes before anyone else to me. It was my big pleasure to meet her at Purdue. To her I dedicate this thesis.

TABLE OF CONTENTS

Page

Page

Page

Page

LIST OF TABLES

LIST OF FIGURES

LIST OF ABBREVIATIONS

ACV : Anterior crossvein

AD : Alzheimer's disease

ALS : Amyotrophic lateral sclerosis

Ant A : Antimycin A

APP : Amyloid precursor protein

Atg : Autophagy-related gene

ATP : Adenosine triphosphate

AV : Autophagic vacuole

A2 : Abdominal segment 2

A4 : Abdominal segment 4

A7 : Abdominal segment 7

CCCP : Carbonyl cyanide *m*-chlorophenylhydrazone

cm : Centimeter

CNS : Central nervous system

CO_2 : Carbon dioxide

DMSO : Dimethyl sulfoxide

DRG : Dorsal root ganglion

Drp1 : Dynamin related protein 1

ER : Endoplasmic reticulum

F_c : Cytoplasmic fluorescence

FCCP : carbonyl cyanide 4-phenylhydrazone

F_m : Mitochondrial fluorescence

F1 : 1^{st} filial generation

F2 : 2^{nd} filial generation

F3 : 3rd filial generation

HAP1 : Huntingtin-associated protein 1

HCV : Humeral crossvein

HD : Huntington's disease

HL6 : Hemolymph-like buffer

HRP : Horseradish peroxidase

HTT : Huntingtin

H_2O_2 : Hydrogen peroxide

JNK : c-Jun N-terminal kinase

kDa : Kilodalton

LSCM : Laser scanning confocal microscope

LV : Longitudinal vein

MDV : Mitochondria-derived vesicle

Mfns : Mitofusins

mito-GFP : Mitochondrially-targeted green fluorescence protein

ml : Milliliter

mm : Millimeter

mM : Millimolar

MT : Microtubule

MVB : Multi-vesicular body

M6 : Muscle 6

M7 : Muscle 7

nm : Nanometer

nM : Nanomolar

NMJ : Neuromuscular junction

Opa1 : Optic atrophy protein 1

PARL : Presenilin-associated rhomboid-like protease

PCV : Posterior crossvein

PD : Parkinson's disease

PE : Phosphatidylethanolamine

PI3P : Phosphatidylinositol 3-phosphate

QC : Quality control

RFP-atg8 : Red fluorescence protein linked with atg8

ROI : Regions of interest

ROS : Reactive oxygen species

rpm : Revolutions per minute

SN : Segmental nerve

SNPH : Syntaphilin

SOD1 : Superoxide dismutase 1

TIM : Translocase of mitochondrial inner membrane

TMRM : Tetramethylrhodamine methyl ester

Ub : Ubiquitin

VALAP : Vaseline, Lanolin and Paraffin mixture

VDAC1 : Voltage-dependent anion channel 1

VG : Ventral ganglion

$\Delta\Psi m$: Mitochondrial inner membrane potential

µg : Microgram

µl : Microliter

µm : Micrometer

µM : Micromolar

ABSTRACT

Sung, Hyun. Ph.D., Purdue University, May 2016. Axonal Transport and Life Cycle of Mitochondria in Parkinson's Disease Model. Major Professor: Peter J. Hollenbeck

In neurons, normal distribution and selective removal of mitochondria are essential for preserving compartmentalized cellular function. Parkin, an E3 ubiquitin ligase associated with familial Parkinson's disease, has been implicated in mitochondrial dynamics and removal. However, it is not clear how Parkin plays a role in mitochondrial turnover *in vivo*, and whether the mature neurons possess a compartmentalized Parkin-dependent mitochondrial life cycle. Using the live *Drosophila* nervous system, here, I investigate the involvement of Parkin in mitochondrial dynamics; organelle distribution, morphology and removal. Parkin deficient animals displayed less number of axonal mitochondria without disturbing organelle motility behaviors, morphology and metabolic state. Instead, loss of Parkin produced tubular and reticular mitochondria specifically in motor neuronal cell body. In addition, unlike in immortalized cells *in vitro*, Parkin-dependent mitophagy was rarely found in our mature neurons. Thus, my results indicate that mitochondrial morphology is restrictively modulated in the cell body in Parkin-dependent manner, and this further proposes an idea that the organelle supply from the cell body is important for the mitochondrial quality control in mature neurons.

CHAPTER 1. INTRODUCTION

1.1 Mitochondria in Neurons

Neurons are specialized cells that process and transmit information through electrochemical signals. They are electrically excitable and morphologically asymmetric, and highly differentiated to demand large amounts of ATP for the maintenance of ionic gradients across the cellular membranes and for release of neurotransmitter at synapses. Among the neuronal components, mitochondria are unique and central organelles for ATP production, intracellular Ca^{2+} homeostasis and generation of reactive oxygen species (ROS). Since these various cellular functions of mitochondria are all critical in membrane excitability and synaptic plasticity, neuronal activity and survival are significantly dependent upon mitochondrial function. As a consequence, proper maintenance of functional mitochondria and/or removal of damaged mitochondria should be understood to better comprehend the physiological behavior of neurons (Fiskum et al., 1999; Nicholls and Budd, 2000).

In neurons, mitochondria are dynamic organelles that display an intricate life cycle. They undergo constant movements (Stowers et al., 2002; Guo et al., 2005; Glater et al., 2006; Pilling et al., 2006; Reis et al., 2009), continuous shape changes (Okamoto and Shaw, 2005; Chan, 2006; Song et al., 2009) with complex biogenesis and degradation (Davis and Clayton, 1996; Amiri and Hollenbeck, 2008; Maday et al., 2012; Ashrafi et al., 2014). Though less is known about the molecular underpinnings of the mitochondrial life cycle in neurons *in vivo*, there is some recent evidence that disruptions of mitochondrial dynamics are associated with several major neurodegenerative diseases including Parkinson's disease (PD) (Palacino et al., 2004; Dodson and Guo, 2007; Gautier et al., 2008; Mortiboys et al., 2008; Wood-Kaczmar et al., 2008). Therefore,

exploring mitochondrial dynamics and life cycle is essential to understanding the complex physiological behavior of neurons, as well as the underlying pathogenesis of neurological diseases.

1.1.1 Mitochondrial axonal transport

Neurons are morphologically asymmetric and polarized cells that exhibit a dramatic example of cellular compartmentalization. Since neurons are compartmentalized into three distinct regions - the cell body, a long axon and synaptic terminal - their distinct subcellular regions are physically and functionally organized. For this reason, proper distribution and normal localization of their organelles among the somatodendritic, axonal and synaptic compartments (Hollenbeck and Saxton, 2005; Hirokawa et al., 2010; Saxton and Hollenbeck, 2012) are important for polarized neuronal functions. Mitochondria are no exception to this strategic positioning of organelles within neurons, since they serve major metabolic demands at various locations such as active growth cones, distal synapses and nodes of Ranvier (Hollenbeck and Saxton, 2005; Sheng and Cai, 2012).

In neurons, axonal transport is the major generator of organelle distribution and localization. Through axonal transport, components within neurons can move anterogradely from the cell body to the synaptic terminal and also return back retrogradely toward the cell body from the distal synaptic regions. Among the neuronal components, mitochondria are one of the categories of organelle that display saltatory and bidirectional movements, especially in the axons and dendrites (Morris and Hollenbeck, 1993; Hollenbeck, 1996). Commonly, bidirectional movements of mitochondria are thought to be associated with the place where the organelles are needed and/or degraded in neurons. Several studies provide evidence of mitochondrial transport organized to meet local demands. One example is the behavior of mitochondria in a myelinated nerve. There, mitochondrial movements are generally reduced in nodal axoplasm compared with internodal and juxtaparanodal axoplasm. Axonal electrical activity, however, increases the size of mitochondrial stationary clusters and decreases

mitochondrial motility in nodal axoplasm. Conversely, decreased axonal electrical activity increases the motile fraction of mitochondria in the node of Ranvier (Kiryu-Seo et al., 2010; Ohno et al., 2011). Since clusters of sodium channels and sodium/potassium ATPases are found at the nodes, the regions near the node of Ranvier generally have a high energy demand. Thus, these modulations of mitochondrial recruitment described above probably represent a response to axonal electrical activity and/or elevated axoplasmic calcium ion levels.

It is unsurprising that many neurodegenerative diseases are reported to involve disruptions of mitochondrial axonal transport. Impaired mitochondrial transport has been observed in hippocampal neurons exposed to amyloid β (Rui et al., 2006; Vossel et al., 2010), and mitochondrial accumulations were found in degenerated axons in patients with Alzheimer's disease (AD) (Stokin et al., 2005). In addition, neurons from patients with amyotrophic lateral sclerosis (ALS) (Sasaki and Iwata, 1996) and from mice that express ALS-related superoxide dismutase 1 (SOD1) mutantions displayed impaired mitochondrial axonal transport (De Vos et al., 2007; Shi et al., 2010). Furthermore, recent studies indicate that the impaired mitochondrial axonal transport is critically involved in the pathology of Huntington's disease (HD), since Huntingtin (HTT) plays an essential role as an integrator for intracellular vesicular trafficking, including mitochondria (Chang et al., 2006; Colin et al., 2008; Caviston and Holzbaur, 2009). Though it has not been demonstrated the direct evidences for defective mitochondrial movements in Parkinson's disease (PD), Parkin, E3 ubiquitin ligase that is associated with familial PD, is proposed to be linked with mitochondrial transport (Wang et al., 2011; Liu et al., 2012). Thus, further investigation is required to elucidate the role of mitochondrial movements in neurodegenerative diseases, such as PD.

So far, little is known about how the movements of mitochondria are closely modulated in response to regional neuronal requirements and how the motility patterns of mitochondria are altered in models of neuronal diseases. However, here, I provide an overview of the trafficking machineries that contribute to the complex nature of mitochondrial transport, and introduce five proposed models that describe how the movements of mitochondria might be regulated in neurons.

1.1.1.1 Trafficking machinery, motor proteins

It is interesting that axons contain a linear array of polarized microtubules (MTs): the plus ends of axonal MTs are arranged towards the distal tips, whereas the minus ends are directed toward the cell body. This uniform arrangement of MTs underlies distinguishable and organized bidirectional, anterograde and retrograde, movements of neuronal cargos. Like most organelles in animal cells, the axonal transport of mitochondria is mainly MT-based. There are two major motor proteins for MT-based mitochondrial movements, kinesin-1 and dynein (Figure 1.1). Conventional kinesin motors, kinesin-1 (also called kinesin heavy chain or Kif5), are responsible for the anterograde transport towards the synaptic terminal, while dynein motors are responsible for the retrograde transport towards the cell body. Since the absence of kinesin-1 and dynein dramatically disrupts the transport of mitochondria in *Drosophila* motor axons (Pilling et al., 2006), recent study clearly suggests the key role of these two major MT associated motor proteins in mitochondrial axonal transport.

Interestingly, the anterograde trafficking motor, kinesin, forms a protein complex with the mitochondrial proteins Miro and milton (Stowers et al., 2002; Guo et al., 2005; Glater et al., 2006; Reis et al., 2009). Milton is a motor adaptor protein that is associated with kinesin and linked indirectly to mitochondria through an interaction with Miro, a mitochondrial rho GTPase which is present in the mitochondrial outer membrane. Mutation of *miro* or *milton* genes in *Drosophila* caused impaired mitochondrial anterograde transport. This suggests that Miro, milton and kinesin constitute a transport system specific for the mitochondrial anterograde movement. So far, it is not clear whether Miro/milton complex is also involved in dynein-mediated retrograde mitochondrial transport. However, a recent study provides direct evidence for a biochemical interaction that TRAK1 (the mammalian homolog of milton) binds to both kinesin-1 and dynein (van Spronsen et al., 2013).

In addition to MT-based motor proteins, kinesin and dynein, syntaphilin is a well-known axonal MT associated protein that is thought to anchor mitochondria (Kang et al., 2008). Syntaphilin is located in the outer membrane of stationary axonal mitochondria and contains a MT-binding domain, so it is thought to anchor mitochondria through direct

interactions with MTs. Interestingly, deletion of the mouse *syntaphilin* resulted in an increased proportion of mobile axonal mitochondria (Kang et al., 2008). However, syntaphilin is only found in mammals. Since other model animals, such as *Drosophila*, also show a similar pattern of a stationary pool of mitochondria in axons, further studies are needed to fully understand mitochondrial anchoring mechanisms to MTs.

Generally, in axons, long-range mitochondrial transport is driven by MT-based kinesin and dynein motors, while short-range mitochondrial transport is thought to be mediated by actin-based motors (Morris and Hollenbeck, 1995). Myosin is a major motor protein that mediated mitochondrial transports with actin microfilaments. Though it remains unknown how myosins bind to mitochondria, a study in *Drosophila* neurons suggests that RNAi knockdown of myosin proteins increased run lengths and net movements of mitochondria (Pathak et al., 2010). Additionally, nerve growth factor can regulate mitochondrial transports by interactions between mitochondria and actin cytoskeleton (Chada and Hollenbeck, 2004).

1.1.1.2 Regulation of mitochondrial movement

If mitochondria move so as to supply local neuronal energy demands and to meet their own physiological purposes, the axonal transport of mitochondria ought to be closely modulated between mobile and stationary pools. In axons, mitochondria display dynamic patterns of behavior including consistent anterograde and retrograde movement with occasional reversals, stops and starts (Hollenbeck and Saxton, 2005; Saxton and Hollenbeck, 2012). So far, however, it is unknown how these movements of mitochondria, especially changes in direction and/or changes between movement and arrest, are regulated in axons. Here, I summarize five models that have been proposed for explaining the regulation of mitochondrial transport, how mitochondria are arrested.

Since syntaphilin (SNPH), which contains MT-binding domain, was observed on stationary axonal mitochondria (Kang et al., 2008), this protein has been proposed to be a static anchor for mitochondria on MT tracks (Figure 1.2, B). The time-lapse observations that visualized GFP-SNPH-labeled mitochondria showed that they remained stationary, while GFP-SNPH-negative mitochondria migrated along the axonal process. This

provided evidence of an anchoring role of syntaphilin in mitochondrial transport (Kang et al., 2008). Thus, syntaphilin is a candidate docking protein, and could play a role in how mobile axonal mitochondria are recruited to the stationary pool and arrested in local axonal sites.

Another proposed model for mitochondrial arrest is the involvement of actin microfilament associated protein, myosin (Figure 1.2, C). It is interesting that deletion of myosin V actually increased mitochondrial velocity in both directions, whereas RNAi knockdown of myosin VI specifically increased retrograde transport of mitochondria (Pathak et al., 2010). This is also consistent with the result that disruption of F-actin causes faster and more persistent mitochondrial axonal transport in cultured neurons (Morris and Hollenbeck, 1995). Though the manipulations of myosin proteins seem to regulate moving mitochondria selectively, this recent study suggests that myosins may arrest moving mitochondria by docking them to the actin cytoskeleton. By analogy with organelle transport in pigment cells (Rogers and Gelfand, 1998; Nascimento et al., 2003), it is possible that myosins compete with MT-based motor proteins, such as kinesins, and inhibit the moving mitochondria on MT tracks.

As described above, the Miro/milton complex is proposed to function as an adaptor between mitochondria and motor protein kinesin. Since the amino-terminal motor domain of kinesin binds to the MT tracks, the cutting off from the one of structural linkages within this motor protein complex will cause mitochondrial arrest. In this regard, it is notable that Miro contains two EF hands with Ca^{2+} binding motifs that can rearrange this motor protein complex. One suggested model of this complex modification is that the EF hands of Miro binds with increased cytosolic Ca^{2+} and release the motors completely from mitochondria (Macaskill et al., 2009). As a consequence, this conformational change would dissociate mitochondria from the MT tracks (Figure 1.2, D). Alternatively, another proposed model in this complex modification is that the motor domain of kinesin directly binds to Miro upon increased cytosolic Ca^{2+} (Wang and Schwarz, 2009). This rearrangement of motor protein complex causes motor protein release from the MT tracks and consequently arrest mitochondria (Figure 1.2, E). These proposed models, however, are not only contradictory, but fail to explain why the manipulations of Miro by increased

Ca^{2+} disrupt not only kinesin dependent anterograde movement, but also dynein dependent retrograde movement of mitochondria.

Recently, an additional model has been proposed to explain mitochondrial arrest by the modulation of the Miro/milton/kinesin motor protein complex. In this mechanism (Figure 1.2, F), two PD related proteins, PINK1 and Parkin, are involved. Interestingly, PINK1, as a mitochondrial membrane kinase, phosphorylates Miro, which activates the proteasomal degradation of Miro by the ubiquitin ligase activity of Parkin. As a result, PINK1/Parkin dissociates the linker protein, Miro, from the milton/kinesin motor protein complex, which in turn detaches mitochondria from the MT track (Wang et al., 2011). Like the other proposed models of this complex modification, the suggested mechanism fails to clarify why the manipulations of PINK1 and Parkin disrupt mitochondrial transport in both directions, and whether PINK1/Parkin regulates mitochondrial transport broadly in other cell or tissue types. However, this proposed model is intriguing and worthy of note because of the involvement of the mitochondrial axonal transport in neurodegenerative disease.

1.1.2 Mitochondrial fission and fusion

In addition to axonal transport, mitochondria display continuous shape changes controlled by fission and fusion. Like mitochondrial transport, mitochondrial fission and fusion dynamics also can contribute to proper distribution of mitochondria within neurons. Indeed, mitochondrial fission may sequester, and mitochondrial fusion may dilute, the damaged components in mitochondrial networks to help maintain the proper function and distribution of organelles.

Many of neurological diseases are associated with the disruptions in mitochondrial fission-fusion balance. It is reported that mutations in mitochondrial fusion protein cause Charcot-Maire-Tooth type 2A, a peripheral neuropathy characterized by sensory neuronal loss and muscle defects (Zuchner et al., 2004). In addition, an imbalance of mitochondrial fission-fusion was observed upon overexpression of APP, amyloid precursor protein associated with AD, in neuronal cells (Wang et al., 2008).

Furthermore, studies from *Drosophila* have suggested that two PD related genes, PINK1 and Parkin, are also involved in regulation of mitochondrial morphology (Poole et al., 2008). Thus, maintaining mitochondrial morphological balance between fission and fusion seems to be required for preserving normal mitochondrial functions and for protecting neurodegenerative diseases, such as PD.

Although many recent studies indicate the significance of mitochondrial morphology in neurodegenerative diseases, contradictory findings have been reported in these studies (Chen and Chan, 2009): normal ultrastructure of mitochondria was found in the striatum of PINK1 deletion mice (Gautier et al., 2008), while enlarged and swollen mitochondria were found in the flight muscle of PINK1/Parkin mutant flies (Poole et al., 2008). Thus, further work is required to fully understand the role of mitochondrial fission-fusion dynamics in neurological diseases. Since mitochondria undergo a continuous cycle of fission and fusion in a regulated manner, here I summarize major proteins that regulate fission or fusion, respectively (Figure 1.3).

1.1.2.1 Mitochondrial fission

In mammalian cells, mitochondrial fission is regulated by two key proteins, Drp1 (Smirnova et al., 2001) and Fis1 (James et al., 2003). Drp1, dynamin-related protein 1, is predominantly located in the cytosol but is recruited to mitochondrial surface for organelle division by mitochondrial outer membrane protein, Fis1. Recent studies showed that inhibition of Drp1 activity causes elongated mitochondria (Pitts et al., 1999), while overexpression of Drp1 results in mitochondrial fragmentation (Arnoult et al., 2005). It was also reported that the depletion of Fis1 causes elongated mitochondria, while the overexpression of Fis1 leads to mitochondrial fragmentation (Yoon et al., 2003). Indeed, the full mitochondrial fission process mediated by Drp1 and Fis1 contains three proposed steps. First, constriction of the mitochondrial membrane occurs initially without Drp1 recruitment. Though the localization of Drp1 on mitochondrial surface is proposed to be independent of the initial constriction of the organelle, secondly, Fis1 recruits Drp1 to the scission site to further constrict the mitochondrial membrane. Finally, once mitochondrial scission is completed, Drp1 is disassembled from the daughter mitochondria (Chan, 2006)

(Figure 1.3, A). In this regard, a recent report that proposes the contribution of endoplasmic reticulum (ER) in mitochondrial division is worth noting. Since ER tubules constrict mitochondria before the Drp1 recruitment (Friedman et al., 2011), it is possible that the first step of mitochondrial division, the initial constriction of mitochondrial membrane, can be mediated by interactions with other organelles, such as ER.

1.1.2.2 Mitochondrial fusion

The detailed molecular mechanisms of mitochondrial fusion remain unclear, but studies from mammalian cells suggest that the fusion event is mediated by two major proteins: Mitofusins (Mfn1 and Mfn2) and optic atrophy protein 1 (Opa1). Mfn1 and Mfn2 are dynamin-related GTPases that are located in the outer membrane of mitochondria, while another dynamin-related GTPase, Opa1, resides in the inner membrane and/or intermembrane space of mitochondria (Okamoto and Shaw, 2005; Chan, 2006; Song et al., 2009). Recent studies indicate that mitochondria lacking either mitofusins or Opa1 cannot undergo fusion, therefore resulting in a shortened and fragmented state (Chan, 2006). Like mitochondrial fission, the fusion event is also known to require three consecutive steps: adjacent mitochondrial docking, mitochondrial outer membrane fusion and mitochondrial inner membrane fusion (Figure 1.3, B). Mitofusins are thought to play an important role in adjacent mitochondrial docking and further in the mitochondrial outer membrane fusion. Once those mitochondria are tethered by the outer membrane fusion, Opa1 is proposed to play a role in mitochondrial inner membrane fusion and further remodeling of cristae structure in newly fused mitochondria (Frezza et al., 2006).

1.1.3 Mitochondrial degradation

Since neurons are critically dependent on functional mitochondria, not only mitochondrial dynamics, axonal transport and fission-fusion, but also temporal-spatial removal of damaged mitochondria is another substantial component of the mitochondrial life cycle in neurons. Autophagy is a major catabolic process by which the cellular components including long-lived proteins and damaged organelles are degraded. During

autophagy, those cellular components are engulfed into double-membrane vesicles, autophagosomes, and then fused with lysosomes to form autolysosomes. Thereby, autophagy is proposed to play a clearing role in neurons by digesting and turning over dysfunctional cellular components, such as damaged mitochondria. “Mitophagy” denotes the degradation specifically of mitochondria through this autophagic process. Although, so far, autophagy has been well-known for its role during starvation, emerging findings have suggested an intimate link between mitophagy and age-associated neurodegeneration.

Recent evidence implicates defective mitophagy in several neurodegenerative diseases. It is reported that elevated mitochondrial ROS production was found in a model of AD pathogenesis, and the deficiency of mitochondrial complexes I and IV is associated with amyloid β accumulation (Caldwell et al., 2015; Lionaki et al., 2015). Additionally, studies in HD reveal that there is dysfunctional mitochondrial accumulation in the cytoplasm and the deficiency of autophagic recognition is also found in this disease model (Martinez-Vicente et al., 2010; Lionaki et al., 2015). Furthermore, it is notable that two PD related genes, PINK1 and Parkin, target depolarized, dysfunctional mitochondria for autophagic engulfment and degradation (Narendra et al., 2008; Matsuda et al., 2010; Narendra et al., 2010; Ashrafi et al., 2014; Lazarou et al., 2015). Although its underlying mechanism remains unclear, these findings suggest the impaired process of mitochondrial removal is significantly associated with the onset of several age-associated neurodegenerative diseases.

It is still unclear whether dysfunctional mitochondria are selectively targeted for mitophagy and where the mitophagy event happens in neurons. However, recent evidence from disease model studies suggests an obvious connection between mitophagy and mitochondrial dynamics. For example, it has been reported that the fly model of Friedreich ataxia displayed disrupted axonal transport of mitochondria with the accumulation of senescent mitochondria in their neuromuscular junctions (NMJs) (Shidara and Hollenbeck, 2010). This clearly implicates that mitochondrial movement is associated with organelle turn over system in neurons. Thus, it is worth considering how

compromised neuronal mitophagy is affected by defective mitochondrial dynamics, such as disrupted axonal transport and/or imbalance of fission-fusion.

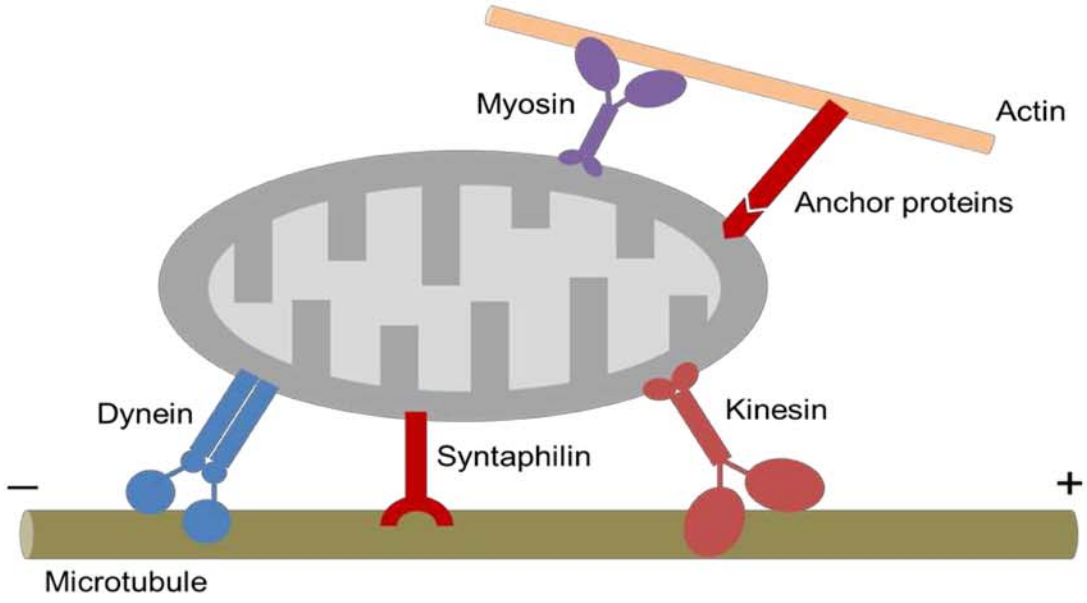

Figure 1.1 Proposed mitochondrial transport machineries, tracks, motors and docking proteins in axons. Microtubule (MT)-based motors, kinesin and dynein, modulate long-range of mitochondrial transport, anterograde and retrograde respectively. Syntaphilin anchors mitochondria through interactions with MTs. The actin-based motor, myosin, regulates short-range of mitochondrial transport and/or halts mitochondrial movements by tethering mitochondria to the axonal actin cytoskeleton. There might be unknown anchoring receptors for the subsequent stationary docking of mitochondria on actin.

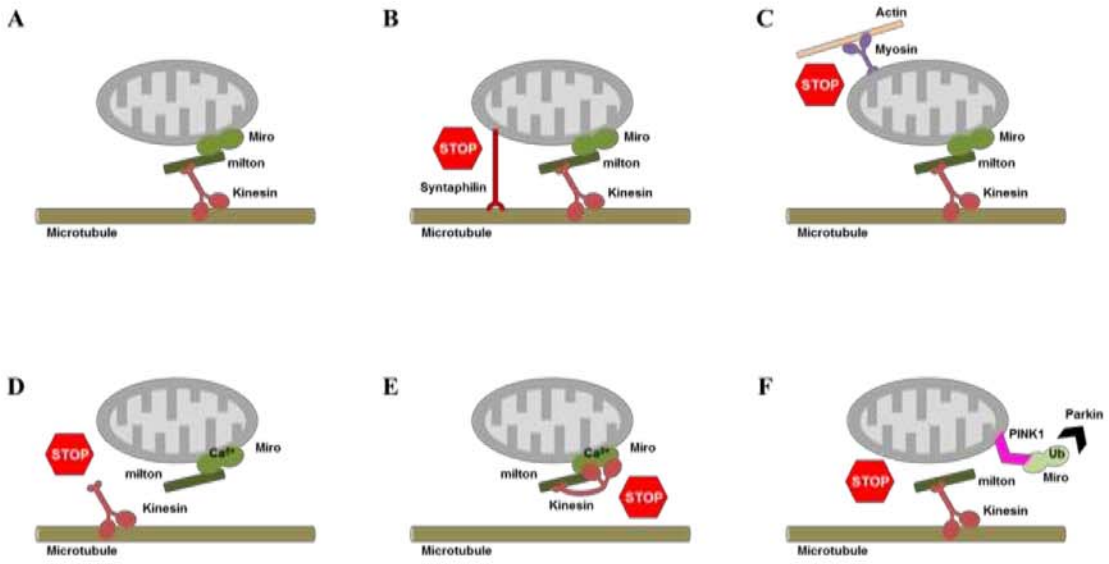

Figure 1.2 Regulation of mitochondrial movements, mitochondrial arrest. Five proposed models describe differently the way in which mitochondrial transport is controlled and arrested. (A) Anterograde moving mitochondria bear a protein complex with Miro/milton and MT-based motor protein, kinesin. (B) Syntaphilin is present on stationary axonal mitochondria and anchors them directly to the MT. (C) Myosin can inhibit mitochondrial movements by tethering them to the actin cytoskeleton. (D) Increased cytosolic Ca^{2+} binds to the EF hands of Miro that consequently release the motor completely from mitochondria, so that mitochondria are dissociated from MT. (E) Increased cytosolic Ca^{2+} binds to the EF hands of Miro that consequently causes a rearrangement of motor protein complex; the motor domain of kinesin directly binds to Miro and cannot interact with MTs, so that mitochondria are dissociated from the MT. (F) Degradation of Miro by PINK1/Parkin dissociates linker from the motor protein complex that consequently detaches kinesin from the mitochondria.

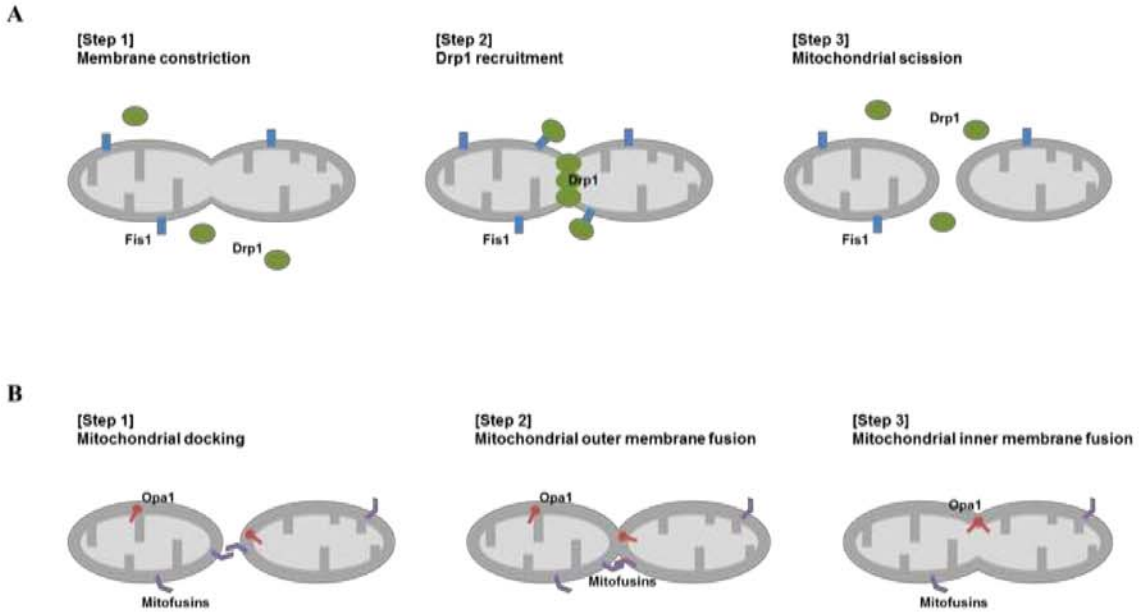

Figure 1.3 Dynamics of mitochondrial fission and fusion. Mitochondrial morphology is regulated by fission-fusion dynamics. (A) Mitochondrial fission by Drp1 and Fis1. Three steps are required for the fission event: mitochondrial membrane constriction, Drp1 recruitment and mitochondrial scission. (B) Mitochondrial fusion by mitofusins and Opa1. Three steps are proposed for the fusion event: mitochondrial docking, mitochondrial outer membrane fusion and mitochondrial inner membrane fusion.

1.2 Autophagosomes in Neurons

Autophagy, which is described as a “self-eating process”, is a conserved lysosomal degradation pathway. Mostly, autophagy has been studied in response to cellular stresses, such as starvation. However, it also reported that a basal level of autophagy is critical for neuronal survival (Hara et al., 2006; Mizushima et al., 2008). Since autophagy has been shown to be associated with various neurodegenerative diseases, recently, neurons are one of the cell types that are widely used for studying biogenesis of autophagic vacuoles, or autophagosomes (Larsen and Sulzer, 2002; Yue et al., 2009). It is reported that neuronal autophagy is reduced in a mouse model of AD, and autophagic deficiency causes amyloid β accumulation (Pickford et al., 2008; Yue et al., 2009). In addition, studies from mouse and fly suggest that autophagic induction by inhibition of mTOR reduces polyglutamine expansion toxicity and enhances mutant huntingtin clearance in HD model (Ravikumar et al., 2004; Sarkar and Rubinsztein, 2008). Although studies are still limited, these findings nonetheless suggest a physiological role for autophagy in the etiology of neurodegenerative diseases. In this context, it cannot be ignored that the two PD related genes, PINK1 and Parkin, have been proposed to target dysfunctional mitochondria for the autophagosomal engulfment.

1.2.1 Formation of autophagosome

Generally, the autophagic process has been described as occurring in three different types: macroautophagy, microautophagy and chaperone-mediated autophagy. Since macroautophagy, hereafter referred to as autophagy, can eliminate large macromolecules and entire organelles by using several cytosolic vesicles, this process is mediated by a subset of molecular machinery to sequester vesicles and to form autophagosomes (Xie and Klionsky, 2007). Studies in yeast revealed that a number of autophagy-related (Atg) genes are engaged sequentially in a highly regulated manner (Tsukada and Ohsumi, 1993; Xie and Klionsky, 2007). In detail, autophagy involves a series of steps: phagophore formation, autophagosome elongation and lysosome fusion. These steps are controlled by

functional groups of proteins (Gelino and Hansen, 2012). First, an expanding cup-shaped double-membrane structure, called phagophore, is generated to enclose and isolate the cytoplasmic components. This formation of phagophore is known to be regulated by phosphatidylinositol 3-phosphate (PI3P)-binding complex. In this step, Atg9, a transmembrane protein that has been proposed to deliver lipids to the phagophore, is distributed by PI3P-binding complex. Once membrane nucleation and phagophore formation are completed, it is known that the Atg5/Atg12/Atg16 conjugation system is involved in phagophore expansion into the double-membrane structure of the autophagosome. The Atg5/Atg12/Atg16 complex mainly resides on the outer side of phagophore and decorates the expanding phagophore. This complex then associates with the Atg8/phosphatidylethanolamine (PE) conjugation system to grow and mature the autophagosomes. Growing autophagosomes can fuse with late endosomes and/or multi-vesicular bodies (MVBs) to form hybrid organelles, called amphisomes. Lastly, the mature autophagosome that contains cargo eventually fuses with lysosome to become the autolysosome, and its cargos are degraded for recycling (Figure 1.4). During the process, most machinery proteins, except for Atg8, are gathered then released from the completed vesicle. Since Atg8 (LC3, mammalian homolog of yeast Atg8) widely associates with the autophagosomal membrane from phagophore formation through lysosomal fusion, Atg8 (LC3) is often used as an experimental marker for autophagosomes.

1.2.2 Autophagosomal axonal transport

In neurons, less is known about the biogenesis, maturation and dynamics of autophagosomes. Like mitochondria, studies from neurons highly suggest that autophagosomes are uniquely regulated in axons and undergo MT-based transport (Hollenbeck, 1993; Maday et al., 2012). However, their axonal transport is mainly governed by dynein, MT-based retrograde motor protein (Maday et al., 2012; Cheng et al., 2015), so differs from the motility characteristic of other organelles, such as mitochondria (Morris and Hollenbeck, 1993) which exhibit both anterograde and retrograde movements in axons. Studies from primary dorsal root ganglion (DRG)

neurons showed that autophagosomes initiate in presynaptic nerve terminals and mature during dynein-dependent retrograde transport toward neuronal soma, where they fuse with lysosomes (Maday et al., 2012). They observed that autophagosomes initially display bidirectional motility at the distal tip of axon, however, in the middle of axon they develop pronounced retrograde transport without pauses or switches in direction. Interestingly, those retrograde-moving autophagosomes become increasingly acidified in axon near the cell body. In addition, study from cortical neurons also provides an evidence of unidirectional retrograde transport of autophagosomes along the axon (Lee et al., 2011). Therefore, these observations suggest the importance of axonal transport of autophagosomes for their life cycle in neurons: that the autophagosomes undergo maturation as they move retrogradely toward the neuronal soma.

So far, the underlying mechanism of how axonal autophasosomes display primarily retrograde transport is still not clear. Surprisingly, not only dynein and dynactin also the anterograde motors, kinesin-1 and kinesin-2, were co-purified with isolated autophagosomes by immunoblotting (Maday et al., 2012). This probably can explain the bidirectional movement of autophagosomes in the distal tip of axon, and further suggests the idea of an underlying mechanism involving competing motor proteins, dynein and kinesins, to give autophagosomal net movements. Indeed, it is thought that the axonal transport of autophagosomes is regulated by promoting dynein motor activity while inhibiting the activity of kinesins. In this regard, it is notable that the motor scaffolding protein JIP1 is proposed to be a coordinator for both dynein and kinesin-1 activity in autophagosomal transport (Fu et al., 2014). It is reported that JIP1 binds to LC3 (mammalian homolog of Atg8) and broadly associates with autophagosomes. Interestingly, JIP1 can directly bind to the dynein activator dynactin as well as to the motor subunit of kinesin-1, kinesin heavy chain. Importantly, however, JIP1 cannot simultaneously bind to both dynactin and kinesin, instead it forms either a retrograde or an anterograde motor protein complex (Figure 1.5). In addition to JIP1, other studies proposed a role for htt and its adaptor protein, hutingtin-associated protein 1 (HAP1), as regulators in axonal transport of autophagosomes (Wong and Holzbaur, 2014b). Using live cell imaging in primary neurons, it has been shown that htt/HAP1 complex enhances

retrograde transport of autophagosomes. Interestingly, depletion of htt/HAP1 by RNAi knockdown significantly disrupts autophagosomal retrograde transport and leads to accumulation of autophagosomes with undegraded mitochondria. Consistently, neurons expressing pathogenic polyQ-htt also display disrupted autophagosomal dynamics. Since the defective transport of autophagosomes induced by polyQ-htt caused the accumulation of polyQ-htt aggregates as well, this clearly suggests that the axonal transport of autophagosome is tightly associated with cargo degradation for neuronal protection. Therefore, like mitochondrial axonal transport, the axonal transport of autophagosomes is also important for a better understanding of underlying mechanisms in neurodegenerative diseases.

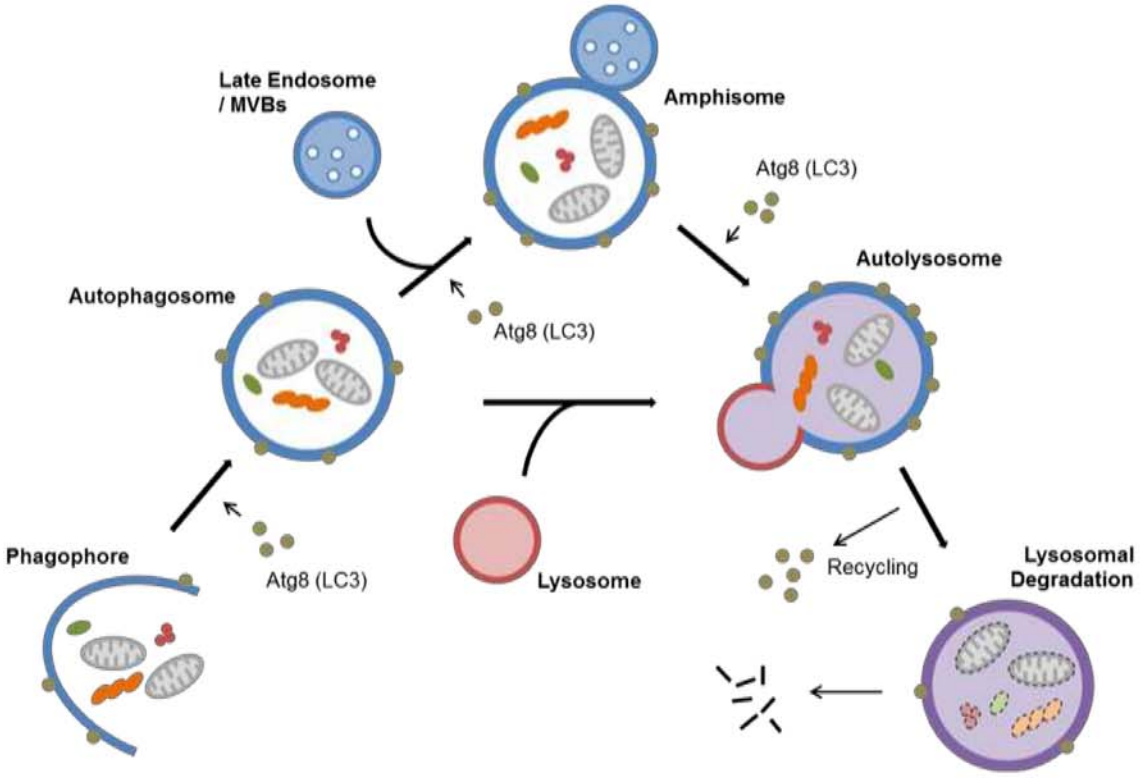

Figure 1.4 Pathway of autophagy: the macroautophagy process. The phagophore is formed to engulf proteins and organelles such as mitochondria. These proteins and organelles are then enclosed and sequestered by double-membrane vesicles, autophagosomes. Autophagosomes undergo maturation and fusion with early/late endosomes and multi-vesicular bodies (MVBs) to generate amphisomes. Formed autophagosomes are delivered to fuse with lysosomes, forming autolysosomes for lysosomal degradation. During autophagic progression, Atg8 (LC3; mammalian homolog of yeast Atg8) controls phagophore expansion and regulates the formation of autophagosomes until fusion with the lysosome. Atg8 (LC3) and autophagy-derived components are recycled.

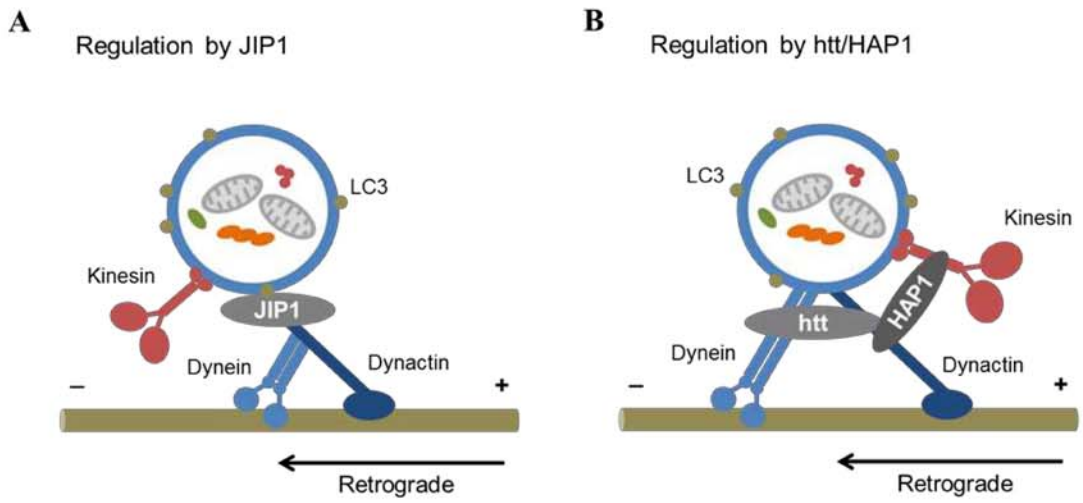

Figure 1.5 Regulation of autophagosomal transport. Two proposed machineries for the retrograde axonal transport of autophagosome in neurons. (A) Model for the effect of JIP1 recruitment on autophagosomal retrograde transport. JIP1 can bind to both kinesin and dynactin, however, cannot bind to both simultaneously. (B) Model for the effect of huntingtin (htt)/HAP1 complex on autophagosomal retrograde transport. Htt and HAP1 play as regulators for autophagosomal transport by constituting a motor protein complex with dynein, dynactin and kinesin.

1.3 PINK1/Parkin Pathway in Mitochondrial Quality Control

As described above, an understanding of mitochondrial transport, fission-fusion and mitophagy together provide a way to explain more fully the life cycle of mitochondria in neurons. Due to the potential distribution of functions among distant compartments, the regulation of the mitochondrial life cycle and maintenance of a robust functional population, termed mitochondrial "quality control (QC)" (Chen and Chan, 2009; Rugarli and Langer, 2012), are likely to be more complex in neurons *in vivo* than in cells of more modest dimensions. Recently, it has been proposed that mitochondrial dynamics and QC are functionally regulated by the proteins that are associated with PD. These proteins include α-synuclein, DJ-1, leucine-rich repeat kinase 2 (LRRK2) and PINK1/Parkin (Henchcliffe and Beal, 2008).

Parkin is an E3 ubiquitin ligase that partially localizes to mitochondria (Clark et al., 2006) and controls mitochondrial fidelity via PINK1, PTEN-induced putative kinase 1 (Park et al., 2006). Genetic analysis in *Drosophila* has demonstrated that *PINK1* and *parkin* are functionally related. In *Drosophila*, a null mutant of PINK1 ($PINK1^{B9}$) phenocopies the Parkin null mutants ($park^{25}$). Both mutant flies showed shorted lifespan, apoptotic muscle degeneration, male sterility and disruptions of locomotion (Greene et al., 2003). Importantly, over-expression of *parkin* was able to rescue these fly defects found in *PINK1* mutants, whereas double mutants showed the same phenotypes as both of them alone. In addition, overexpression of *PINK1* did not rescue the *parkin* defective phenotypes (Clark et al., 2006; Park et al., 2006). These findings clearly suggested that *PINK1* and *parkin* function in the same pathway, and that *parkin* acts downstream of *PINK1*. For this reason, it is important to elucidate how the PINK1 and Parkin are functionally incorporated in mitochondrial quality control.

1.3.1 Mitochondrial dynamics for organelle quality control

Probably, digestion in lysosomes would be the final destination for the dysfunctional mitochondria and/or for their damaged components to be removed and recycled properly

in neurons. Here, mitochondrial axonal transport may help to send the damaged organelles to their final destination, while mitochondrial fission may sequester, and fusion may dilute, the senescent components in neuronal mitochondrial networks. As mitochondria display dynamic a life cycle in neurons, we expect their movement, morphological changes and degradation to be closely inter-related. Recently, the reciprocal interactions between these components of mitochondrial life cycle are becoming more appreciated, however, little is understood about their molecular mechanisms.

Remarkably, numerous studies indicate that mitochondrial axonal transport and their fission-fusion processes are closely inter-related. A study from cultured *Drosophila* neurons revealed that the myosin V depletion significantly increases number of elongated mitochondria in axons (Pathak et al., 2010). On the other hand, it is also reported that mitochondrial fission protein Drp1 effects on the proper distribution of mitochondria in *Drosophila* NMJs (Verstreken et al., 2005). In addition, studies from cultured DRG neurons suggested the involvement of the mitochondrial fusion protein Mfn2 in mitochondrial movement. Importantly, Mfn2 interacts with Miro and milton, key components that link mitochondria to MT-based kinesin motors (Baloh et al., 2007; Misko et al., 2010). Furthermore, a study from the axons of *Drosophila* larval neurons suggested that knockdown of Opa1 (mitochondrial inner membrane fusion protein) by RNAi impairs mitochondrial transport mainly in retrograde movements (Yu et al., 2016). Though the exact relationship between mitochondrial movements and morphological changes remains unclear, collected results suggest that these two components are tightly integrated in neurons: dysregulation of mitochondrial axonal transport affects organelle morphology (Pathak et al., 2010), while altered fission-fusion balance impairs axonal mitochondrial motility (Verstreken et al., 2005; Baloh et al., 2007; Misko et al., 2010; Yu et al., 2016).

Recently, an interesting idea describing the regulation of mitochondrial quality control via a vesicular trafficking pathway has been proposed. It has been reported that a subpopulation of mitochondria-derived vesicles (MDVs) can carry selected cargo to lysosomes under oxidative stress. This was surprising because of its independent role

from both mitochondrial fission and mitophagy. It was found that the formation of stress-induced MDVs is Drp1 independent, and also the transport of MDVs to lysosomes is Atg5 and LC3 (Atg8) independent (Soubannier et al., 2012). Notably, rather, it was found that the generation of MDVs in response to mitochondrial oxidative stress is regulated by PINK1 and Parkin (McLelland et al., 2014). Thus, these findings suggest that the dysfunctional mitochondria can undergo comparably faster quality control via MDVs, by carrying selective cargo to lysosomes, whereas turnover of the entire organelle by mitophagy process is relatively slow.

Indeed, PINK1/Parkin is known to function in mitochondrial dynamics broadly: not only in MDV generation, but also in mitochondrial axonal transport, in mitochondrial fission-fusion balance and in targeting dysfunctional mitochondria. Therefore, exploring the role of PINK1/Parkin in mitochondrial life cycle may provide a good guide to elucidate the intricate interrelationship of mitochondrial dynamics and to understand organelle quality control in neurons (Figure 1.6).

1.3.2 PINK1/Parkin pathway in mitochondrial axonal transport

Since the major compartments of the lysosome are found near nucleus, the axonal transport of mitochondria is thought to be highly linked with organelle turnover and quality control in neurons. As previously described (briefly in 1.1.1.2), PINK1 and Parkin are two proteins that are intensively studied for their potential linking of mitochondrial movement with organelle quality control.

The potential involvement of PINK1/Parkin in mitochondrial movement was first suggested by a biochemical assay which provided evidence of physical association between PINK1 and the Miro/milton complex (Weihofen et al., 2009). Later, Miro was also demonstrated to be a substrate of Parkin (Liu et al., 2012). It was reported that PINK1 phosphorylates Miro, which is critical for the subsequent activation of Parkin to this motor protein complex. Thus, the activation of PINK1/Parkin pathway promotes proteasomal degradation of Miro and consequently arrest mitochondria by detaching organelle from the MT-based motor. The idea of linker protein dissociation by

PINK1/Parkin pathway could explain the mitochondrial arrest caused by up-regulation of PINK1 or Parkin, and the enhanced mitochondrial movements caused by knockdown of PINK1 or Parkin (Wang et al., 2011). However, it is still not clear whether PINK1/Parkin selectively targets dysfunctional mitochondria in axonal transport so as to enhance organelle quality control. In this context, it is noteworthy that the results from immunoprecipitation show the interactions of PINK1 and Parkin with Miro upon mitochondrial depolarization by carbonyl cyanide *m*-chlorophenylhydrazone (CCCP) treatment.

The association of PINK1/Parkin with Miro caused by experimental mitochondrial depolarization is important for understanding a role of mitochondrial axonal transport in organelle quality control. Since Miro can also interact with Mitofusins (Misko et al., 2010), a proposed model for mitochondrial axonal transport and organelle quality control involving PINK1/Parkin is that PINK1/Parkin pathway arrests damaged mitochondria and prevents them from fusing with others, so that the damaged organelle can be quarantined in a fragmented state. If this is true, it probably supports the autophagosomal engulfment for mitophagy process by producing stationary and fragmented mitochondria (Figure 1.6).

1.3.3 PINK1/Parkin pathway in mitochondrial fission and fusion

Like mitochondrial axonal transport, the morphological changes of mitochondria by fission-fusion are also thought to be related to organelle turnover and quality control in neurons. Specifically, it is thought that fission is responsible for sequestration and isolation of dysfunctional mitochondria thus may help to promote their degradation. On the other hand, fusion seems to be required for dilution of damaged mitochondrial materials to complement and protect the organelle functions. Indeed, PINK1 and Parkin have been also reported to function not only in the mitochondrial transport machinery, but also in mitochondrial fission-fusion. Thus, a better understanding of these two PD related genes is needed if we are to determine the role of mitochondrial fission-fusion processes in the organelle quality control.

How does the PINK1 and Parkin pathway regulate mitochondrial morphology in organelle quality control? Genetic studies in *Drosophila* flight muscle revealed that knocking out either protein caused swollen and enlarged mitochondria (Clark et al., 2006; Poole et al., 2008). Although it still remains unclear that the modulation of mitochondrial morphology by PINK1/Parkin seems different from mammalian cells, studies in *Drosophila* suggest that PINK1 and Parkin seem to promote mitochondrial fission and/or inhibit mitochondrial fusion. Importantly, mitochondrial morphological defects caused by PINK1/Parkin depletion were restored by over-expression of the fission protein Drp1 or down-regulation of fusion proteins Mfn2 and Opa1 (Poole et al., 2008). Though the epistatic relationship of PINK1/Parkin to the mitochondrial fission and fusion may not be direct, these observations clearly indicate a genetic interaction between PINK1/Parkin and mitochondrial fission-fusion machineries.

Interestingly, a recent study in mouse cardiac myocytes proposes that the Mfn2 is a mitochondrial receptor for Parkin recruitment (Chen and Dorn, 2013). In this study, it is reported that phosphorylation of Mfn2 by PINK1 promotes the interaction between Mfn2 and Parkin. In addition, Mfn2 knockout prevented Parkin translocation to the depolarized mitochondria under carbonyl cyanide 4-phenylhydrazone (FCCP) treatment. Since the depletion of Mfn2 subsequently suppressed mitophagy events (Chen and Dorn, 2013), this suggests a potential mechanism by which Mfn2 can mediate PINK1 and Parkin for mitochondrial quality control (Figure 1.6).

1.3.4 PINK1/Parkin pathway in mitophagy

So far, it is not clear whether PINK1 and Parkin specifically target dysfunctional mitochondria for autophagosomal engulfment and lysosomal degradation in neurons. Recently, however, numerous studies in non-neuronal cells provide evidence of PINK1/Parkin involvement in experimentally-depolarized, dysfunctional mitochondria (Narendra et al., 2008; Jin et al., 2010; Matsuda et al., 2010; Narendra et al., 2010; Ashrafi et al., 2014; Lazarou et al., 2015). Thus, exploring how PINK1 and Parkin play a

role in mitochondrial turnover is required for better understanding mitochondrial quality control in neurons under normal physiological conditions.

Normally, PINK1 is known to be cleaved by mitochondrial translocase of the inner membrane (TIM) and presenilin-associated rhomboid-like protease (PARL) which reside in the mitochondrial inner membrane, so that it is kept in an inactivate state (Jin et al., 2010). PINK1, however, can be stabilized and thus accumulate on the outer membrane of mitochondria upon organelle depolarization, there to subsequently recruit Parkin to the mitochondrial surface (Jin et al., 2010; Matsuda et al., 2010; Narendra et al., 2010). In addition, knockdown or knockout of PINK1 results in failure to translocate Parkin to mitochondria even under CCCP treatment (Matsuda et al., 2010; Narendra et al., 2010). These observations clearly demonstrated that Parkin translocation to the depolarized mitochondria is mediated by PINK1.

PINK1 phosphorylates either ubiquitin (Ub) or Parkin to trigger translocation of Parkin and to promote ligase activity of Parkin. Translocation and activation of Parkin on depolarized mitochondria leads to further ubiquitination of mitochondrial outer membrane proteins, such as Miro and Mfn2. It is believed that this stepwise process driven by PINK1/Parkin leads to recruitment of the autophagosomal machinery for engulfment and removal of damaged mitochondria. Still, adaptors that bind to ubiquitin chains on damaged mitochondria for the PINK1/Parkin-mediated autophagic process is not known. However, several proteins are proposed to play a role in PINK1/Parkin-mediated mitophagy as an autophagic receptor. It was suggested that Parkin-dependent mitophagy requires the ubiquitin-autophagic adaptor p62. In this study, it was identified that voltage-dependent anion channel 1 (VDAC1) is a target protein of Parkin activity in response to mitochondrial depolarization (Geisler et al., 2010). Recently, two other candidates, optineurin and NDP52, have been shown to mediate PINK1/Parkin-dependent mitophagy in the absence of p62 (Wong and Holzbaur, 2014a; Lazarou et al., 2015). In addition, however, contradictory findings were also reported in the identification of autophagic receptors for PINK1/Parkin-mediated mitophagy. Ambra1, an activating molecule in beclin1-regulated autophagy, is an example. A study in cultured cells demonstrated that the endogenous Ambra1 and Parkin are coimmunoprecipitated

and their interaction was pronouncedly increased under mitochondrial depolarization (Van Humbeeck et al., 2011). Contrary to this, however, it was also reported that Ambra1 induces the LC3-dependent mitophagy process under antimycin A (Ant A) treatment in Parkin-deficient cell lines (Strappazzon et al., 2015). Though there are still uncertain and contradictory observations in identification of PINK1/Parkin-mediated autophagic receptor, the suggested proteins activated by PINK1/Parkin are recruited to the depolarized mitochondria prior to the formation of LC3-positive autophagosomes. Therefore, these recent findings provide several possible links between PINK1, Parkin and the selective mitochondrial degradation via autophagosomes in neurons.

It is important to note that the previous studies demonstrating the role of PINK1 and Parkin in mitochondrial turnover have been carried out largely using chemically-uncoupled mitochondria in immortalized cell lines (Narendra et al., 2008; Geisler et al., 2010; Matsuda et al., 2010; Narendra et al., 2010; Van Humbeeck et al., 2011; Wong and Holzbaur, 2014a; Lazarou et al., 2015; Strappazzon et al., 2015). This actually raises the issue of how and whether the PINK1/Parkin pathway regulates neuronal mitochondrial autophagy *in vivo* under normal physiological conditions. In addition, since mitochondrial QC includes not only autophagy, but the interrelated processes of transport, biogenesis, fission and fusion (Chen and Chan, 2009), broader regulatory effects of PINK1/Parkin activity may occur. In particular, the compartmentalization of neurons raises the question of whether different components of regulation of the mitochondrial life cycle may be spatially segregated for organelle QC in neurons.

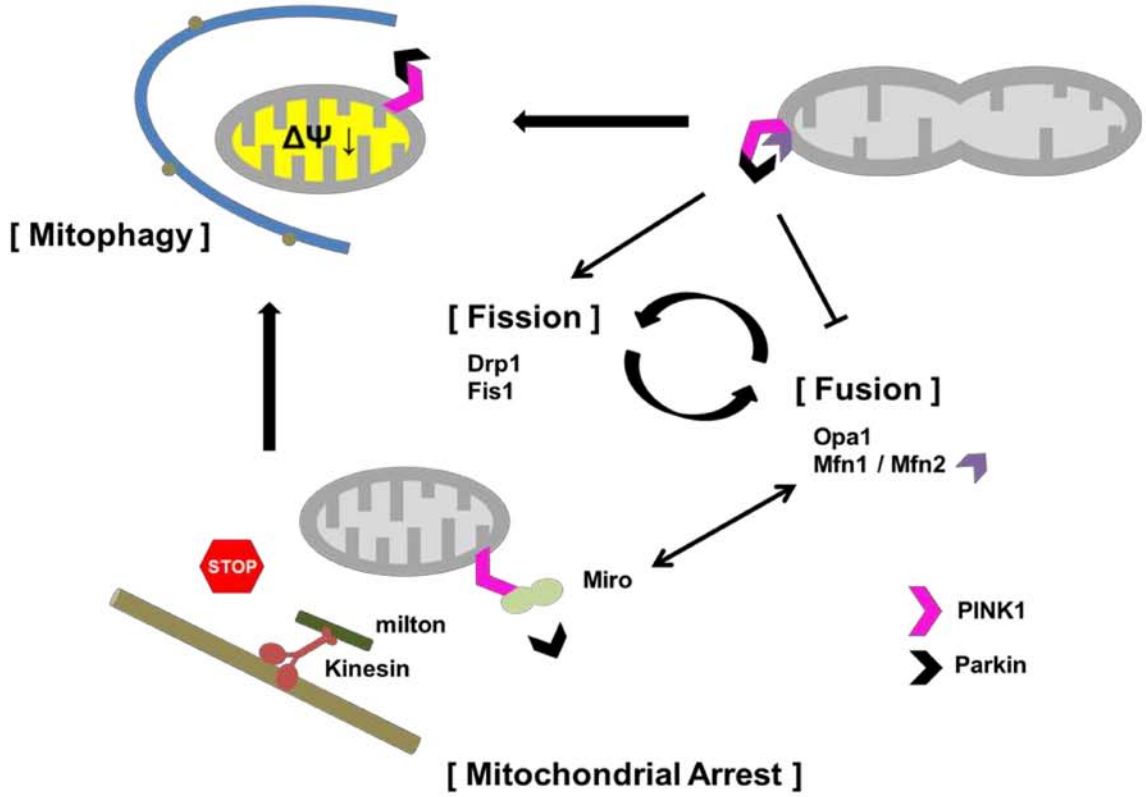

Figure 1.6 Possible PINK1 and Parkin roles in mitochondrial quality control. Mitochondrial dynamics and turnover are intricately coupled by PINK1 and Parkin. PINK1/Parkin dissociates the linker protein, Miro, from the milton/kinesin motor protein complex for mitochondrial arrest. Arresting mitochondria by PINK1/Parkin may help the degradation of damaged organelle, and the mitochondria are targeted by PINK1 and Parkin upon the organelle depolarization. PINK1/Parkin pathway promotes mitochondrial fission and/or inhibits mitochondrial fusion. Mitochondrial fission by PINK1/Parkin segregates and isolates the damaged mitochondria, and this may help autophagic engulfment for the organelle turnover. Miro interacts with Mitofusins (Misko et al., 2010), which can couple the mitochondrial axonal transport and morphological changes. As discussed, data exist to support and to contradict most aspects of these model mechanisms.

CHAPTER 2. MATERIAL AND METHODS

2.1 Materials and Model System

2.1.1 Reagents

Hemolymph-like buffer (HL6 buffer containing 0.6 mM $CaCl_2$ and 4 mM L-glutamate), CO_2, dH_2O, VALAP (Vaseline, Lanolin and Paraffin mixture), 70% ethanol, DMSO - dimethyl sulfoxide (Sigma, #D2650), TMRM - tetramethylrhodamine methyl ester (Life Technologies Molecular Probes, #T668), agarose (Invitrogen, #15510-019), Triton X-100 (Sigma, #9002-93-1), PBS, Sparkle glass cleaner, Endotoxin-free sterile water (VWR, #16750-098), Schneider's medium (Gibco, #21720-024), FBS (Atlanta Biologiclas, #S11150H), Pen-Strep (50 μg/ml of penicillin with 50 μg/ml of streptomycin), Ca^{2+}/Mg^{2+}-free saline, collagenase (Sigma,#C2674), concanavalin A (Sigma, #C0412), H_2O_2 (Mallinckrodt, #7722-84-1), antimycin A (Sigma, #A8674), paraformaldehyde, BSA (Sigma, #9048-46-8), Precision plus protein standards (Bio-Rad, #161-0373).

2.1.2 Equipment

Sylgard plate, 3 concavities glass slide, two pairs of fine paint brushes (Daler Rowney, #00), Vannas Spring Scissors - Straight/Sharp/8 cm/3 mm Cutting Edge (Fine Science Tools, #15000-00), two pairs of Dumont #5 Forceps - Standard Tips/Straight/Dumostar/11 cm (Fine Science Tools, #11295-00), Dumont #7 Forceps - Inverted/Curved/11.5 cm (Fine Science Tools, #11274-20), Minutien Pins - Stainless Steel/0.1 mm Diameter (Fine Sciences Tools, #26002-10), dental wax (Surgident, #50092189), double-sided tape (Scotch, #137DM-2), cotton swab (Puritan, Cotton

Tipped Applicators), siliconized p200 pipette tips (VWR, #53503-790), 1.5 ml microfuge tube (VWR, #20901-551), 25 X 75 mm glass slides (Rite-on Gold Seal Micro Slides Pre
Cleaned, #3050), 25.4 X 76.2 mm single concavity glass slides (Pearl, #7103), 24 X 40 mm cover glasses (VWR, #16004-306), 22 X 22 mm cover glasses (VWR, #48366-067), 35 X 10 mm tissue culture dishes (Falcon, #353001), Mini-protean TGX^{TM} gels (Bio-Rad, #456-1033), BCA^{TM} protein assay kit (Pierce, #23227), Mini trans-blot cell (Bio-Rad, #1703989), Nitrocellulose membranes (Thermo Sci., #88025).

2.1.3 *Drosophila Melanogaster*

All flies were reared in polystyrene vials (25 X 95 mm) with standard cornmeal agar medium. Fly stocks were maintained at 25^{o}C room temperature and 50% humidity with a 12 h light/dark cycle. The table below is the *Drosophila* strains used in this study:

Table 2.1 Genotypes of *Drosophila* strains

Genotype		Derived from crossing of	
		Female	Male
#1	*D42-Gal4>UAS-mitoGFP* (III)		
#2	w^{1118}		
#3	*D42-Gal4>UAS-mitoGFP/+* (III)	#1	#2
#4	$park^{25}$*, D42-Gal4/TM6B* (III)		
#5	$park^{25}$*,UAS-mitoGFP/TM6B* (III)		
#6	$park^{25}$*, D42-Gal4/*$park^{25}$*,UAS-mitoGFP* (III)	#4	#5
#7	*UAS-*$Parkin^{C2}$*/CyO* (II); $park^{25}$*, D42-Gal4/TM6B* (III)		
#8	*UAS-*$Parkin^{C2}$*/CyO* (II); $park^{25}$*, UAS-mitoGFP/TM6B* (III)		
#9	*UAS-*$Parkin^{C2}$ (II); $park^{25}$*, D42-Gal4/*$park^{25}$*, UAS-mitoGFP* (III)	#7	#8
#10	*UAS-RFPatg8* (II); *D42-Gal4>UAS-mitoGFP* (III)		
#11	*UAS-RFPatg8* (II); *+/TM6B* (III)		
#12	*UAS-RFPatg8* (II); *D42-Gal4>UAS-mitoGFP/+* (III)	#10	#11
#13	*UAS-RFPatg8* (II); $park^{25}$*, D42-Gal4/TM6B* (III)		
#14	*UAS-RFPatg8* (II); $park^{25}$*, UAS-mitoGFP/TM6B* (III)		
#15	*UAS-RFPatg8* (II); $park^{25}$*, D42-Gal4/*$park^{25}$*, UAS-mitoGFP* (III)	#13	#14

Table 2.1 continue

#16	*dpr-Gal4/CyO* (II)		
#17	*UAS-mitoGFP/gla* (II); *+/TM6B* (III)		
#18	*dpr-Gal4/UAS-mitoGFP* (II)	#16	#17
#19	$park^{1}$*/TM6B* (III)		
#20	*TM2/TM6B* (III)		

2.2 *Drosophila* Preparation for *In Vivo* and *In Vitro* Conditions

2.2.1 Fly larval dissection for *in vivo* observation

Procedures of larval dissection and mounting were performed essentially as previously described (Devireddy et al., 2014). Wandering late third instar larvae were collected for larval dissection, and washed gently by distilled water in 3 concavities glass slide to remove the remaining cornmeal agar medium. Washed larvae were placed on a Sylgard plate with the dorsal side up, and fixed with Minutien Pins at posterior and anterior ends of body. Pinned larvae were dissected with a Vannas Spring Scissors from posterior to anterior along the dorsal body wall in a puddle of HL6 buffer containing 0.6 mM of $CaCl_2$ and 4 mM of L-glutamate. Fat bodies and intestines were then removed gently with Dumont #5 Forceps to reveal the intact ventral ganglion, segmental nerves and neuromuscular junctions (Pilling et al., 2006; Louie et al., 2008; Shidara and Hollenbeck, 2010). The dissected and cleaned larva was unpinned from Sylgard plate and gently arranged dorsal side up on a 25 X 75 mm glass slide using a fine paint brush. The dissected larva was then covered by a 24 X 40 mm cover glasses using dental wax as a spacer to form a chamber. The chamber was filled with ~ 120 µl of HL6 buffer, and sealed with VALAP for imaging. Segmental nerves, branched thin axons, ventral ganglia, and neuromuscular junctions from the dissected late third instar larva (Figure 2.1) were monitored for *in vivo* observation. To insure normal *in vivo* conditions of the nervous system, larval dissection was performed in no longer than 5 minutes and larval motor neurons were observed within 20 minutes of dissection (Shidara and Hollenbeck, 2010; Devireddy et al., 2014).

2.2.2 Adult fly wing preparation for *in vivo* observation

Hatched flies were synchronized by age to collect the 5-day-old adults for wing preparation, and paralyzed on a CO_2 anesthetizing pad. The fly wings were visualized under a regular dissecting stereomicroscope, and prepared on a Sylgard plate. In all experiments, only the right wing from the female adult was used. The wing preparation

was performed to serve the experimental purpose using one of the two methods described below (Fang et al., 2013): live imaging of the wing nerve, or quick imaging of detached wings.

Live imaging of the wing nerve: paralyzed 5-day-old adult flies were collected, and their left wings were cut at the end of wing root with a Vannas Spring Scissors to avoid a hindrance to right wing observation. Prepared flies were then mounted on 25.4 X 76.2 mm single concavity glass slides. Using a fine paint brush, flies were posed ventral side up in the concave well, and their bodies were fixed in place with 2% agarose. The wing was placed flat and extending out from the body. Concave glass slides with prepared fly samples were cover by 24 X 40 mm cover glasses using dental wax as a spacer to form a chamber.

Quick imaging of detached wings: paralyzed 5-day-old adult flies were collected, and their right wings were cut at the end of wing root with a Vannas Spring Scissors to preserve whole nerve tract along the humeral crossvein with the lateral vein and costal vein (Fang et al., 2012). Severed wings were pretreated with detergent (20%, Triton X-100 in dH_2O) to avoid trapping air bubbles, and briefly rinsed with 1X PBS. Prepared wings were then mounted on 25 X 75 mm glass slides with the dorsal side up, and covered by 24 X 40 mm cover glasses using dental wax as a spacer to form a chamber. The chamber was filled with PBS and sealed with VALAP for imaging. To insure normal *in vivo* conditions of the wing nervous system, images were taken within 10 minutes of scission.

Neuronal cell bodies from fly wing were observed at the distal part of lateral vein 1 (Figure 2.2, from 3 to 4), and axons of humeral crossvein (Figure 2.2, from 1 to 2) from the wing arch were monitored to analyze axonal mitochondrial density (Carreira et al., 2011).

2.2.3 Primary neuronal cell culture for *in vitro* experiments

Crawling late third instar larvae were selected, sterilized briefly with 70% ethanol and rinsed in dH_2O. Schneider's medium containing 10% FBS and 0.5% Pen-Strep was

prepared, and the washed larvae were transferred to a drop of Schneider's medium on Sylgard plate. Brain lobes and ventral ganglia (CNS) were taken from larvae and transferred into 1.5 ml microfuge tubes containing ~500 µl of Schneider's medium. 5 ~ 7 sets of CNS were collected per each tube, and centrifuge at 300 g for 5 minutes. Supernatant was removed without disturbing the pellet from tubes and 500 µl of Ca^{2+}/Mg^{2+}-free saline with 0.7 mg/ml of collagenase was added to incubate the CNS for 1 hour at room temperature. Incubated CNS was then dissociated into individual cells by siliconized pipette triturating in 500 µl of Schneider's medium. After dissociation, ~ 250 µl of cell solution was transferred to 22 X 22 mm cover glass that coated with 20 µg/ ml of concanavalin A in a 35 X 10 mm tissue culture dish, and incubated 1 hour for cell adhesion. After 1 hour of incubation, 2 ml of Schneider's medium was added and culture dishes were incubated at 22^{o}C in humidified chamber for ~96 hours to allow neurons to extend their processes. After 96 hours, medium was changed to 2 ml of new Schneider's medium prior to imaging. Prepared 22 X 22 mm cover glasses with cultured neurons were flipped over using Dumont #7 Forceps, and mounted on 25 X 75 mm glass slides. Glass slides were prepared by attaching double-sided tape as a spacer to form an imaging chamber. Formed chamber was filled with ~ 100 µl of Schneider's medium, and sealed with VALAP. Using a cotton swab with Sparkle glass cleaner, the sealed cover glasses were cleaned for imaging.

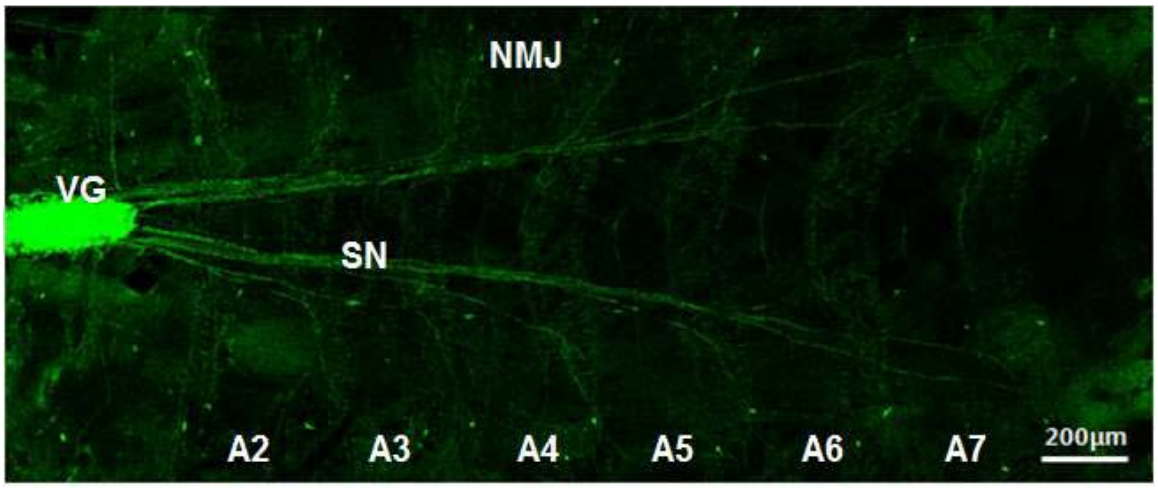

Figure 2.1 Dissected late third instar larva expressing mito-GFP in motor neurons. Mitochondrial movements are monitored at three different regions in the axons of segmental nerves (SNs): proximal (A2), middle (A4), and distal (A7). Cell bodies in the ventral ganglion (VG) and neuromuscular junctions (NMJs) are also analyzed.

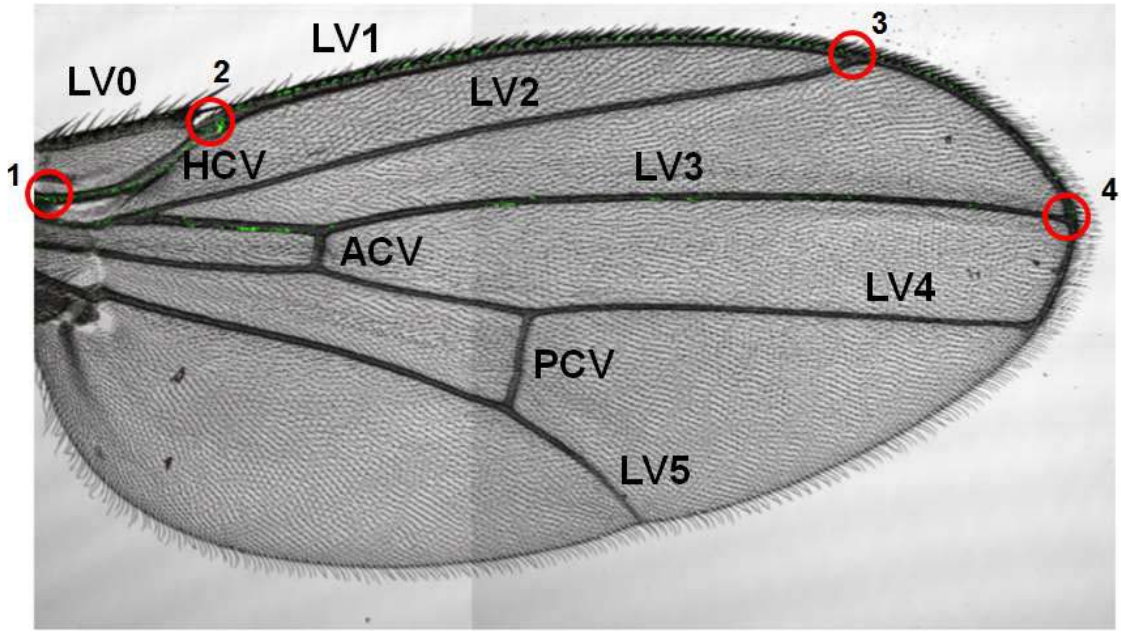

Figure 2.2 *Drosophila*'s wing morphology and axonal mitochondria. Dorsal view of right wing and landmark positioning. LV: longitudinal vein, HCV: humeral crossvein, ACV: anterior crossvein, PCV: posterior crossvein.

2.3 Imaging by Confocal Microscopy

All imaging was performed using a laser scanning confocal microscope (LSCM, Nikon C1 on an Eclipse 90i microscope). Time lapse images, kymographs (Figure 2.3) and 3D structural images (Figure 2.4) were acquired and generated by *NIS-Elements AR 3.2* software.

2.3.1 Time lapse images without photo-bleaching

To analyze organelle movements in larval motor neurons, time lapse images were acquired without photo-bleaching from the longest segmental nerve; mitochondrial movements were analyzed in three different regions (A2, A4 and A7), while autophagic vacuole movements were analyzed in the middle (A4) of the segmental nerve (Figure 2.1). Time lapse confocal images were obtained using 5% laser power with a 488 nm line for mito-GFP and 10% laser power with a 561 nm line for RFP-Atg8 through the smallest pinhole (30 μm). Since images were acquired by a 60X oil-immersion objective and generated by 4X field zoom at 512 pixel resolution, the region imaged for segmental nerves was 51.2 μm in length with varying height. The frames for individual channels (513/30 for mito-GFP and 590/50 for RFP-Atg8) were obtained at 1 second time intervals for 2 minutes. Representative kymographs were generated from the acquired frames (Figure 2.3, A and C) to observe and confirm general movements of organelles. To ensure live physiological conditions of the larval nervous system, time lapse images were taken within 10 minutes of individual animal.

2.3.2 Time lapse images with photo-bleaching

Mitochondrial movements were monitored with photo-bleaching from the middle (A4) of the longest segmental nerve to scrutinize their movements without interference from the abundant, bright, stationary mitochondria. Time lapse confocal images were obtained using 5% laser power with a 488 nm band, and the full intensity (100% laser power) of

488 nm light from the confocal laser at 1 frame scan per second for 30 seconds was used to illuminate the region of interest. Images were acquired by a 60X oil-immersion objective and generated by 4X field zoom at 512 pixel resolution with a regional photo-bleaching. An area box with 30 μm fixed length was drawn in the middle of the assigned segmental nerve to give regional photo-bleaching; 30 μm length illumination within 51.2 μm of segmental nerves. Time course images were obtained at a rate of 1 frame every 2 seconds for 5 minutes, and representative kymographs were generated from the acquired frames (Figure 2.3, B and D). Note that photo-bleaching eliminates the mito-GFP signals from the stationary mitochondria, allowing the visualization of the movement of individual mitochondria clearly. To ensure the live physiological conditions of the larval nervous system, time lapse images with photo-bleaching were taken within 20 minutes of individual animal.

2.3.3 Z-stack images for 3D structure

Images of motor neuronal cell bodies in ventral ganglion (Figure 2.1) were acquired with confocal z-stack frames to construct the 3 dimensional structures. 5% laser power with a 488 nm line was used for mito-GFP and 10% laser power with a 561 nm line was used for RFP-Atg8 through the smallest pinhole (30 μm) by a 60X oil-immersion objective. Confocal z-stack images were generated by *Microscope 90i Z-Drive*, and the frame with focused nucleus set as the *Ref* (Figure 2.4, A). To cover the volume of the cell bodies, set the number of *Steps* as 100 with 0.05 μm *Step Size* to get the *Range* of 5 μm; 2.5 μm *Range* above and below the *Ref*, to *Top* and *Bottom*, respectively. 100 frames of confocal images were then reconstructed to 3 dimensions using *Volume View* generation of *NIS-Elements AR 3.2* software. *Maximum Intensity Projection* was selected for blending the signals, and *Bounding Box* was selected for visualizing axes. To get the single cell body structure, images were cropped and built from 20 μm (X, height) by 20 μm (Y, width) with 5 μm (Z, depth) (Figure 2.4, B).

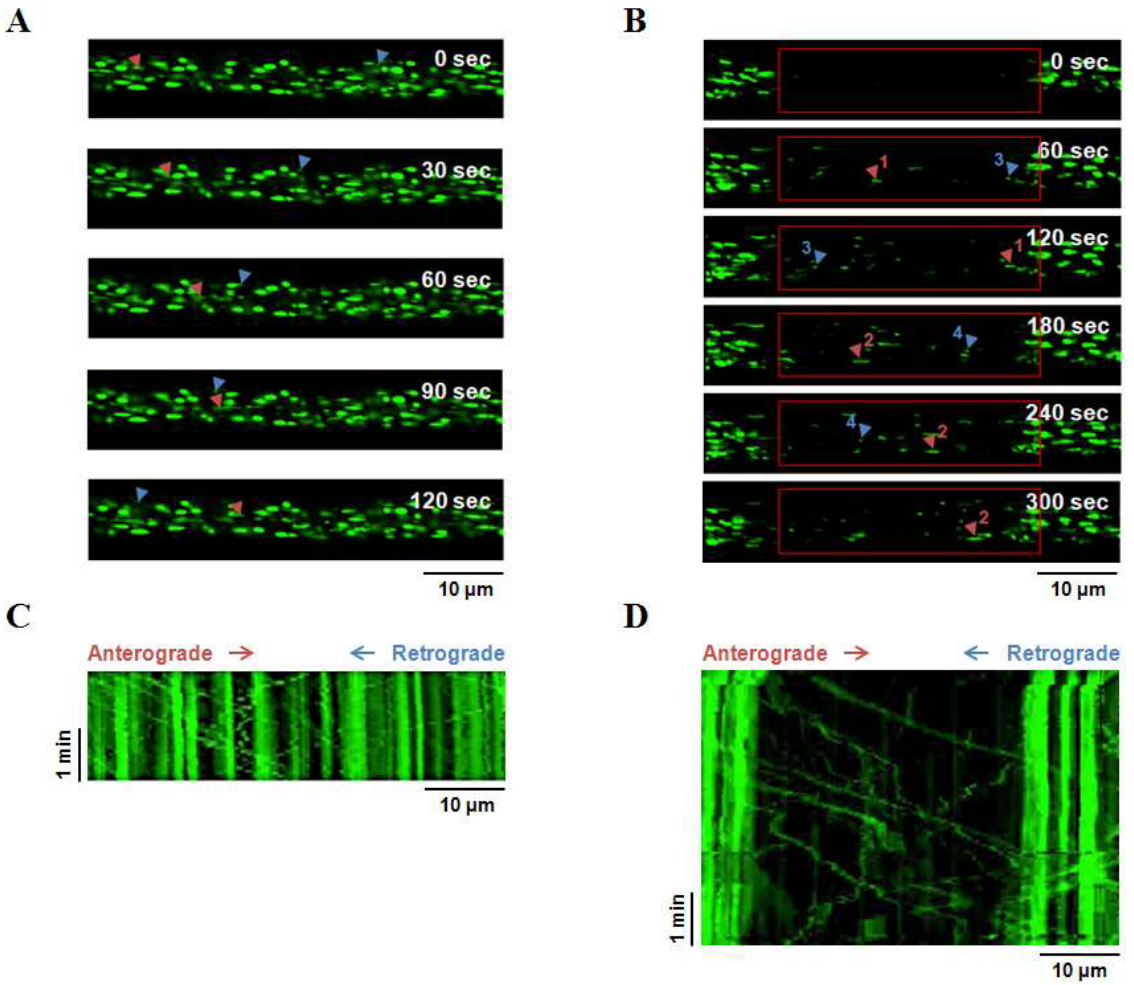

Figure 2.3 Mitochondrial transport without and with photo-bleaching. (A), Representative frames at 30 second intervals spanning 2 minutes under non-bleached conditions. Red arrowheads represent anterograde moving mitochondria, while blue arrowheads represent retrograde moving mitochondria. (B), Representative frames at 60 second intervals spanning 5 minutes under photo-bleached condition. Individual moving mitochondria are marked as red arrowheads (1 and 2) for anterograde and as blue arrowheads (3 and 4) for retrograde. (C), Representative kymograph from (A). (D), Representative kymograph from (B). (Figure is adapted and modified from Devireddy et al., 2014)

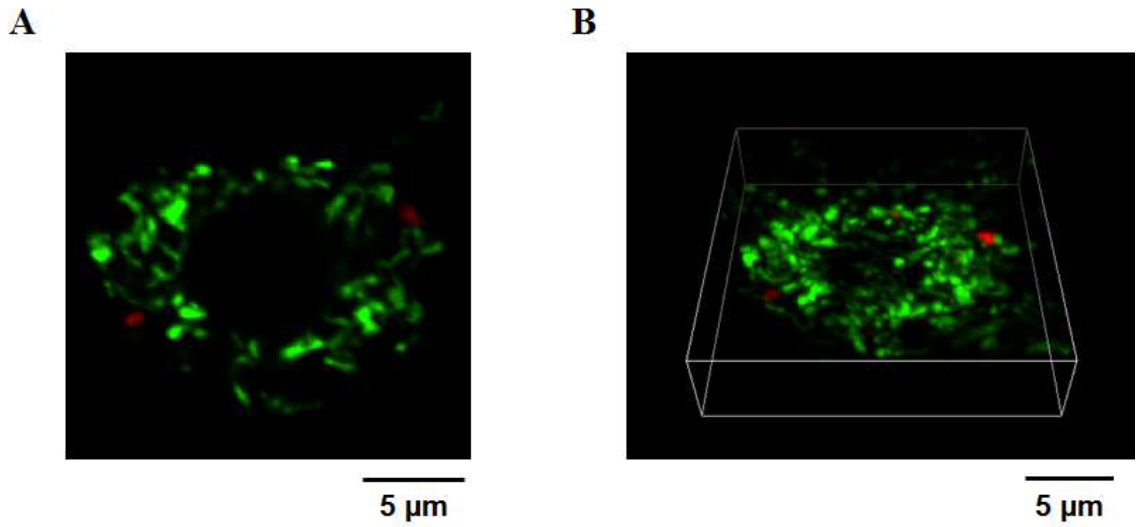

Figure 2.4 Z-stack structure image of organelle from motor cell body. (A), Representative plane image of mitochondria with autophagic vacuoles in motor cell body. Mitochondria are visualized by mito-GFP (green), while autophagic vacuoles are visualized by RFP-Atg8 (red). (B), 3 dimensional structure image of mitochondria with autophagic vacuoles that are reconstructed from (A). 100 frames are obtained to construct the z stacks.

2.4 Analysis of Organelle Movements

For understanding axonal organelle transport, analysis and quantification of moving parameters were performed essentially as previously described (Devireddy et al., 2014).

2.4.1 Mitochondrial movements

Axonal transport ofmitochondria was analyzed based upon the time lapse images of mito-GFP from the longest segmental nerves. **Flux** was measured from three different regions (A2, A4 and A7) of segmental nerves, and *NIS-Elements AR 3.2* software was used for measurement. Mitochondrial flux was measured for both anterograde and retrograde movement by observing the number of moving mitochondria passing a defined point per unit time over 2 minutes. To define the observing point, a vertical line was drawn in the middle of segmental nerve using *Insert Line* by *Annotations* function. **Velocity** was measured from three different regions (A2, A4 and A7) of segmental nerves, and manual tracking of *ImageJ* software was used for measurement. Mitochondrial velocity was measured from a run (continuous movements of more than 3 seconds duration) in one direction. One pixel represents 0.1 μm in the collected images, and only net velocities greater than 0.1 μm/sec or less than - 0.1 μm/sec for at least three consecutive frames were selected as bona fide anterograde and retrograde transport, respectively. During 2 minute time lapse movies, only mitochondria that moved for more than 60 seconds were considered for velocity analysis. At least 5 anterograde and 5 retrograde mitochondria were tracked respectively from each individual animal. **Percent of movement** was measured from three different regions (A2, A4 and A7) of segmental nerves, and *ImageJ* software was used for quantification. The % of mitochondria moving and stationary was measured from the total population of mitochondria within a field. Since the population of mitochondria within the assigned axonal regions included a changing set of moving mitochondria, the second frame of each movie was selected for designating the total mitochondrial population. Mitochondria in the population were categorized and marked as anterograde, retrograde or stationary by the *Cell Counter* plugin in *ImageJ* to quantify

the percentage of moving and stationary mitochondria in segmental axons. **Duty cycle** was measured from three different regions (A2, A4 and A7) of segmental nerves, and *ImageJ* software was used for quantification. After determining the runs and pauses by *ImageJ*, mitochondrial duty cycle was calculated for moving mitochondria based on observing their movement or pause time over the observation interval. The percentage of the time that mitochondria moved in each particular direction or paused was quantified. Only mitochondria that moved for more than 60 seconds were considered for duty cycles, and at least 5 anterograde and 5 retrograde moving mitochondria were selected respectively from individual animals. **Run length** was measured from three different regions (A2, A4 and A7) of segmental nerves, and *ImageJ* software was used for calculation. After determining the runs and pauses by *ImageJ*, mitochondrial run length was defined as the distance per individual run, between stops. Mitochondrial net runs in the dominant direction only for both anterograde and retrograde movement were used for the run length measurement. To calculate the average of run length, the total distance of runs from a moving mitochondrion was divided by the number of runs. At least 5 anterograde and 5 retrograde moving mitochondria were considered respectively from individual animals. **Number of steady-state movers** was measured from the middle (A4) of segmental nerves with photo-bleaching, and *NIS-Elements AR 3.2* software was used for analysis. Every 30 seconds over 5 minutes, number of steady-state moving mitochondria was quantified from the 30 μm bleached regions within 51.2 μm of segmental nerves. To define the observing point, a red box that covers the bleached region was drawn using *Insert Rectangle* by *Annotations* function. Note that the numbers of mitochondria moving into the bleached regions become equal in number of entry and exit within a certain period of time.

2.4.2 Autophagic vacuole movements

Axonal transport of autophagosomes was analyzed based upon the time lapse images of RFP-Atg8 signals from the middle (A4) of the longest segmental nerves. Autophagosomal **flux** was measured as stated above (2.4.1) by using *NIS-Elements AR*

3.2 software. Since some diffuse RFP-Atg8 signal was seen throughout the axonal cytosol, only vacuoles above an assigned threshold intensity (1000 on a 12-bit scale) were designated as autophagosomal vacuoles.

2.5 Determination of Organelle Density and Co-localization

2.5.1 Mitochondrial density in motor axons

MetaMorph version 7.6.5 software was used to measure the mitochondrial density in axons based on the intensity of the mito-GFP signal (Devireddy et al., 2014). Density was defined as the total pixels occupied by mitochondria within the assigned axonal regions. To reduce the noise and sharpen the original images, *Low-Pass2* and *Laplace* filters were consecutively used in *MetaMorph* software. Then, the images were converted to binary forms via *Binary Operations* with 400 minimum intensity thresholds on a 12-bit scale of 0 - 4095 to clarify the shape of the mitochondrial boundary. To retain their original form, the binarized images were processed using *Dilate* with 4 pixel *Neighborhood* using *MetaMorph*. From the binarized and dilated images, the *Integrated Intensity* measurement was used to quantify the area occupied by mitochondria. Axons from different regions (A2, A4 and A7) of larval segmental nerves (Figure 2.5, A) and axons of the humeral crossvein from the adult fly wing arch (Figure 2.5, B) were monitored to analyze the density of axonal mitochondria. To determine mitochondrial density in larval segmental nerves, the second frame of each movie was selected for the quantification.

2.5.2 Organelle density in motor cell bodies and neuromuscular junctions

NIS-Elements AR 3.2 software was used to analyze the area and to quantify the organelle density from the assigned regions, cell bodies or neuromuscular junctions. Density was defined as the area that occupied by organelles of interest, mitochondria or

autophagosomes, divided by the total area of the assigned regions. 515/30 (mito-GFP) channel was used for measuring mitochondrial area, whereas 590/50 (RFP-Atg8 or anti-HRP) channel was used for measuring the area of autophagic vacuoles or synaptic boutons respectively. The density of mitochondria was quantified both from motor cell bodies and neuromuscular junctions, whereas density of autophagosomes was quantified only from motor cell bodies.

Organelle density in motor cell bodies: in each cell body, the *Polygonal ROI* tool was used to draw a region around the cell body and the area occupied by assigned organelles, mitochondria or autophagosomes, was calculated as a fraction of total area (Figure 2.6, A). The images were converted to representative thresholded versions to clarify the shape of the organelle boundaries. Minimum intensities varied while maximum threshold intensity was fixed as 4095 on a 12-bit scale. At least 5 cell bodies were analyzed from individual animals.

Mitochondrial density in neuromuscular junctions: neuromuscular junctions were selected between muscles 7 (M7) and 6 (M6) from the middle (A4) of the body wall (Figure 2.6, B). In each neuromuscular junction, the *Polygonal ROI* tool was used to draw a region around the synaptic boutons and the area covered by mitochondria was calculated and divided by the total area using *ROI Area* (Figure 2.6, C). The images were converted to representative thresholded versions (400 minimum intensity for mitochondria, and 200 minimum intensity for anti-HRP staining) to clarify the shape of the organelle boundaries. At least 5 synaptic boutons were selected from individual neuromuscular junctions for the mitochondrial density measurement.

2.5.3 Co-localization of mitochondria with autophagic vacuoles

Mitochondrial co-localization with autophagic vacuoles was quantified by *NIS-Elements AR 3.2* software. Motor neuronal cell bodies and axons from dissected larvae were selected to analyze the organelle co-localization. *Intensity Profile* from two channels, 513/30 (mito-GFP) and 590/50 (RFP-Atg8), was used to analyze the co-localization. Line

scans of the images were used to indicate the signal *Intensity Profile* of mitochondria and autophagic vacuoles.

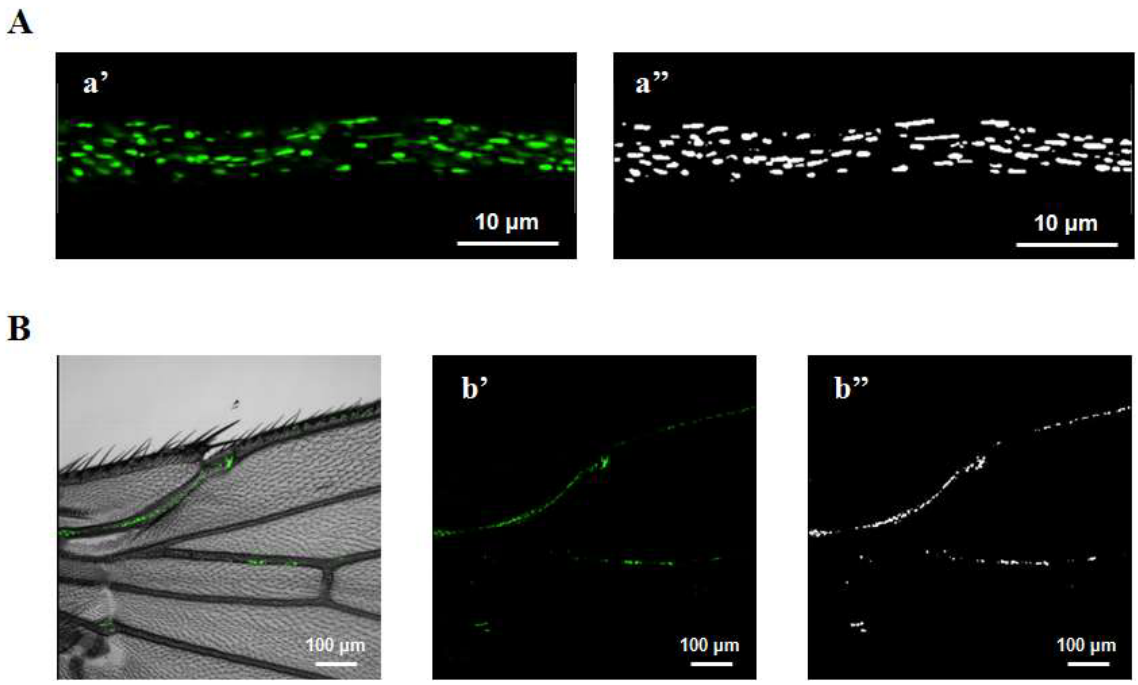

Figure 2.5 Density of mitochondria in motor axons. (A), Representative confocal fluorescence image (a') and converted binary image (a'') of mitochondria from the axon of A4 segmental nerves. (B), Representative confocal fluorescence image (b') and converted binary image (b'') of axonal mitochondria from the humeral crossvein of 5-day-old adult fly wing. Mitochondrial density is quantified from the images of (a'') and (b''). (Figure is adapted and modified from Devireddy et al., 2014)

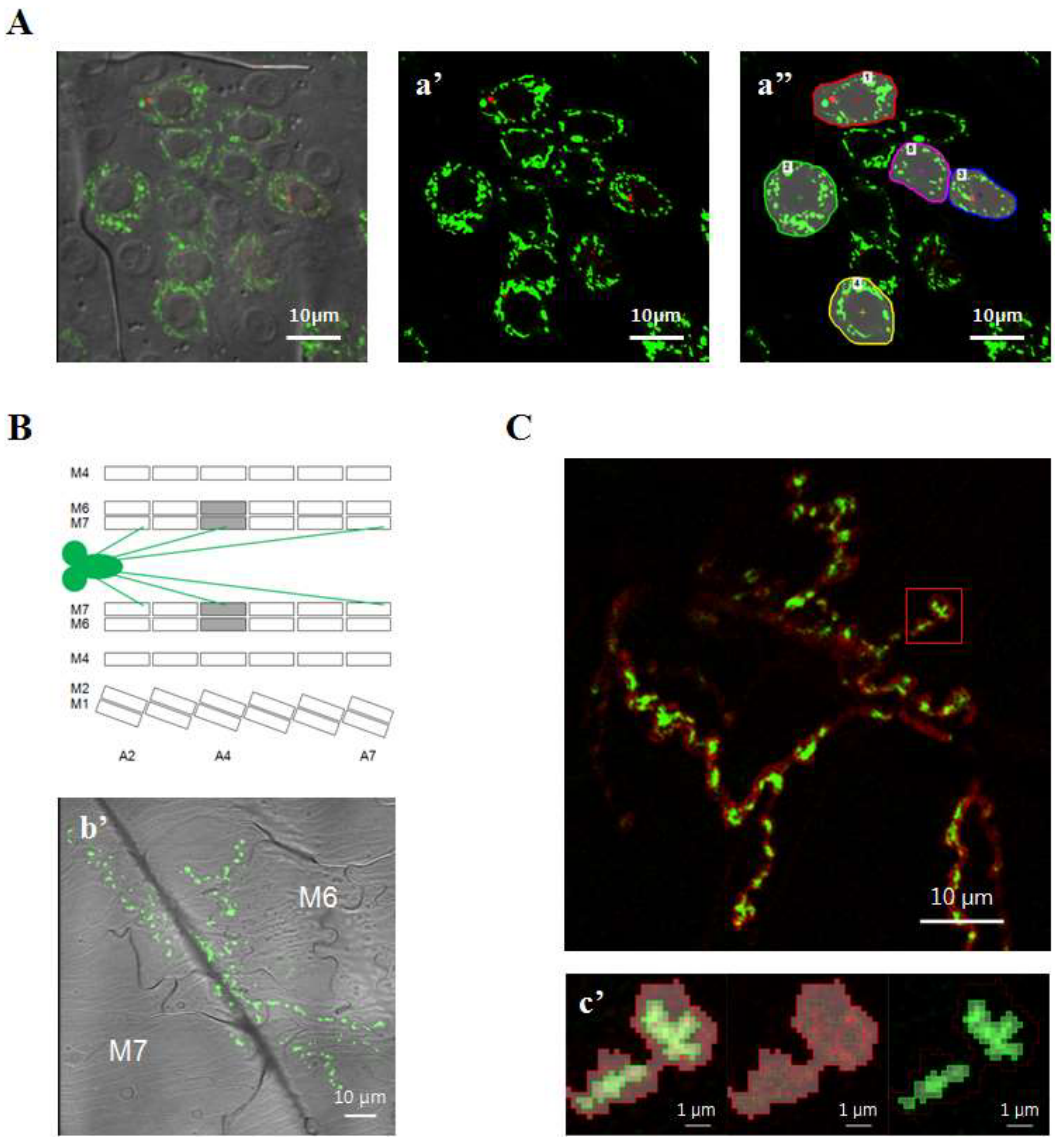

Figure 2.6 Density of organelles in motor cell bodies and neuromuscular junctions. (A), Representative images of motor cell bodies for organelle density measurements. Signal (mito-GFP and RFP-Atg8) are thresholded (a') and the boundaries of cell bodies are designated (a'') for density measurement. (B), Neuromuscular junctions are monitored from the middle (A4) segmental nerves between muscle 7 (M7) and 6 (M6). Mitochondria in neuromuscular junction are visualized by mito-GFP (b'). (C), Representative image of neuromuscular junction for mitochondrial density measurement. Mitochondria are visualized by mito-GFP (green) expression and motor synaptic boutons are stained with anti-HRP (red). The red box indicates higher magnification images (c') of synaptic boutons and mitochondria for the quantification of area.

2.6 Analysis of Mitochondrial Morphology

2.6.1 Measurement of mitochondrial length

The length of axonal mitochondria was determined by manually measurement, using *NIS-Elements AR 3.2* software. Non-overlapping axonal mitochondria were selected from cultured neurons or larval segmental nerves. Stationary and moving (both anterograde and retrograde) axonal mitochondria from three different regions (A2, A4 and A7) of segmental nerves were separately considered for the length measurement. Within the collected frames of time lapse images, the frame that contained the best focused non-overlapping mitochondria was selected. From these frames, the individual coordinates of mitochondria were used for the length measurement. The designated coordinates were measured using *Length* tool with *2 Points* by *Measurements* function. Since 1 pixel represents 0.1 μm in the *NIS-Elements AR 3.2* software images, the minimum standard distance unit was 0.1 μm (Figure 2.7, a). To determine the boundary of mitochondria, images were thresholded at a standard intensity of 200 to identify pixels belonging to mitochondria. At least 5 each of stationary, anterogradely and retrogradely mitochondria were selected respectively from individual animals and 10 mitochondria were selected from each single culture dish for the mitochondrial length measurement.

2.6.2 Measurement of mitochondrial area

The area of axonal mitochondria in segmental nerves was measured from the binarized images by *MetaMorph version 7.6.5* software. Non-overlapping axonal mitochondria from three different regions (A2, A4 and A7) of segmental nerves were selected and considered for the area measurement. From the binarized images, individual polygons were automatically designated by *Create Regions Around Objects* function (Figure 2.7, b). *Integrated Intensity* and *Area* were selected from *Configure* to measure the area of each polygon. Only polygons that represented single mitochondria were considered. At least 10 mitochondria were selected from individual animals.

2.6.3 Analysis of 3D structure of mitochondria

3 dimensional structures of mitochondria were analyzed in motor cell bodies from dissected larvae. Generated 3 dimensional structures from the confocal z-stack frames (2.3.3) were played and monitored through *Show Volume View* in *NIS-Elements AR 3.2* software. Axes were visualized by *Show Axis*, and the volume was clarified by *Show Box* to give an outline of coordinates. From *Volume View*, *Move Orthogonal Cropping Plane* and *Colocalization* were played to analyze the organelle (mitochondria (mito-GFP, 515/30) and autophagic vacuoles (RFP-Atg8, 590/50)) co-localization. To analyze mitochondrial structure, images were rotated using the *Rotation* tool along the X, Y and Z axes. Mitochondrial structure was categorized into 4 different phenotypes; fragmented, wild-type, tubular and hyper-fused. Mitochondrial morphological analyses were performed while blinded to the experimental condition.

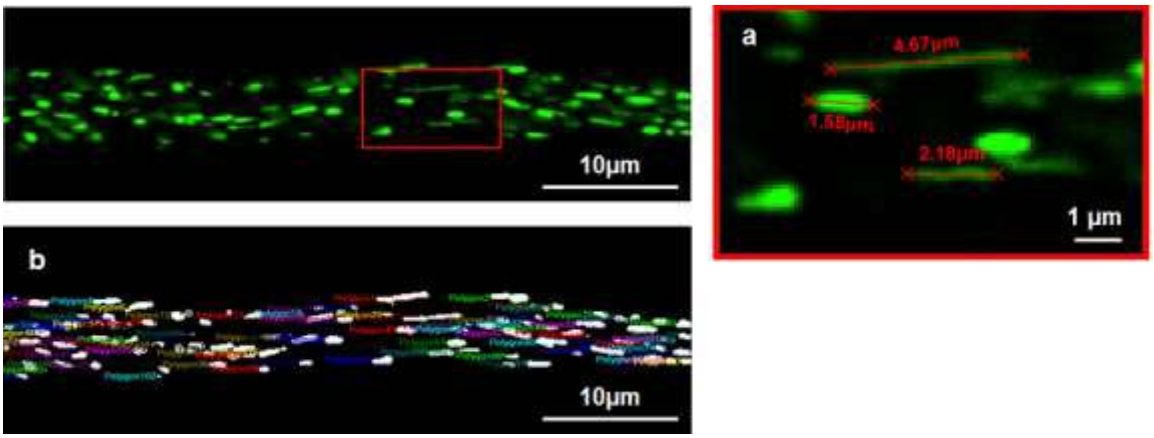

Figure 2.7 Length and area measurement of axonal mitochondria. The red box in a confocal fluorescence image is enlarged in (a) to show mitochondrial length measurements performed using *NIS-Elements* software. Polygons in (b) are designated by *MetaMorph* software from the binary image to measure the area of mitochondria. (Figure is adapted and modified from Devireddy et al., 2014)

2.7 Determination of Mitochondrial Inner Membrane Potential

Tetramethylrhodamine methyl ester (TMRM), a lipophilic cationic fluorescent dye, was used for the determination of mitochondrial transmembrane potential both, *in vivo* (Devireddy et al., 2014) and *in vitro* (Verburg and Hollenbeck, 2008). Thin neurons and neuromuscular junctions adjacent to the middle segmental nerves in larval A4 segment and projected axons of primary cells were selected for measuring neuronal mitochondrial membrane potential under *in vivo* and *in vitro* conditions. TMRM was prepared as a 20 µM working solution by dissolving in sterile filtered DMSO, and the prepared working solution was diluted into medium (HL6 buffer or Schneider's medium) for the experiment. 200 nM TMRM in prepared medium was added to the dissected larvae or cultured cells for 20 minutes, then replaced with 50 nM TMRM for imaging. Images were obtained sequentially using 5% laser power, 488 nm excitation, for mito-GFP and 5%, 561 nm excitation for TMRM. Only non-overlapping axonal mitochondria were considered for quantification.

Mitochondrial inner membrane potential was quantified using *NIS-Elements AR 3.2* software. The ratio of mitochondrial fluorescence intensities (F_m) over cytoplasmic fluorescence intensities (F_c) was used to estimate mitochondrial membrane potential ($\Delta\Psi_m$, F_m/F_c) (Verburg and Hollenbeck, 2008; Shidara and Hollenbeck, 2010; Devireddy et al., 2014). To clarify the boundaries of axonal mitochondria, images were thresholded at an intensity of 400 to identify pixels belonging to mitochondria. Mitochondria were designated by *Polygonal ROI* for measuring F_m, and two square boxes (7 by 7 pixels) adjacent to the assigned mitochondrion were drawn by *Rectangular ROI* within cytosol for F_c measurement. Fluorescence intensity of F_m and F_c were determined from *MeanIntensity* with *ROI Area*, selected by *ROI Data*. To estimate $\Delta\Psi_m$, F_c was calculated as the mean of two *MeanIntensity* from the square boxes and the yielded F_m was divided by the calculated F_c. At least 5 axonal mitochondria were selected from individual animals and 10 mitochondria were selected from single culture dish for the $\Delta\Psi_m$ measurement.

2.8 Western Blotting

10 larvae or 20 adult fly heads were collected for each sample preparation. Collected samples were homogenized and lysed in 200 μl of lysis buffer containing 75 mM NaCl, 2.5 mM $MgCl_2$, 50 mM NaF, 0.1 mM EDTA, 0.5% Triton X-100 with protease inhibitor. Total proteins which were quantified by BCA protein assay kit (Pierce, #23227) were denatured by boiling with 40 μl of 6X sample buffer containing 6% SDS, 30% glycerin, 320 mM Tris-HCl and 3% β-mercaptoethanol for 10 minutes at 95^{o}C. Denatured samples were collected in 1.5 ml microfuge tubes, and supernatants were collected by centrifugation at 6,000 rpm for 10 minutes. Equal amount of proteins (30 - 60 μg) were loaded on precast gels with protein standard (Bio-Rad, #161-0973), and separated by SDS-electrophoresis. Gels were run at 200V for 30 minutes. After protein separation, proteins in the SDS gels were transferred onto nitrocellulose membranes at 350 mA for 90 minutes. Transferred membranes were cut for the different antibodies, and incubated in blocking solution (5% BSA in PBS) for 1 hour at room temperature with gentle shaking. After blocking, prepared primary antibodies were added into blocking solution, and the membranes in primary antibodies were incubated at 4^{o}C for overnight with gentle shaking. Membranes were washed three times with 0.1% PBST for 10 minutes, then secondary antibodies in blocking solution were prepared in the dark. Treated membranes were additionally incubated at room temperature in darkness for 1 hour and washed three times with 0.1% PBST for 10 minutes. Proteins were quantified and visualized by *Odyssey* detection. The antibodies used in this study were as follows: rabbit anti-parkin (74N and 278N 213.03) at 1:1,000 and mouse anti-actin at 1:5,000 for the primary antibodies, and goat anti-rabbit Alexa 680 (Invitrogen, #1073054) at 1:5,000 and goat anti-mouse Alexa 680 (Invitrogen, #1081875) at 1:5,000 for the secondary antibodies.

2.9 Immunostaining

For immunostaining of neuromuscular junctions, late third instar larvae were partially dissected (2.2.1) and fixed with 4% paraformaldehyde in 3 concavities glass slide for 20 minutes at room temperature (Shidara and Hollenbeck, 2010). Fixed samples were transferred to a 1.5 ml microfuge tubes, then washed twice with PBT (PBS containing 0.1% Triton X-100) for 15 minutes. Washed samples were blocked with PBTB (PBT containing 0.2% BSA) for 30 minutes, then stained with mouse anti-HRP (1:1000) that conjugated with Alexa594 goat anti-mouse (J.C. Clemens, Purdue University) for overnight at 4^{o}C. After incubation, immunostained samples were rinsed twice with PBTB for 30 minutes before mounting and observation. Images of immunostained neuromuscular junctions were taken between larval muscles 6 and 7 from A4 segmental nerves.

2.10 Statistical Analysis

To analyze data from *park*^{25} mutants compared to controls, *p*-values were calculated using an unpaired homoscedastic *t*-test. For multiple group comparisons, statistical significance was calculated by one-way ANOVA with Bonferroni correction *post* test. Significance between two populations was determined by two-sample Kolmogorov-Smirnov (K-S) test for analyzing the critical distribution. Correlations between two parameters were assessed by Pearson's correlation coefficient by R^2 values. In all cases, at least three independent experiments were performed. Number of experimental samples, mitochondria, axons, cell bodies, synaptic boutons, larvae and cells, were indicated in figures and figure legends. Error bars represent means ± SEM. All statistical significance was verified at $*p < 0.05$, $**p < 0.01$ and $***p < 0.001$ using *GraphPad Prism 5*.

CHAPTER 3. RESULTS

3.1 *park*^{25} Animals Display Loss of Parkin Expression

In order to elucidate the role of Parkin in mitochondrial quality control, I first generated *park*^{25} null mutants for comparison with control animals. Wild type flies expressing a single copy of mitochondrially-targeted GFP (mito-GFP) driven by the *D42* driver (Pilling et al., 2006) were used for the control (Table 2.1, #3), while *park*^{25} null mutants (Table 2.1, #6) were derived from crossing of *park*^{25}, *D42-Gal4/TM6B* (III) and *park*^{25}, *UAS-mitoGFP/TM6B* (III) (Greene et al., 2003). To confirm the deletion of *park*^{25} alleles (Figure 3.1, A), the protein expression was identified by western blot analysis. Here, the lysates were prepared from third instar larvae and adult heads respectively, and two antibodies (74N and 278N 213.03) were used for the Parkin detection. As expected, Parkin was not detected in *park*^{25} animals; though Parkin was not properly detected by 74N, the protein expression was faintly detected from either lysate of control animals by 278N 213.03 (Figure 3.1, B). This result confirms that *park*^{25} flies expressing mito-GFP in motor neurons described in this study are null alleles, and suggests that *park*^{25} flies will display the loss of Parkin function for understanding mitochondrial quality control.

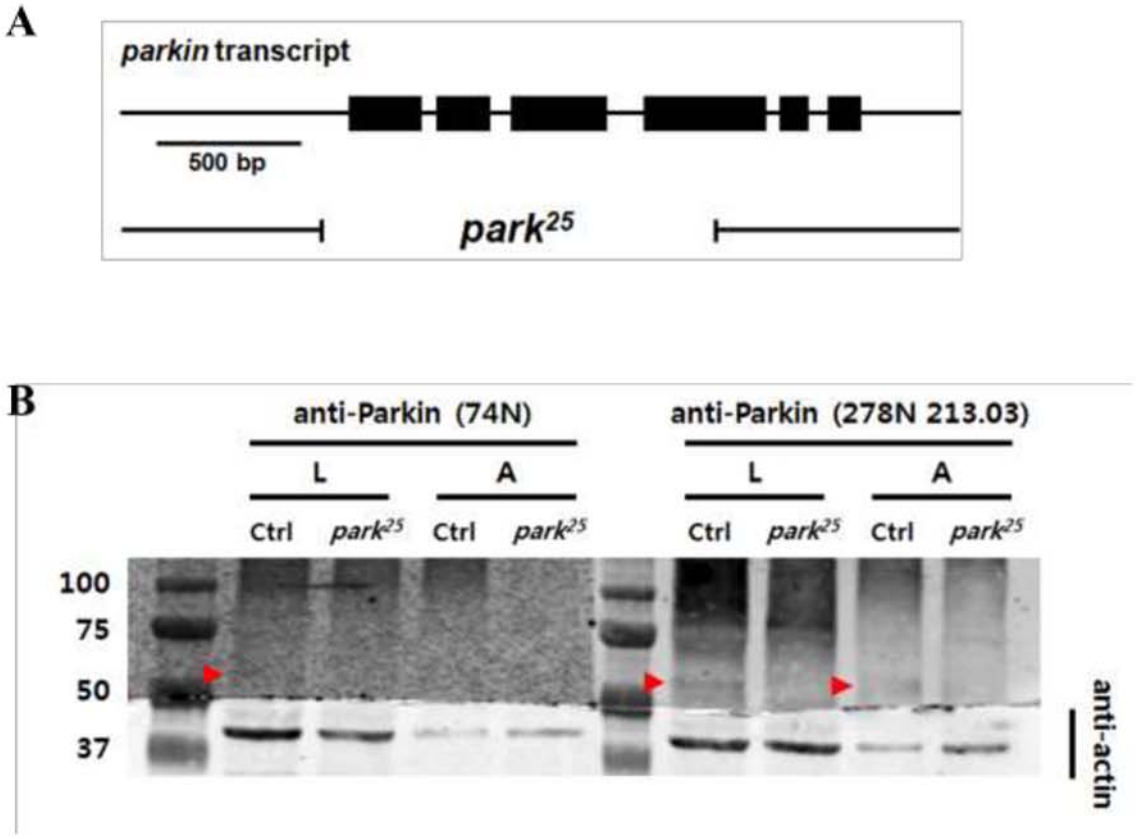

Figure 3.1 *park*^{25} mutant allele and Parkin expression. (A), Molecular map of the *parkin* transcript showing the breakpoint of the *park*^{25} deletion allele described in this study. The black boxes designate Parkin protein-coding sequences. (B), Western blot analysis of Parkin from third instar larvae (L) and adults (A) using two Parkin antibodies (74N and 278N 213.03). The red arrowheads indicate the size of Parkin, ~52 kDa. 30 µg of proteins are loaded. Size units are kDa.

3.2 Loss of Parkin Alters Mitochondrial Axonal Traffic

Currently, the cell body is predicted and proposed to be the major place where neuronal mitochondria are synthesized and degraded (Saxton and Hollenbeck, 2012). The PINK1/Parkin pathway has been proposed both to support mitochondrial quality control and turnover (Narendra et al., 2008; Matsuda et al., 2010; Narendra et al., 2010), and to regulate mitochondrial motility (Wang et al., 2011; Liu et al., 2012; Saxton and Hollenbeck, 2012). These two functions are likely to be related, as the return of senescent mitochondria to the cell body would require targeted net retrograde traffic. Thus, this current model raises the question of whether Parkin supports the axonal transport of senescent mitochondria for normal mitochondrial turnover processes.

3.2.1 *park*^{25} animals display reduced organelle flux

One strong expectation of current models is that Parkin deficiency will inhibit the turnover and retrograde traffic of mitochondria, causing an accumulation of senescent organelles in the axon. To test this hypothesis *in vivo*, I quantified the axonal transport of mitochondria in motor neurons of the intact *Drosophila* larval nervous system (Pilling et al., 2006; Russo et al., 2009). Using mitochondrially-targeted GFP (mito-GFP) driven by *D42,* transport was quantified in both directions in the proximal (segment A2), middle (A4) and distal (A7) regions of the segmental nerves (SNs), and was compared between control (wild type with *D42-Gal4>UAS-mitoGFP*) and *park*^{25} (*parkin* null) animals (Figure 3.2, A) (Devireddy et al., 2014). Consistent with previous analysis, mitochondrial flux in control motor axons was greater in the anterograde than retrograde direction, and declined with distance from the cell body in SNs (Shidara and Hollenbeck, 2010). In *park*^{25} SNs, flux was attenuated in both directions (Figure 3.2, B). Specifically, anterograde fluxes were more severely impaired than retrograde fluxes in *park*^{25} SNs; anterograde fluxes dropped to 48% (A2), 41% (A4) and 53% (A7) of control while retrograde fluxes dropped to 70% (A2), 53% (A4) and 61% (A7). In order to confirm that the reduced fluxes in *park*^{25} SNs were specifically affected by *parkin* perturbation, I

genetically over-expressed Parkin in null mutant lines by UAS-Parkin. Reduced fluxes in A4 SN of *park*^{25} were significantly rescued by Parkin over-expression, in both directions (Figure 3.2, B and C).

3.2.2 *park*^{25} animals display normal features of mitochondrial movements

Because this pathway has been proposed to specifically detach kinesin from the mitochondrial surface (Wang et al., 2011), we next examined whether reduced mitochondrial flux in *park*^{25} SNs derived from alteration of particular elements of mitochondrial motility. We analyzed the mitochondrial velocities, % moving, duty cycle and run length (Devireddy et al., 2014). In *park*^{25} SNs, mitochondrial velocities in both directions were similar to those of controls throughout the axons (Figure 3.3, A), and the percentages of moving and stationary mitochondria in motor axons were unaffected by Parkin deletion (Figure 3.3, B). This eliminated the major movement parameters as sources of the flux deficit, but we further measured the duty cycle and run length of moving mitochondria, and found that *park*^{25} mutants showed a modestly increased % of their time pausing during mitochondrial movement in both directions (Figure 3.3, C) caused by reduced proportion of movements in the dominant direction. However, the run lengths of moving mitochondria were similar, with only a small deficit in the A4 region of SNs (Figure 3.3, D). These data indicate that although the loss of Parkin significantly reduces mitochondrial flux in the axon, mitochondrial motility behaviors and the % of moving mitochondria are nearly unchanged.

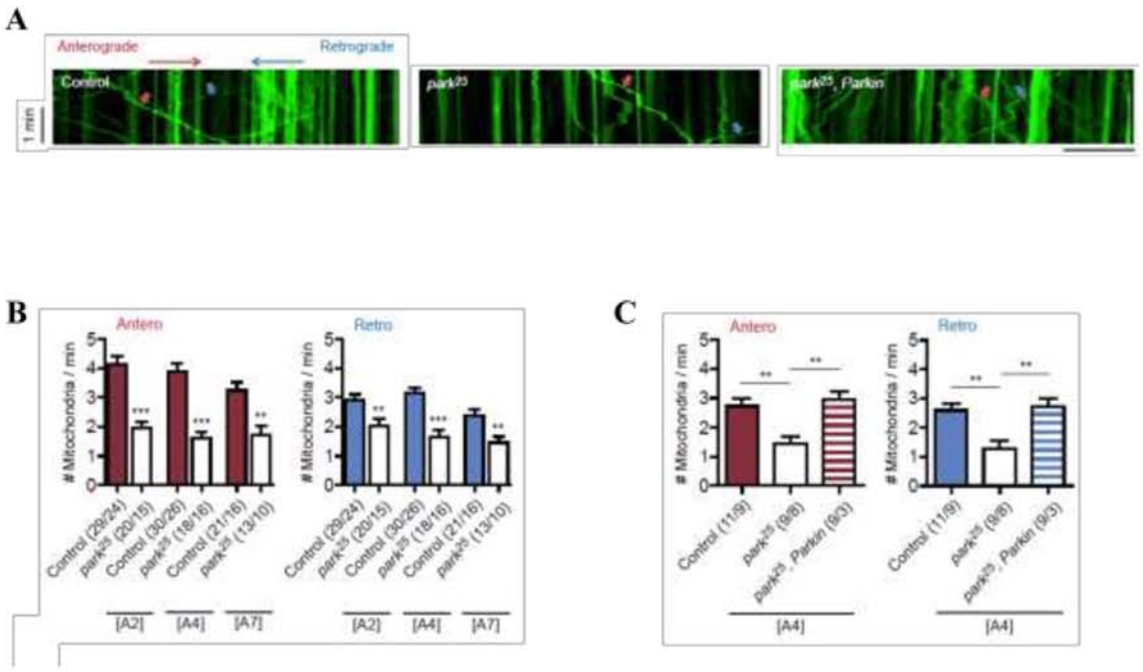

Figure 3.2 Parkin perturbation alters mitochondrial axonal traffic by reducing flux. (A), Representative kymographs of mitochondrial axonal transport from the A4 SNs. The red arrows indicate anterograde movements, while blue arrows indicate retrograde. Scale bar, 10 μm. (B), Mitochondrial flux in different *parkin* genotypes in A2, A4 and A7 SNs. $park^{25}$ mutants display attenuated mitochondrial flux in both directions throughout SNs. (C), Mitochondrial flux in *parkin* deletion and rescue, in A4 SNs. The attenuated mitochondrial flux in $park^{25}$ mutants is restored by *UAS-Parkin* expression. (*n*/*n*) = number of axonal regions/number of animals. Error bars indicate mean ± SEM. Significance is determined by Student's *t*-test (B) or by one-way ANOVA with Bonferroni correction (C). $^{**}p < 0.01$ and $^{***}p < 0.001$.

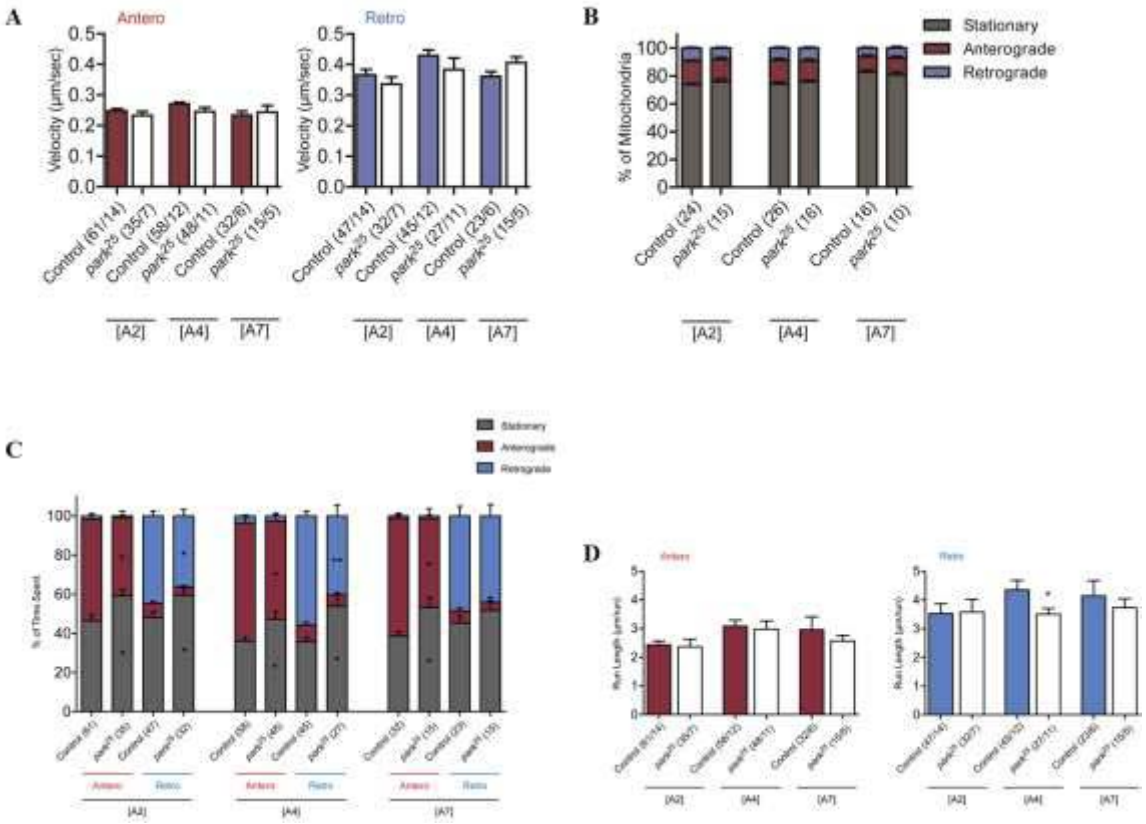

Figure 3.3 Parkin mutants show only modestly altered duty cycle and run length. (A), Mitochondrial net velocity in different *parkin* genotypes. *park*^{25} mutants retain normal mitochondrial velocities in both directions throughout the SNs. (*n*/*n*) = number of mitochondria/number of animals. (B), The percentages of moving and stationary mitochondria are unaffected in *park*^{25} SNs. (*n*) = number of animals. (C), Mitochondrial duty cycle in axons in different *parkin* genotypes. *park*^{25} mutants showed a modest increase in % of time pausing during mitochondrial movement in both directions. (*n*) = number of mitochondria. (D), Mitochondrial run lengths. *park*^{25} mutants showed a modest decrease in retrograde run length, only in the A4 region of SNs. (*n*/*n*) = number of mitochondria/number of animals. Mitochondrial duty cycles and run lengths were measured from moving mitochondria in axons in A2, A4 and A7 SNs. Error bars indicate mean ± SEM. Significance is determined by Student's *t*-test. **p* < 0.05 and ***p* < 0.01.

3.3 Loss of Parkin Produces Reduced Axonal Mitochondrial Density

If mitochondrial motility was essentially normal in *park*^{25} mutant animals, what could explain the large decrease in flux? One possibility is that Parkin deficiency reduces the number of mitochondria in the axon. This would run contrary to expectations, since the proposed role of the PINK1/Parkin pathway in mitochondrial turnover predicts that Parkin deficiency would cause the accumulation of senescent mitochondria (Narendra et al., 2008; Matsuda et al., 2010; Narendra et al., 2010). Nonetheless, I assessed this possibility by quantifying total mitochondrial density (both moving and stationary) in larval segmental nerves, motor synaptic boutons and axons from adult fly wing.

3.3.1 *park*^{25} animals display reduced axonal mitochondrial density in larval segmental nerves

I first considered organelle density in motor axons to verify the cause of reduced mitochondrial fluxes (Devireddy et al., 2014). There was clear and pronounced loss of axonal mitochondria throughout *park*^{25} motor axons: mitochondrial density within 50 μm axonal length was reduced to 51.70% (A2), 60.93% (A4) and 55.58% (A7) of control in *park*^{25} segmental nerves (Figure 3.4, A and B). This deficit was restored in A4 of *park*^{25} segmental nerves by Parkin over-expression (Figure 3.4, A and C). Though it was unexpected because of the proposed role of Parkin for targeting dysfunctional mitochondria (Narendra et al., 2008; Matsuda et al., 2010; Narendra et al., 2010), these results raise a possible idea to elucidate the cause of reduced mitochondrial fluxes that I found in *park*^{25} segmental nerves (Figure 3.2, B): that the altered mitochondrial flux in *park*^{25} motor axons results mainly from reduced organelle density.

3.3.2 *park*^{25} animals display reduced mitochondrial density in their motor synaptic boutons

Since *park*^{25} segmental nerves displayed reduced axonal mitochondrial density, I further monitored their neuromuscular junctions to verify whether there is any accumulation of mitochondria in *park*^{25} motor synaptic boutons. To quantify the density of mitochondria from motor synaptic boutons, neuromuscular junctions were stained with anti-HRP and selected between muscles 7 (M7) and 6 (M6) from the middle (A4) of the body wall. As in *park*^{25} segmental nerves, a reduced mitochondrial density is observed in synaptic boutons of *park*^{25} mutants (Figure 3.5, A and B). Together with Figure 3.4, these results suggest that *park*^{25} animals do not accumulate senescent mitochondria neither in segmental nerves nor in motor synaptic boutons.

3.3.3 *park*^{25} animals display reduced axonal mitochondrial density in adult fly wings

As described above, contrary to expectations, *park*^{25} animals do not accumulate senescent mitochondria either in segmental nerves or in motor synaptic boutons; rather, they display reduced axonal mitochondrial density. To confirm this deficit in *park*^{25} adult animals, I examined mitochondria in the wing, where a subset of sensory neurons express genes driven by *D42* driver, and these are situated along the wing margin (L0 vein and L1 vein) with L3 vein (Fang et al., 2012). I visualized *D42>mito-GFP* mitochondria in these sensory axons by observing the humeral crossvein (HCV) of LV1 (Figure 3.6, A and B). As in the larval nervous system, HCV axons of *park*^{25} mutant wings showed reduced mitochondrial density (Figure 3.6, C). However, unlike the larval segmental nerves, the deficit was not significantly restored by Parkin over-expression. Perhaps, Parkin expression may differ in developmental stage and/or after the animal metamorphosis. Collectively, this result consistently indicates that *park*^{25} animals also contain fewer axonal mitochondria and suggests that *park*^{25} animals display this reduced mitochondrial density in axons throughout their developmental stages.

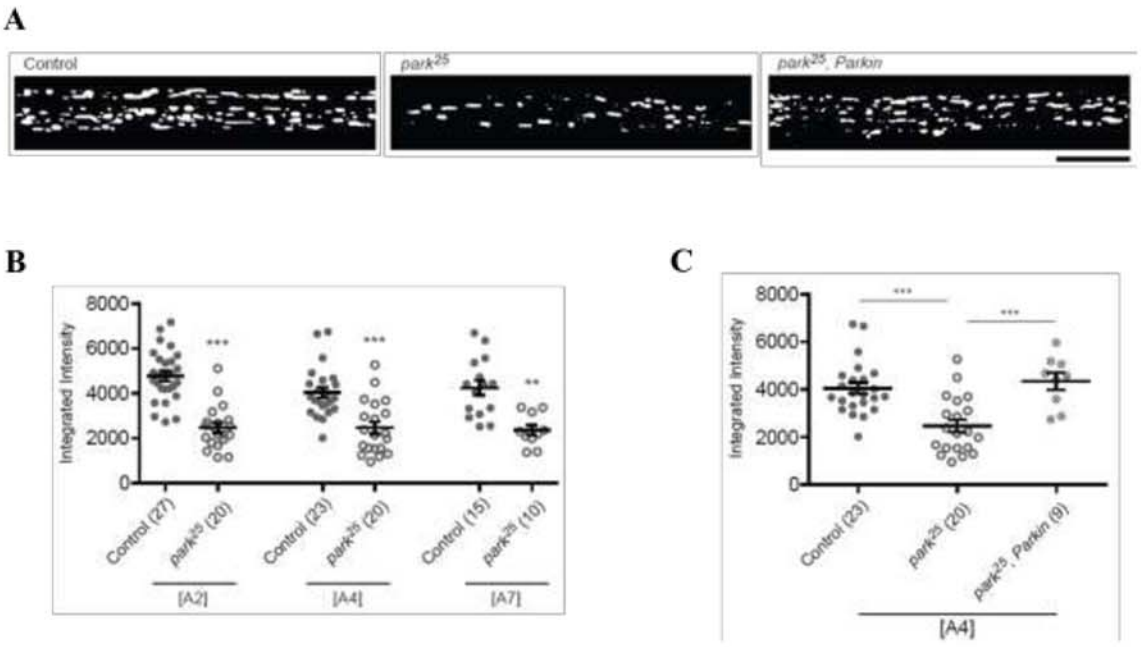

Figure 3.4 Reduced mitochondrial density is found in *park*^{25} motor axons. (A), Representative binarized images of mitochondria from the axon of A4 segmental nerves. Scale bar, 10 μm. (B), Axonal mitochondrial density measurements from different *parkin* genotypes in the A2, A4 and A7 regions show that density is decreased by half in *park*^{25} mutants throughout the axons. (C), Axonal mitochondrial density from different *parkin* genotypes in A4 segmental nerves show that the decreased density in *park*^{25} axon is restored by *UAS-Parkin* expression. (*n*) = number of animals. Error bars indicate mean ± SEM. Significance is determined by Student's *t*-test (B) or by one-way ANOVA with Bonferroni correction (C). $^{**}p < 0.01$ and $^{***}p < 0.001$.

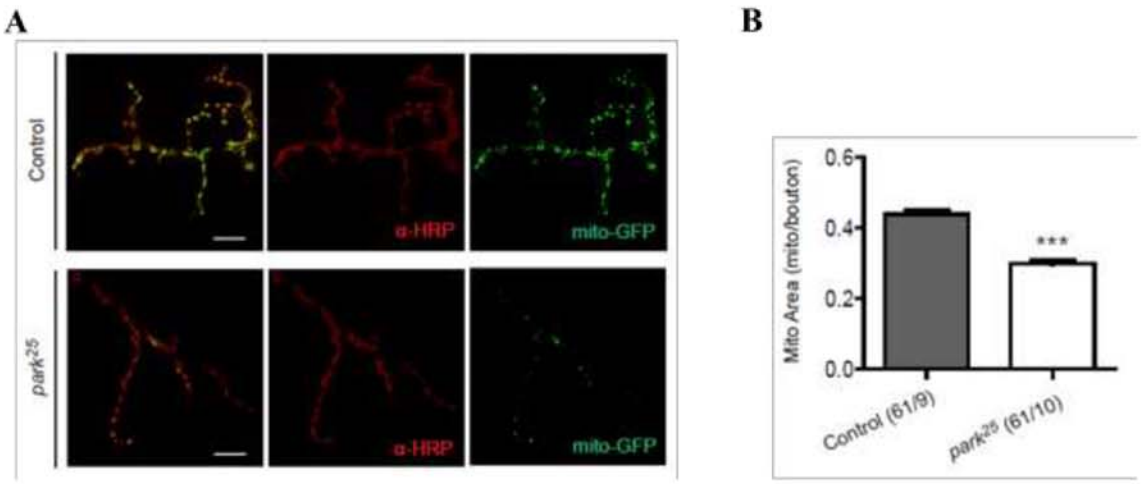

Figure 3.5 Reduced mitochondrial density is found in *park*^{25} motor synaptic boutons. (A), Images of mito-GFP (green) and anti-HRP staining (red) show mitochondria in motor synaptic boutons. Scale bars, 10 μm. (B), Mitochondrial density in motor NMJs. *park*^{25} mutants display reduced mitochondrial density in synaptic boutons. (*n*/*n*) = number of boutons/number of animals. Error bars indicate mean ± SEM. Significance is determined by Student's *t*-test. ***$p < 0.001$.

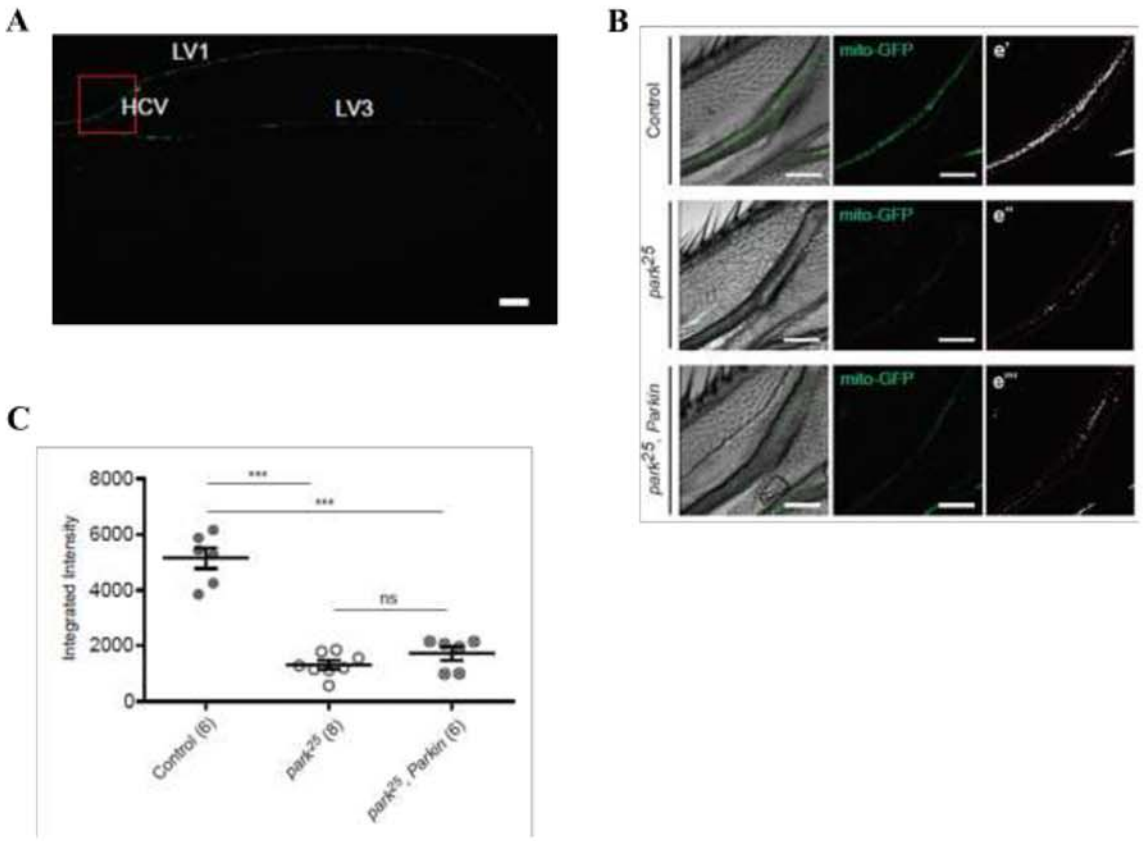

Figure 3.6 Reduced mitochondrial density is found in *park*^{25} fly wings. (A), Axonal mitochondria from 5d adult fly wing. Axons from the humeral crossvein (HCV; red box) of the first lateral vein (LV1) are monitored. Scale bar, 100 μm. (B), Axonal mitochondrial density in the HCV from different genotypes. Binarized images of mitochondria from the outlined area (e', e'' and e''') are quantified. (C), Quantitative data of axonal mitochondrial density in HCV. *park*^{25} mutants display reduced mitochondrial density in HCV. The deficit is not restored by *UAS-Parkin* expression in adult HCV. Scale bars, 50 μm. (*n*) = number of animals. Error bars indicate mean ± SEM. Significance is determined by one-way ANOVA with Bonferroni correction. ***p < 0.001.

3.4 Parkin Perturbation Produces Reduced Number of Motile Mitochondria

3.4.1 *park*^{25} animals display reduced number of steady-state moving mitochondria

The majority of mitochondria in axons are persistently stationary: 73.8 ± 0.82% (A2), 74.3 ± 1.46% (A4) and 82.9 ± 1.47% (A7) of axonal mitochondria were stationary in control animals, while 75.9 ± 1.94% (A2), 75.8 ± 1.32% (A4) and 80.8 ± 2.18% (A7) of axonal mitochondria were stationary in *park*^{25} animals (Figure 3.3, B). So next I separately assessed the density of moving mitochondria from larval motor axons to further analyze the relationship between axonal mitochondrial flux and density. Here, I monitored the number of steady state moving mitochondria over a time course from 30 μm photobleached axonal regions (Figure 3.7, A). By counting mitochondrial entry into bleached regions, I found a reduced steady state density of moving mitochondria in *park*^{25} axons and this reduction was partially rescued by Parkin over-expression (Figure 3.7, B). However, equal times were required to fill a bleached region to the steady state density of moving mitochondria: both control and *park*^{25} animals required ~ 210 seconds to reach plateau phase (Figure 3.7, B). Again, this suggests that reduced mitochondrial fluxes in *park*^{25} axons are mainly caused by reduced mitochondrial density rather than altered mitochondrial velocities.

To quantify the reduced mitochondrial density further in bleached regions, I also estimated the number of moving mitochondria from double reciprocal plots (Figure 3.7, C). 30 and 29 steady state moving mitochondria were estimated in control and *park*^{25}, *Parkin* animals respectively, while 17 steady state moving mitochondria were estimated in *park*^{25} mutants from the 30 μm photobleached regions: control from ($y = 0.033e^{63.612x}$), *park*^{25} from ($y = 0.059e^{58.643x}$) and *park*^{25}, *Parkin* from ($y = 0.035e^{63.741x}$). Thus, these data reconfirm that *park*^{25} segmental nerves contain less moving mitochondria, and reveal that the unexpected results of attenuated fluxes in *park*^{25} axons are mainly caused by a greatly reduced number of moving mitochondria.

3.4.2 Estimated numbers of steady-state moving mitochondria are consistent with numbers calculated from % of movement

Since I quantified the percentage of moving mitochondria by monitoring total amount of organelles (moving and stationary) from A4 segmental nerves (Figure 3.3, B), I tried to reconfirm the estimated number of steady state moving mitochondria by comparing with the numbers calculated with the % of movement. From A4 segmental nerves, the average number of total mitochondria within the assigned length (51.2 μm) was 180 in control, while 110 in *park*^{25}. And the mean % of moving mitochondria was 25.71% in control, while 24.21% in *park*^{25}. Since I photo-bleached 30 μm in the middle of segmental nerves, the calculated number of steady state moving mitochondria from control was 27.12 (180 × 30 / 50.2 × 0.2571) and from *park*^{25} was 15.60 (110 × 30 / 51.2 × 0.2421). As these numbers are close to 30 and 17 respectively, it reconfirms that *park*^{25} segmental nerves contain fewer moving mitochondria and consistently suggests that reduced mitochondrial axonal density produced by *parkin* deletion causes most of the reduction in mitochondrial transport in motor axons *in vivo*.

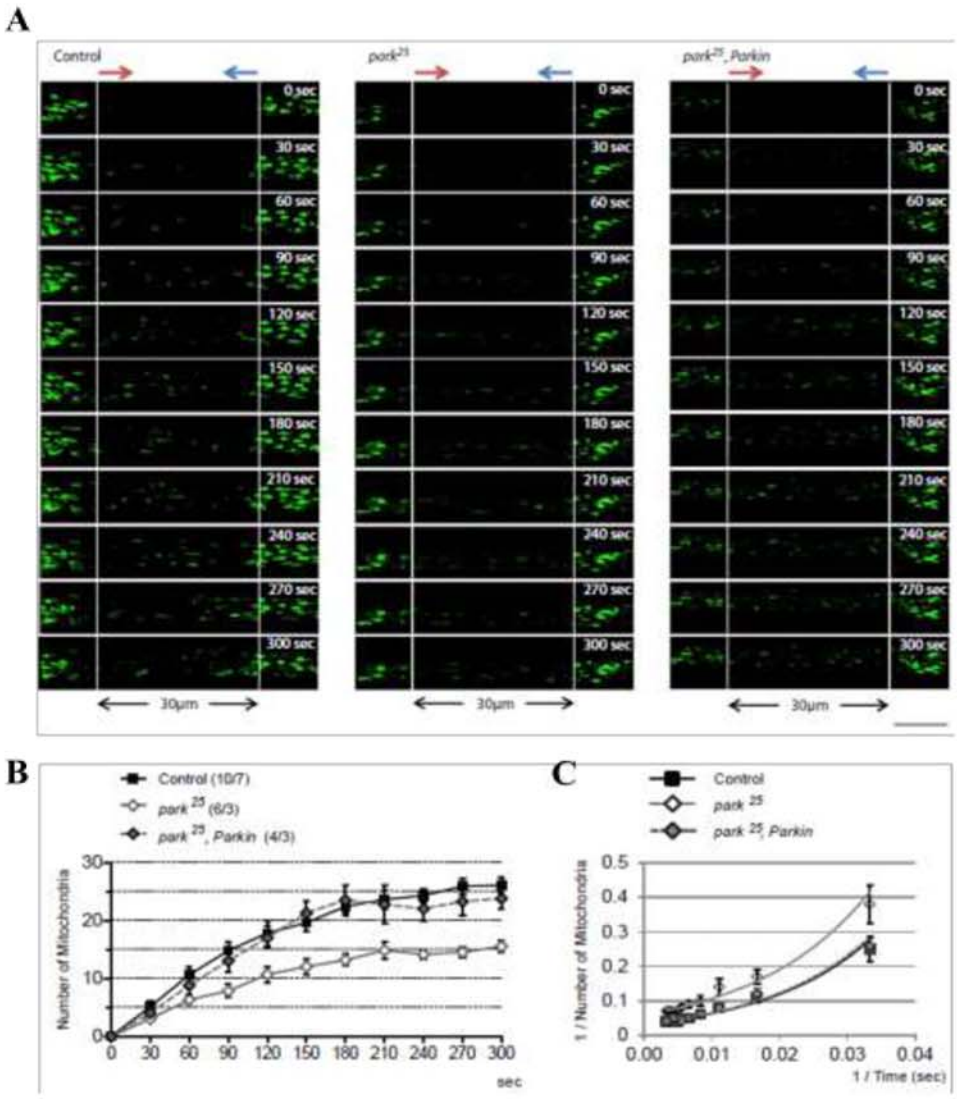

Figure 3.7 Reduced number of motile mitochondria is the cause of altered mitochondrial flux in *park*^{25} motor axons. (A), Images from 5 min time lapse of a photo-bleached region of axon in A4 segmental nerves. The steady-state numbers of moving mitochondria were quantified by monitoring their entry into the bleached regions (30 μm). Red arrows indicate the anterograde direction, blue indicates retrograde. Scale bar, 10 μm. (B), Number of moving mitochondria in the bleached region reaches steady-state at around 5 min. Mitochondria are counted every 30 seconds. (C), Double-reciprocal plots of the data in (B). The steady-state mitochondrial number is estimated from the extrapolated y intercepts. 30 and 29 steady-state moving mitochondria are estimated in control and *park*^{25}, *Parkin* animals, while 17 steady-state moving mitochondria are estimated in *park*^{25} mutants from the 30 μm photo-bleached regions. (*n*/*n*) = number of axonal regions/number of animals. Error bars indicate mean ± SEM.

3.5 Loss of Parkin Display Normal Status of Axonal Mitochondria

The Parkin pathway has also been proposed to keep senescent, depolarized mitochondria from fusing with normal ones by promoting the degradation of Mitofusin (Deng et al., 2008; Poole et al., 2010; Ziviani et al., 2010). Thus, another prediction of current models is that *park*^{25} mutants will display longer and/or enlarged mitochondria with lower inner membrane potential ($\Delta\Psi_m$).

3.5.1 *park*^{25} animals retain normal morphology of mitochondria in axons

As a reduced density of mitochondria was found in *park*^{25} motor axons, I further asked whether those remaining axonal mitochondria have normal or compromised mitochondrial morphology. I first measured the length of both stationary and moving axonal mitochondria in controls, and found that the mean length of moving mitochondria was 0.8 times that of stationary ones in general. Surprisingly, the mean length of either stationary or moving mitochondria from segmental nerves was not affected by *parkin* perturbation (Figure 3.8, A). Mean length of stationary mitochondria was 1.54 ± 0.01 μm in control and 1.55 ± 0.01 μm in *park*^{25}, while mean length of moving mitochondria was 1.38 ± 0.03 μm in control and 1.28 ± 0.03 μm in *park*^{25}. To elucidate whether a length difference in *park*^{25} mutants might be manifested not in the population average, but as a small outlying population of longer mitochondria, I also examined the length distribution by a two-sample Kolmogorov-Smirnov test (Figure 3.8, B). However, there was no significant difference between control and *park*^{25} mutants, for either moving or stationary mitochondria: K-S statistics from each of stationary and moving mitochondrial length were smaller than critical distribution. Thus, these data indicate that axonal mitochondrial length is not affected by *parkin* perturbation which contradicts the idea that Parkin controls fission-fusion steady state.

Next, I further measured the projected area of axonal mitochondria to confirm whether *park*^{25} mutants show any shape differences in axonal mitochondria. However, area of mitochondria in *park*^{25} SNs was comparable to control throughout the axons

(Figure 3.9, A and B): 0.82 ± 0.01 μm^2 with 0.56 μm mean height in control and 0.79 ± 0.01 μm^2 with 0.56 μm mean height in *park*^{25}. Collectively, these *in vivo* data from morphological analysis indicate that Parkin seems to be dispensable for maintaining normal mitochondrial morphology in motor axons.

3.5.2 *park*^{25} animals retain normal inner membrane potential of mitochondria in axons

To test whether the remaining axonal mitochondria in *park*^{25} mutants nonetheless display normal membrane potential, I assessed the $\Delta\Psi_m$ of mitochondria from intact larval motor neurons. Tetramethylrhodamine methyl ester (TMRM) was used for determination of mitochondrial transmembrane potential. Since the fluorescent probe of TMRM does not successfully penetrate into the larval segmental nerves due to their connective tissue sheet (Figure 3.10, A), axonal mitochondria within axons of thin nerves adjacent to the larval A4 segment were selected for *in vivo* quantification (Verburg and Hollenbeck, 2008; Shidara and Hollenbeck, 2010; Devireddy et al., 2014; Devireddy et al., 2015). The acquired TMRM images were thresholded at an intensity of 400 to identify pixels belonging to mitochondria and to determine the mitochondrial fluorescence intensities (F_m), while the mean intensity of two area boxes (7 by 7 pixels) adjacent to the assigned mitochondria was used to determine the cytoplasmic fluorescence intensities (F_c). The ratio of mitochondrial to cytoplasmic fluorescence intensities (F_m/F_c) was used as a logarithmic quantification of mitochondrial inner membrane potential ($\Delta\Psi_m$) (Verburg and Hollenbeck, 2008; Shidara and Hollenbeck, 2010). Surprisingly, mitochondrial $\Delta\Psi_m$ was properly maintained in thin axons of *park*^{25} SNs (Figure 3.10, B and C), and the reduced axonal mitochondrial density observed in segmental nerves was also apparent in these thin nerves (Figure 3.10, B).

3.5.3 *park*^{25} animals retain normal inner membrane potential of mitochondria in neuromuscular junctions

The *in vivo* data from larval motor neurons indicate that there is lack of the predicted accumulation of senescent mitochondria in *park*^{25} mutant axons. Instead, I found a reduced number of mitochondria not only from mutant axons (Figure 3.4) but also from mutant neuromuscular junctions (Figure 3.5). This raises an additional question whether those remaining mitochondria in *park*^{25} mutant synaptic terminal also retain normal metabolic state. To verify this issue, I assessed the $\Delta\Psi_m$ of mitochondria from larval neuromuscular junctions of A4 segments, and found that the remaining mitochondria in *park*^{25} synaptic boutons display preserved a normal inner membrane potential (Figure 3.11, A and B). I also quantified the distribution of TMRM intensity to understand whether a difference of mitochondrial $\Delta\Psi_m$ in *park*^{25} mutants might be manifested not in the population average, but as a small outlying population of diminished $\Delta\Psi_m$ of mitochondria, and found a comparable distribution of TMRM intensity between control and *park*^{25}: K-S statistics show no significant difference between two groups (Figure 3.11, C). Collectively, these results thus suggest that Parkin perturbation fails to produce the predicted accumulation of enlarged, longer and senescent mitochondria both in motor axons and in synaptic terminal *in vivo*; *park*^{25} mutant animals display normal status for their axonal mitochondria.

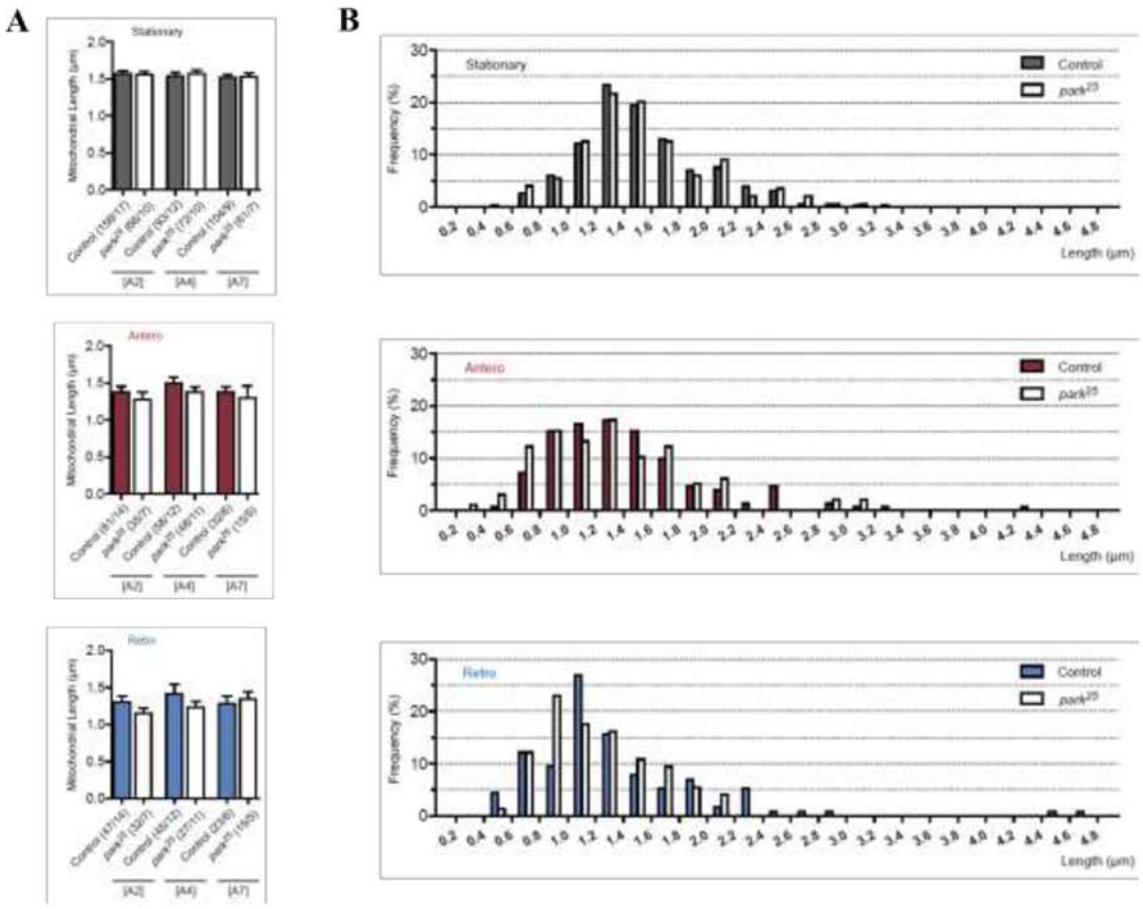

Figure 3.8 Normal mitochondrial length is maintained in motor axons of *park*^{25} mutants. (A), Mean length of axonal mitochondria in different *parkin* genotypes. Stationary and moving mitochondria are measured in axons of A2, A4 and A7 SNs. Normal mitochondrial length is preserved in *park*^{25} mutants throughout the SNs. (B), Length distribution of axonal mitochondria in different *parkin* genotypes. Stationary, anterograde and retrograde mitochondria from axons are separately analyzed. There is no outlying population of longer mitochondria in *park*^{25} mutant axons. (*n*/*n*) = number of mitochondria/number of animals. Error bars indicate mean ± SEM. Significance is determined by Student's *t*-test (A) and data are assessed by a two-sample Kolmogorov-Smirnov test (B, no significant difference between any of the control-*parkin* mutant pairs).

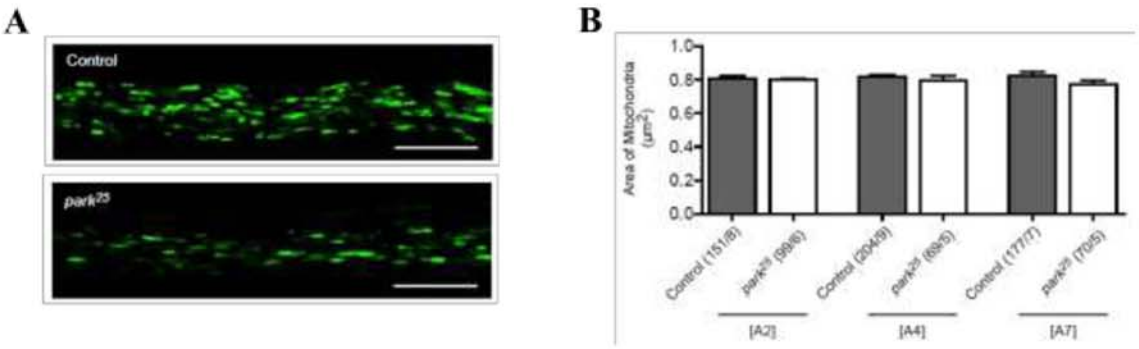

Figure 3.9 Normal mitochondrial morphology is maintained in motor axons of *park*^{25} mutants. (A), Representative images of axonal mitochondrial morphology from A4 SNs. Scale bars, 10 μm. (B), Area of mitochondria in motor axons. Normal projected area of axonal mitochondria is retained in *park*^{25} mutant axons. (*n*/*n*) = number of mitochondria/number of animals. Error bars indicate mean ± SEM. Significance is determined by Student's *t*-test.

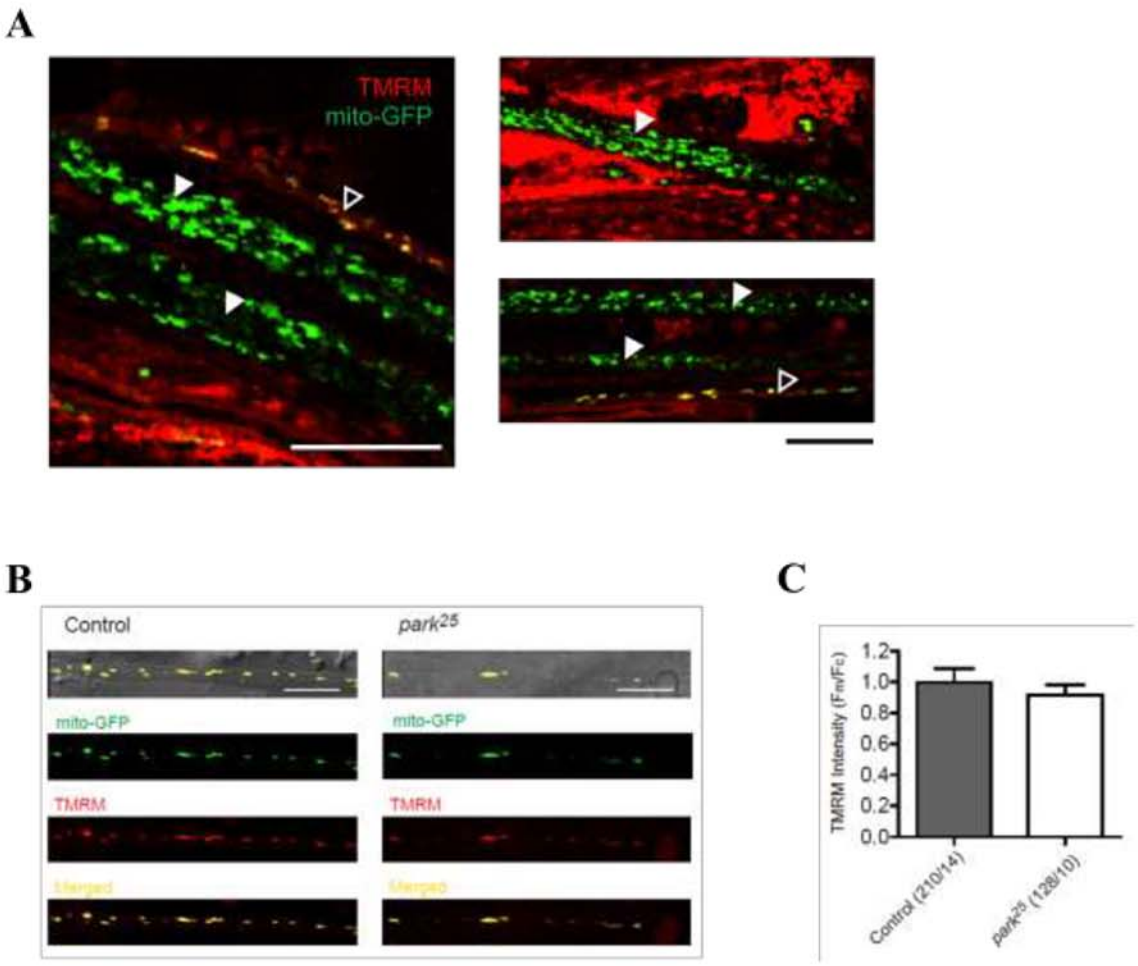

Figure 3.10 Normal mitochondrial inner membrane potential ($\Delta\Psi_m$) is maintained in motor axons of *park*^{25} mutants. (A), Representative TMRM (red) stained images of axonal mitochondria with mito-GFP (green) from the larval A4 segmental nerves. Mitochondria are stained with TMRM to indicate inner membrane potential ($\Delta\Psi_m$), while mito-GFP reveals all axonal mitochondria. Note that mitochondria only in single axon (open arrowheads) are successfully stained by TMRM, whereas TMRM did not penetrate into axon bundles (blocked arrowheads). Scale bar, 20 µm. (B), Representative TMRM stained images of axonal mitochondria with mito-GFP from thin nerve adjacent to the A4 segment. Note that mito-GFP here confirms the lower mitochondrial density in *park*^{25} axons compared to controls. Scale bars, 10 µm. (C), Mean F_m/F_c intensity ratio of TMRM from neurons in different *parkin* genotypes. Normal mitochondrial inner membrane potential is retained in *park*^{25} mutant axons. (*n*/*n*) = number of mitochondria/number of animals. Error bars indicate mean ± SEM. Significance is determined by Student's *t*-test.

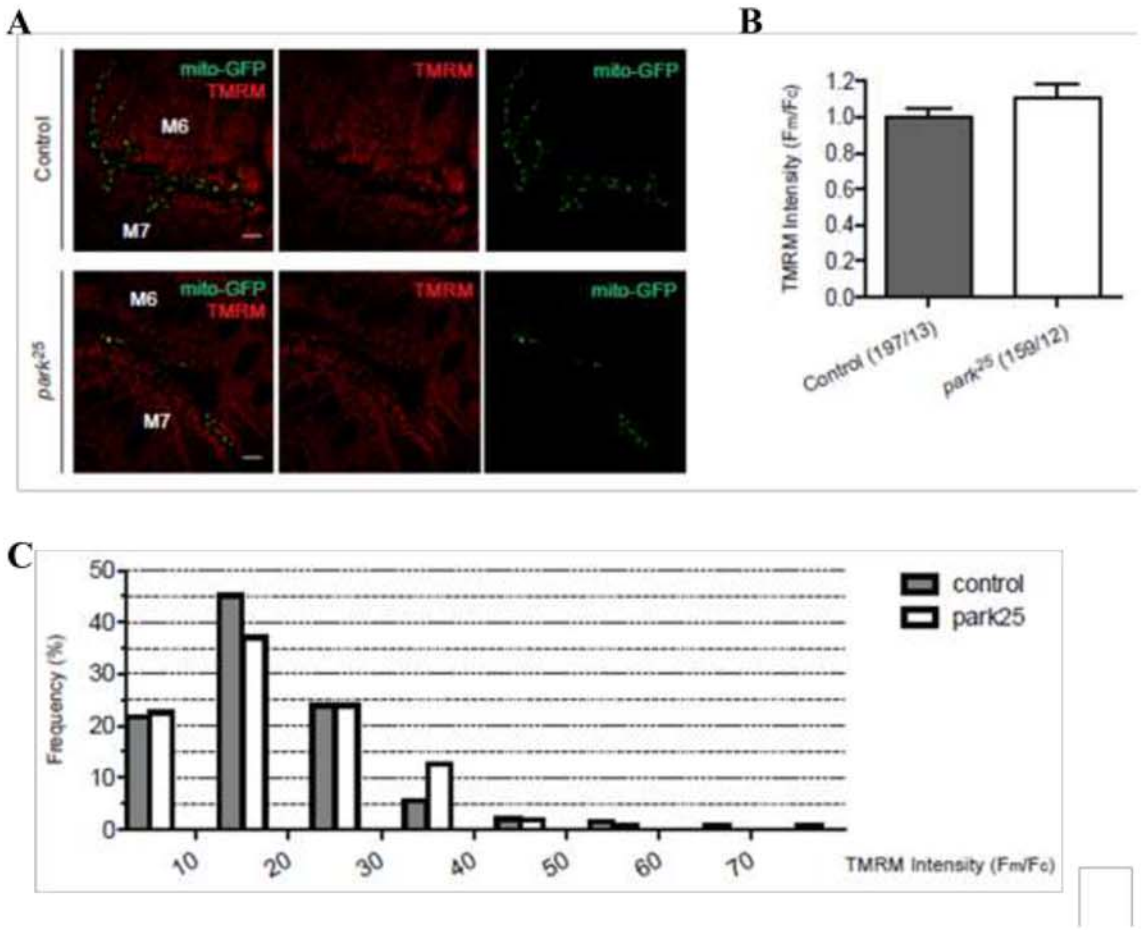

Figure 3.11 Normal mitochondrial inner membrane potential ($\Delta\Psi_m$) is maintained in neuromuscular junctions of *park*^{25} mutants. (A), Representative TMRM staining images of mitochondria with mito-GFP from NMJs. NMJs are taken between muscles 7 (M7) and 6 (M6) from A4 SNs, and mitochondria in synaptic boutons are selected for $\Delta\Psi_m$ quantification. Scale bars, 10 μm. (B), Mean F_m/F_c intensity ratio of TMRM from NMJs in different genetic backgrounds. Normal $\Delta\Psi_m$ is retained in synaptic boutons of *park*^{25} NMJs. (C), TMRM intensity distribution of mitochondria in NMJs. (*n*/*n*) = number of mitochondria/number of animals. Error bars indicate mean ± SEM. Significance is determined by Student's *t*-test (B) or by two-sample Kolmogorov-Smirnov test (C, K-S statistics show no significant difference).

3.6 Correlation between Axonal Mitochondrial Length and Velocity

Having already measured net velocities of moving mitochondria for quantifying axonal transport, I then regressed mitochondrial velocities against their lengths to understand any relationship between transport and morphology. Although lengths were distributed from 0.35 μm to 4.65 μm, the net velocities of mitochondria were consistent in both directions. There was no correlation between mitochondrial length and velocity or direction of movement (Figure 3.12). Determination of correlation coefficient (R^2) from each groups verified no difference: anterograde mitochondria from control ($R^2 = 0.0097$), retrograde mitochondria from control ($R^2 = 0.0059$) and anterograde mitochondria from *park*^{25} ($R^2 = 0.0155$), retrograde mitochondria from *park*^{25} ($R^2 = 0.031$). Though this seems counterintuitive on its face, it is consistent with previous studies that have shown no effect of mitochondrial length on axonal motility except at extreme, non-physiological lengths (Amiri and Hollenbeck, 2008).

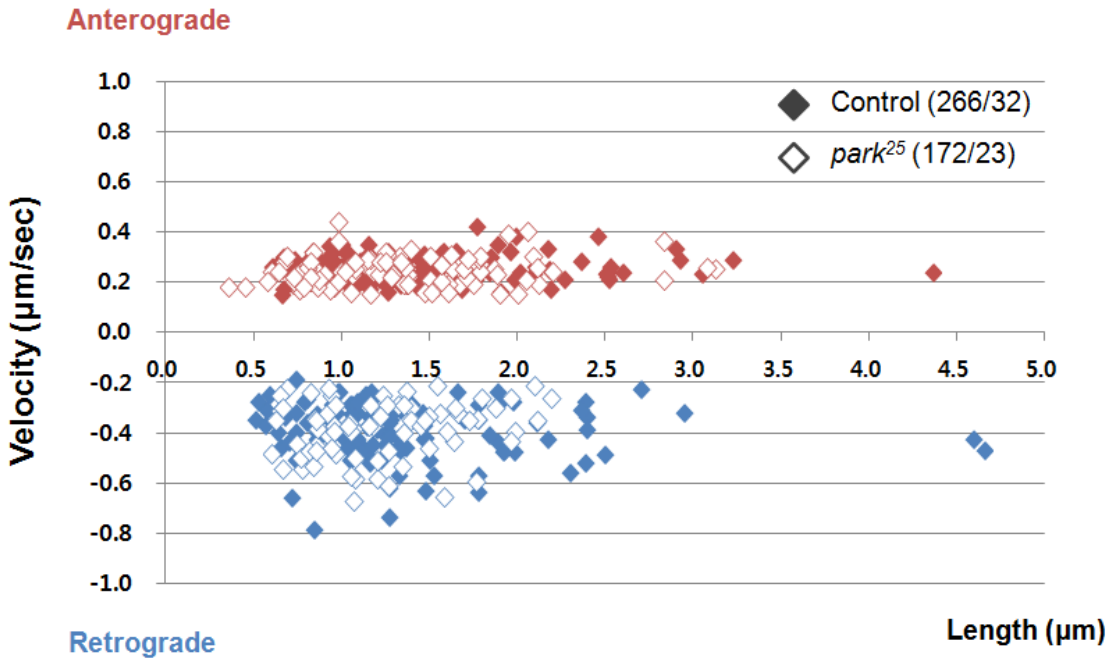

Figure 3.12 Relationship between axonal mitochondrial velocity and length in motor neurons. Individual moving mitochondria in larval motor axons are plotted by their length and velocity. Correlation coefficients are verified by R^2 values: no correlation between two variables, R^2 values ≤ 0.65 (anterograde mitochondria from control (R^2 = 0.0097), retrograde mitochondria from control (R^2 = 0.0059) and anterograde mitochondria from *park*^{25} (R^2 = 0.0155), retrograde mitochondria from *park*^{25} (R^2 = 0.031)). (*n*/*n*) = number of mitochondria/number of animals.

3.7 Parkin Deficit Produces Abnormal Mitochondrial Morphology in Motor Cell Bodies

The observed defects - a reduced number of mitochondria with normal organelle status - in *park*^{25} axons contradicted the predicted expectation that senescent mitochondria would accumulated due to *parkin* perturbation. This raised the possibility that the cell body itself is the main locus of Parkin-dependent turnover and/or Parkin-dependent mitochondrial biogenesis, perhaps including regulation of mitochondrial entrance into the axon. Thus, I further analyzed the morphology of mitochondria in motor cell bodies of the larval nervous system. Interestingly, abnormal morphologies, tubular and reticular, of mitochondria were found in *park*^{25} motor cell bodies (Figure 3.13, A). To quantify these complex differences in organelle morphology, I categorized the mitochondria into four different types by their morphological appearances - fragmented (1), wild type (2), tubular (3) and hyper-fused (4) - and scored them while blinded to the genotype. Interestingly, a higher frequency of tubular and hyper-fused mitochondria was formed in *park*^{25} motor cell bodies: 7.5 % of tubular (3) and 0.0 % of hyper-fused (4) were formed in controls, while 54.2 % of tubular (3) and 26.4 % of hyper-fused (4) were formed in *park*^{25} (Figure 3.13, B). To further confirm the role of Parkin in mitochondrial morphology in motor cell bodies, I over-expressed Parkin by *UAS-Parkin* and the morphological deficit was partially restored (Figure 3.13, A and B). Therefore, these data demonstrate that in contrast to motor axons (Figure 3.8 and 3.9), in cell bodies Parkin is essential for the maintenance of normal mitochondrial morphology. Along with the data from Figure 3.7, these results also indicate the importance of Parkin in mitochondrial interconnected network within neuron that Parkin is critical for both normal mitochondrial morphology in the cell body and their entry into the axon, and suggest a likely relation of the two: that normal somatic organelle morphology, reflecting a normal fission-fusion balance, is significant for producing and/or launching axonal mitochondria.

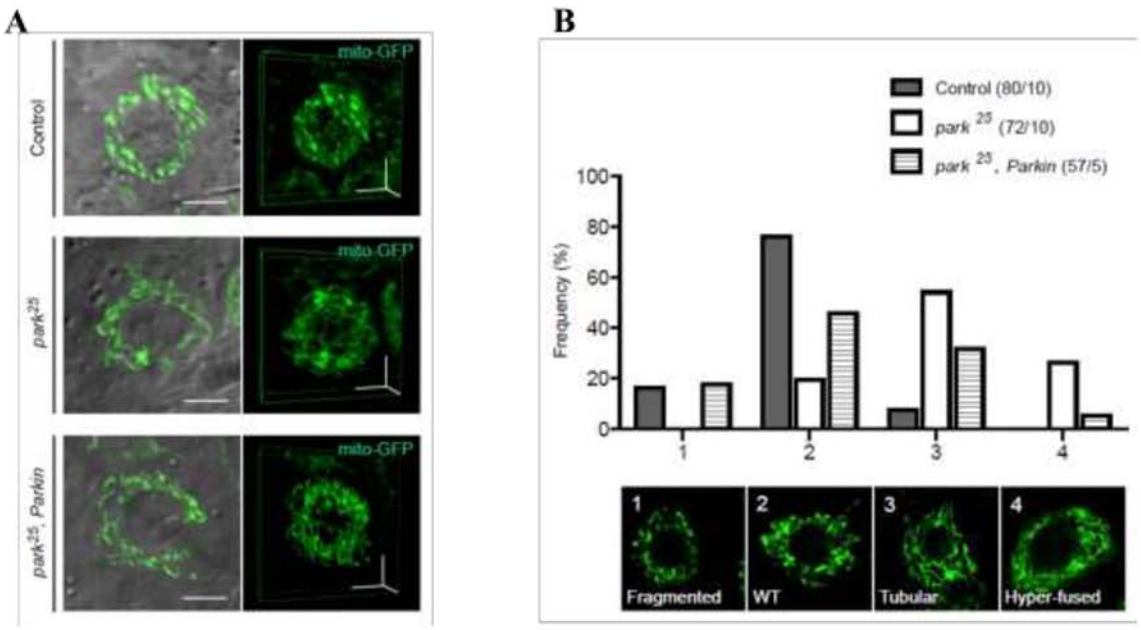

Figure 3.13 Parkin perturbation produces tubular, inter-connected mitochondria in cell bodies. (A), Representative plane and 3 dimensional reconstructed images of the mitochondria in motor cell bodies. Reconstructed images are generated from sections of 20 μm width (x), 20 μm height (y) and 5 μm depth (z) using 100 frames to construct the z stacks. Scale bars, 5 μm. (B), Mitochondrial morphology in cell bodies of different *parkin* genotypes. Mitochondrial morphology is categorized as: 1, fragmented; 2, wild type; 3, tubular; or 4, hyper-fused. Tubular and hyper-fused morphological defects of mitochondria are observed much more frequently in $park^{25}$ cell bodies. Morphological defects of mitochondria in $park^{25}$ cell bodies are partially restored by *UAS-Parkin* expression. (*n*/*n*) = number of cell bodies/number of animals. Data are generated by analysis blinded to the genotype in the images and assessed by a two-sample Kolmogorov-Smirnov test (morphological changes of mitochondria caused by Parkin null are significantly different from control; $D = 0.7306 > critical\ D = 0.2209$ with a corresponding $p < 0.001$).

3.8 Parkin-dependent Mitophagy Is Undetectable in Motor Neurons *In Vivo*

Studies in embryonic neurons *in vitro* have shown that autophagosomes arise in the distal axon and undergo maturation during their retrograde transport (Maday et al., 2012; Maday and Holzbaur, 2014). Since the PINK1/Parkin pathway is thought to be necessary for local mitophagy in the distal axon (Ashrafi et al., 2014), the lack of evidence for Parkin-dependent axonal mitochondrial turnover that I found here was surprising and raised the question of whether Parkin is actually responsible for local mitophagy processes *in vivo*. To understand further the role of Parkin in neuronal mitophagy, I visualized simultaneously mitochondria and autophagic vacuoles in *Drosophila* larval motor neurons (Figure 3.14): mitochondria were visualized by mito-GFP, while autophagic vacuoles (AVs) were visualized by RFP-atg8 in motor neurons driven by *D42* driver.

3.8.1 No detectable co-localization of mitochondria with autophagic vacuoles in motor cell bodies *in vivo*

As I already observed the altered morphology of mitochondria in the cell bodies, I first tried to quantify the co-localization of autophagosomes with mitochondria from the motor cell bodies to examine whether Parkin plays a critical role in targeting dysfunctional mitochondria. Consistent with my previous data (Figure 3.13), tubular and elongated mitochondria were found in $park^{25}$ cell bodies. However, mitochondria almost completely failed to co-localize with autophagic vacuoles in either control or $park^{25}$ cell bodies (Figure 3.15, A and B): signals from intensity profiles (a', a'' and b', b'') represent discrete organelle particles. Since autophagic vacuoles barely co-localized with mitochondria even under basal conditions, I prevented larvae from feeding for 6 hours before observation to trigger starvation-induced autophagy (Gomes et al., 2011; Rambold et al., 2011; Ghosh et al., 2012). Though this treatment caused the expected mitochondrial fragmentation (Gomes et al., 2011; Rambold et al., 2011), which should render mitochondria even better candidates for engulfment, the co-localization of

autophagic vacuoles with mitochondria was still not detected from either control or *park*^{25} cell bodies (Figure 3.15, A and B): signals from intensity profiles (c', c'' and d', d'') represent discrete organelle particles. Thus, in cell bodies I could not test the hypothesis that Parkin deficiency would reduce the rate of mitophagy *in vivo*, because there was no detectable mitophagy even in controls under either normal physiological or starvation-induced autophagic conditions.

3.8.2 No detectable co-localization of mitochondria with autophagic vacuoles in motor axons *in vivo*

Although there was no detectable co-localization of autophagosomes with mitochondria in motor cell bodies from our *in vivo* larval system, it remained possible that mitophagosomes arose in the distal axon and completed degradation during retrograde transport, making autophagosome-mitochondria co-localization undetected in cell bodies. Thus, I monitored autophagic vacuoles along the axon to elucidate whether the mitophagy process can occur during the autophagic maturation. However, in axons, as in cell bodies I observed a striking lack of co-localization of autophagic vacuoles with mitochondria in either control or *park*^{25} animals (Figure 3.16, A - D). Thus, these results indicate that the mitophagy process is essentially absent *in vivo* at least in the form of mitochondrial engulfment by autophagosomes.

As expected from previous studies (Maday et al., 2012), axonal autophagic vacuoles mainly moved retrogradely and rarely changed their direction, while mitochondria showed pauses and/or salutatory, bidirectional movements (Figure 3.17, A). In general, the majority of retrograde moving autophagic vacuoles displayed faster movement than those of moving mitochondria. To understand whether Parkin is involved in organelle axonal transport, I simultaneously analyzed axonal movements of mitochondria and autophagic vacuoles by flux measurement. Consistent with the previous data (Figure 3.2), mitochondrial flux was greater in the anterograde than retrograde direction, and the fluxes were reduced by *parkin* perturbation in both directions (Figure 3.17, B). Unlike mitochondria, autophagosomes displayed a higher

flux in the retrograde direction than in anterograde. Interestingly, autophagic vacuole flux was also substantially reduced in *park*^{25} mutants, but specifically in the retrograde direction (Figure 3.17, C): *park*^{25} mutants showed anterograde AV flux equal to that of control, while retrograde flux was reduced by 50%. Collectively, these results indicate that while autophagic vacuoles are apparent and their axonal transport is consistent with them having a Parkin-dependent origin and/or maturation in the distal axon, mitophagy is so rare as to be undetectable in motor neurons *in vivo*.

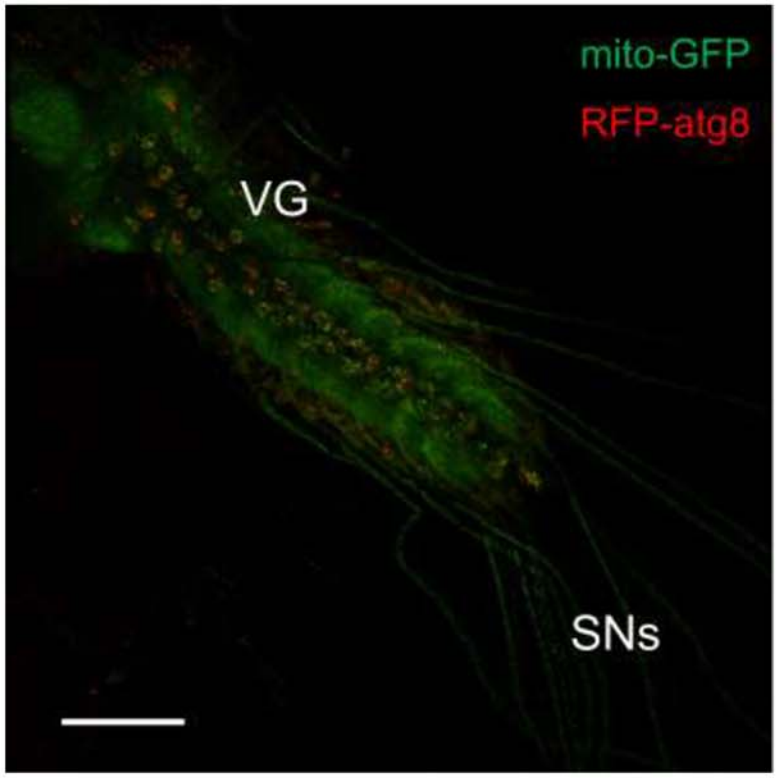

Figure 3.14 Dissected late third instar larva expressing mito-GFP and RFP-atg8 in motor neurons. Mitochondria (green) are monitored with autophagosomes (red) at cell bodies in the ventral ganglion (VG) and at axons in the segmental nerves (SNs). Scale bar, 100 μm.

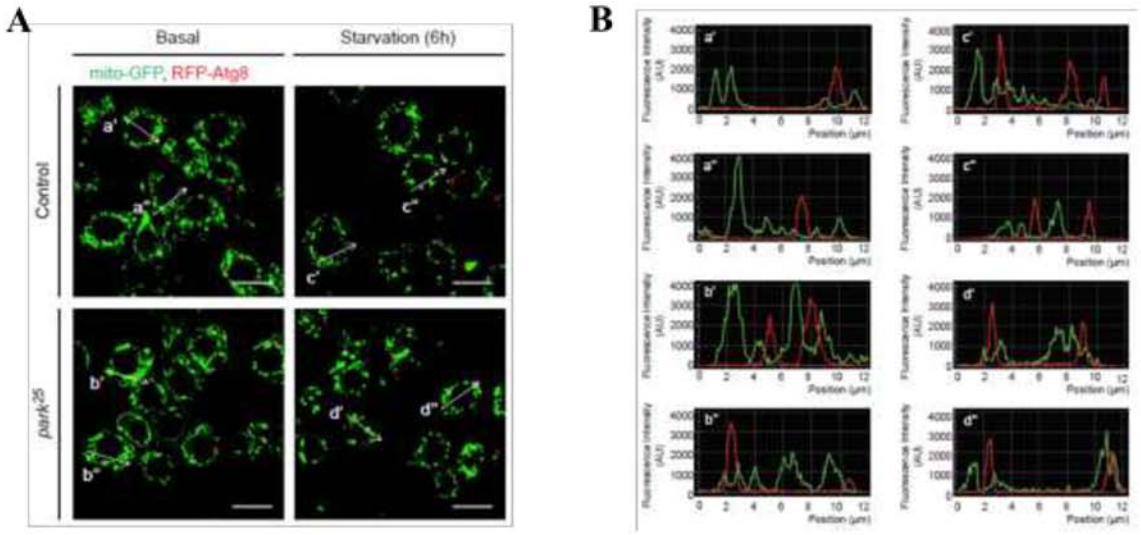

Figure 3.15 Mitochondria do not co-localize significantly with autophagic vacuoles in motor cell bodies *in vivo*. (A) Representative images of cell bodies in different *parkin* genotypes. mito-GFP fluorescence was used to identify mitochondria (green) and RFP-Atg8 to identify AVs (red). Autophagy was induced by 6 hour starvation. White arrows indicate lines along which organelle co-localization was analyzed for basal (a', a'' and b', b'') and starvation (c', c'' and d', d'') conditions. Scale bars, 10 μm. (B), Respective signal intensity profiles from the line scans indicated in (A). Distinct mito-GFP and RFP-Atg8 signals reveal no clearly detectable mitophagy events in motor cell bodies from either genotype. AU, arbitrary units.

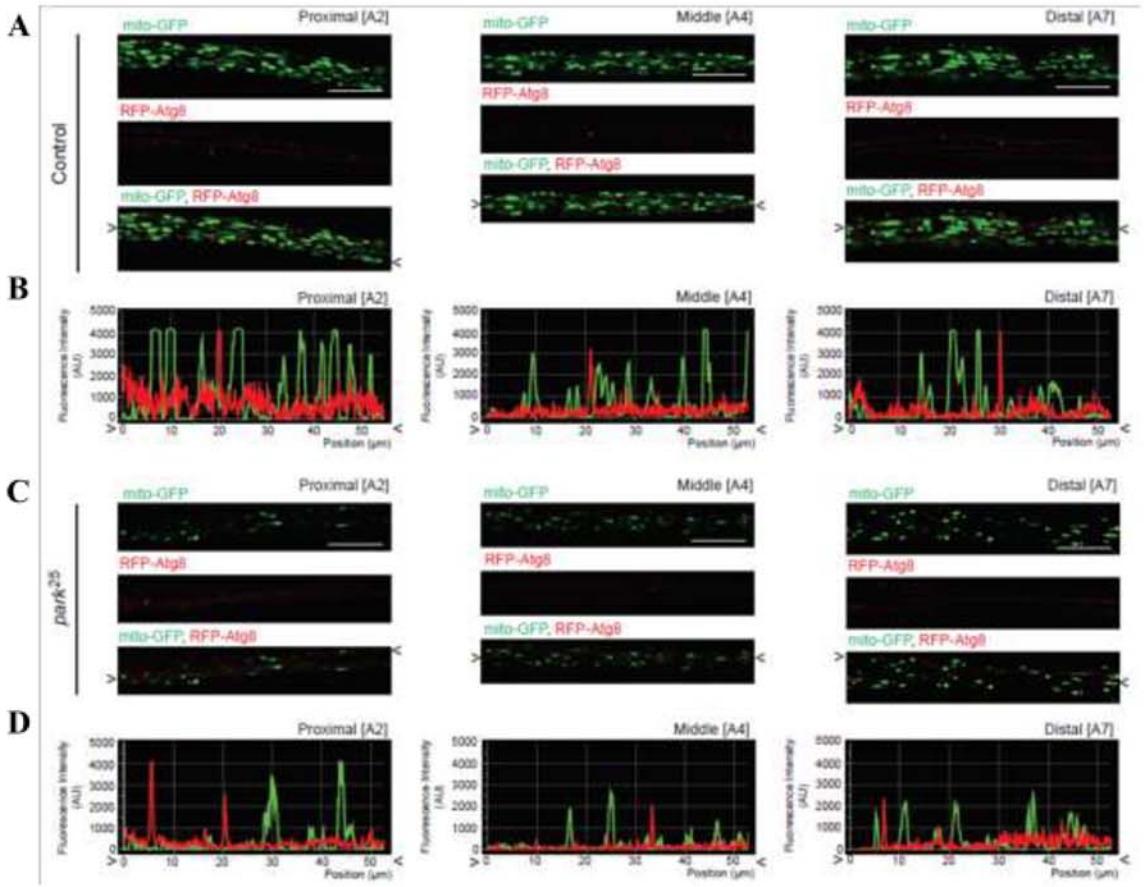

Figure 3.16 Mitochondria do not co-localize significantly with autophagic vacuoles in motor axons *in vivo*. (A), Representative images of axonal mitochondria with AVs in A2, A4 and A7 SNs from control animals. Organelle co-localization is represented by oblique (A2) or rectilinear (A4 and A7) line scan analysis. Scale bars, 10 μm. (B), Signal intensity profiles of line scans of images in (A). (C), Representative images of axonal mitochondria with AVs in A2, A4 and A7 SNs from *park*^{25} mutant animals. Organelle co-localization was determined by oblique (A2 and A7) or rectilinear (A4) line scan analysis. Scale bars, 10 μm. (D), Signal intensity profiles of line scans of the images in (C). mito-GFP and RFP-Atg8 signals from both genotypes show distinct, non-overlapping distributions of mitochondria and AV signal throughout SNs. Angle brackets denote corresponding points in images (A, C) and line scan analysis for intensity profiles (B, D). AU, arbitrary units.

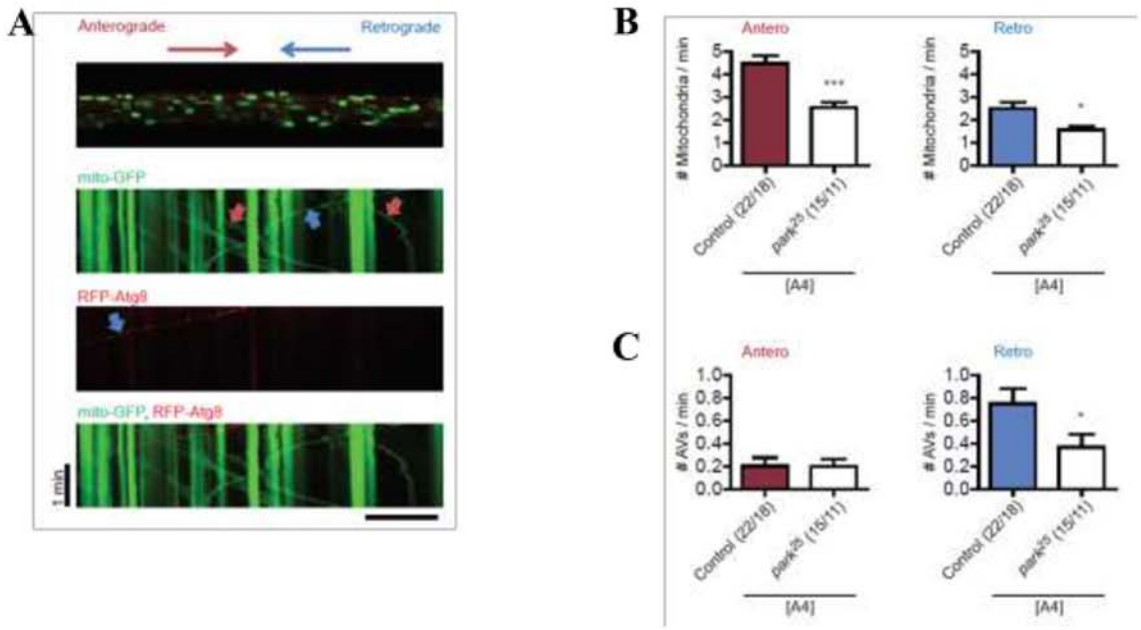

Figure 3.17 Parkin perturbation impairs retrograde transport of autophagic vacuoles. (A), Representative kymographs of mitochondrial and autophagosomal axonal transport from the A4 SNs axons of control animals. Red arrows indicate anterograde moving mitochondria, blue arrows indicate retrograde moving organelles. Scale bar, 10 μm. (B), Mitochondrial flux in different *parkin* genotypes. (C), Autophagosomal flux in different *parkin* genotypes. Reduced AV flux was observed only in the retrograde direction, while reduced mitochondrial flux was observed in both directions in $park^{25}$ mutant axons. (*n*/*n*) = number of axonal regions/number of animals. Error bars indicate mean ± SEM. Significance is determined by Student's *t*-test. $*p < 0.05$ and $***p < 0.001$.

3.9 Parkin-dependent Mitophagy Is Detectable in *Drosophila* Neurons *In Vitro*

It is notable that the most of the previous studies that have supported a role for Parkin in mitochondrial turnover and mitophagy were done *in vitro*, with either neuronal (Ashrafi et al., 2014) or non-neuronal (Narendra et al., 2008; Matsuda et al., 2010; Narendra et al., 2010; Lazarou et al., 2015) cells. As described above, however, mitochondria did not co-localized with autophagic vacuoles and there was no successful engulfment of mitochondria by autophagosomes in our *Drosophila* larval *in vivo* system. Thus, I next sought to examine whether mitophagy events can be detected in neurons *in vitro* in the same system that I used for the *in vivo* studies. Here, I used a *Drosophila* primary neuronal culture system to further investigate the role of Parkin in mitophagy process.

3.9.1 *park*^{25} neurons display inhibited mitochondrial engulfment into autophagosomes *in vitro*

To investigate the role of Parkin in mitophagy process *in vitro*, I grew *Drosophila* primary motor neurons in culture, using the mito-GFP larvae as the source of cells (Bai et al., 2009; Pathak et al., 2010). Cells were plated into tissue culture dishes, and incubated for 96 hours to allow neurons to extend their processes. Mitochondria and autophagic vacuoles which visualized by mito-GFP and RFP-atg8 respectively were monitored in motor cell bodies and projected axons to analyze the mitophagy process *in vitro*. Surprisingly, unlike the *in vivo* data, I observed numerous autophagic vacuoles that co-localized with mitochondria *in vitro*. Not only did control neurons show this evidence for mitophagy *in vitro*, but the frequency of autophagosome-mitochondrial co-localization was substantially reduced in neurons from *park*^{25} mutant larvae: frequencies were reduced to 33% of control levels in the cell bodies and 27% in the axons (Figure 3.18, A and B). Interestingly, however, number of the autophagic vacuoles of all kinds per cell in neurons cultured from *park*^{25} mutants was not reduced relative to controls in either the cell bodies or axonal regions (Figure 3.18, C). These results suggest that *in vitro* Parkin

plays an essential role in mitochondrial engulfment by autophagosomes, and also indicate that Parkin does not control the general process of autophagy.

3.9.2 *park*^{25} neurons display elongated axonal mitochondria *in vitro*

Unlike *in vivo*, another distinct feature of mitochondria from *in vitro* neurons was that I could observe more elongated axonal mitochondria in *park*^{25} mutant cells (Figure 3.19, A), which is predicted by current models of the role of Parkin in mitochondrial morphology (Deng et al., 2008). The mean length of axonal mitochondria was 2.48 ± 0.12 μm in control neurons, while mean length of axonal mitochondria was 4.10 ± 0.46 μm in *park*^{25} cells.

In the neuronal (Ashrafi et al., 2014) as well as non-neuronal (Matsuda et al., 2010; Narendra et al., 2010) environments, mitochondria that undergo mitophagy mostly show an isolated status and fragmented morphology. As expected, the mitochondria engulfed by autophagic vacuoles that I observed from cultured neurons were smaller than others, and fragmented (Figure 3.18, A). Thus, I further asked whether the size of mitochondria, rather than Parkin expressions is critical for the mitophagy event as visualized by autophagosome-mitochondria co-localization. To remodel mitochondria independently of Parkin perturbation, neurons were treated with 5 μM of Antimycin A (Ant A), an inhibitor of respiratory complex III that depolarizes neuronal mitochondria (Slater, 1973; Cai et al., 2012). Applying 5 μM of Ant A for 20 minutes caused a significant decrease in mitochondrial length in *park*^{25} cells (Figure 3.19, A), but they still contained a comparable number of autophagic vacuoles in both cell bodies and axons (Figure 3.18, C). However, mitochondrial engulfment via autophagosomes was still inhibited in *park*^{25} mutant neurons: the frequencies of autophagic vacuoles with fragmented mitochondria from *park*^{25} mutants were reduced to 28% of control levels in cell bodies and 49% in axons (Figure 3.18, A and B).

To further understand whether autophagic induction by itself can modulate autophagosome-mitochondria co-localization regardless of Parkin, I also tested the role of Parkin in mitophagy under conditions of experimental autophagic induction. To

promote mitophagy, cells were treated with 100 μM of H_2O_2, a reactive oxygen species that induces autophagic process through oxidative stress (Court and Coleman, 2012). Again, mitochondrial size was significantly decreased in both control and *park*^{25} cells by H_2O_2 treatment for 1 hour (Figure 3.19, A). However, even under conditions of oxidative stress I observed inhibition of mitochondrial engulfment in *park*^{25} mutant cells: in H_2O_2-treated cells the frequency of autophagic vacuoles co-localizing with mitochondria was reduced to 18% of control levels in cell bodies and to 39% in axons (Figure 3.18, A and B). Collectively, these data suggest that that Parkin regulates mitophagy *in vitro* independently of the modulation of mitochondrial size. Furthermore, since both Ant A and H_2O_2 treatments cause fragmentation of mitochondria (Figure 3.19, B) but no increase in autophagic vacuoles (Figure 3.18, C), I also can conclude that Parkin is dispensable for the remodeling of damaged mitochondria and for the regulation of general autophagy *in vitro*.

3.9.3 *park*^{25} neurons display diminished inner membrane potential of axonal mitochondria *in vitro*

Since I saw elongated axonal mitochondria and inhibited autophagosomal engulfment in *park*^{25} neurons *in vitro*, I further asked whether those axonal mitochondria in *park*^{25} cells preserve the normal inner membrane potential. Mitochondrial $\Delta\Psi_m$ was determined by using the intensity ratio of TMRM staining between mitochondria and cytosol within the projected axons. Intriguingly, *park*^{25} cells displayed diminished $\Delta\Psi_m$ in neuronal axons (Figure 3.20, A and B). Consistent with previous analysis, axonal mitochondria were elongated in *park*^{25} cells (Figure 3. 20, C). For this reason, I additionally regressed mitochondrial $\Delta\Psi_m$ against their lengths to determine whether neurons *in vitro* display a key predicted consequence of Parkin-mediated mitochondrial quality control: the accumulation of longer, less polarized organelles in the absence of Parkin. I found that indeed, *park*^{25} motor axons contained a small outlying population of longer mitochondria, and those mitochondria generally displayed diminished $\Delta\Psi_m$ (Figure 3.20, D and E): the length distribution by a two-sample Kolmogorov-Smirnov test shows a significant

difference between the two groups (D = 0.2107 > *critical* D = 0.1274 with a corresponding $p < 0.001$). Thus, as previously reported, I also find a significant *in vitro* role for Parkin in regulating axonal mitochondrial morphology and metabolic state; however, I do not observe these phenomena in the same neurons studied *in vivo*.

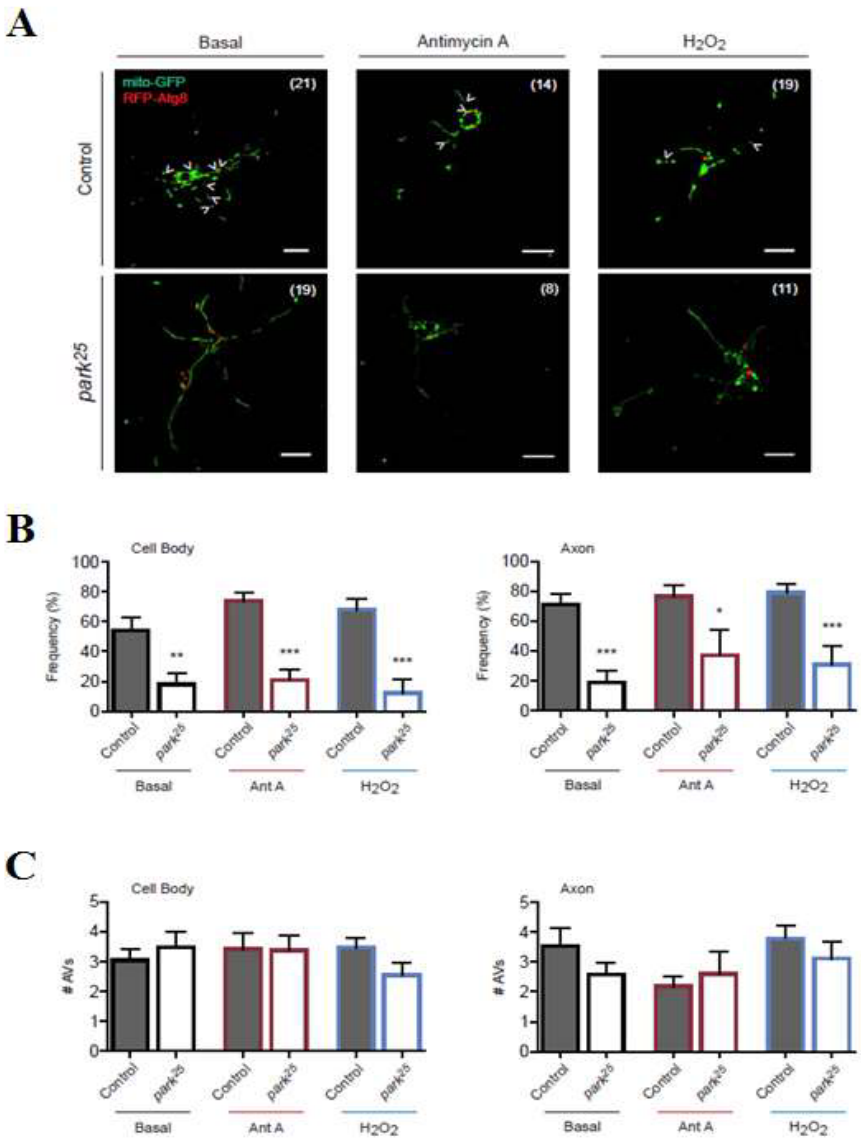

Figure 3.18 Parkin is essential for mitochondrial engulfment by autophagosomes *in vitro*. (A), Images of *in vitro* primary motor neurons expressing mito-GFP and RFP-Atg8 after 96 hours in culture. For stress conditions, cells are exposed to Antimycin A (Ant A; 5 μM, 20 minutes) or H_2O_2 (100 μM, 1 hour) before imaging. White arrowheads denote the co-localization of mitochondria with AVs. Scale bars, 10 μm. (*n*) = number of cells. (B), Frequency of autophagosomes that contain mitochondria under each condition. Mitochondrial engulfment into AVs is inhibited in *park*^{25} mutant neurons. (C), Number of AVs per cell under each condition within cell bodies or axons. Error bars indicate mean ± SEM. Significance is determined by Student's *t*-test. **p* < 0.05, ***p* < 0.01 and ****p* < 0.001.

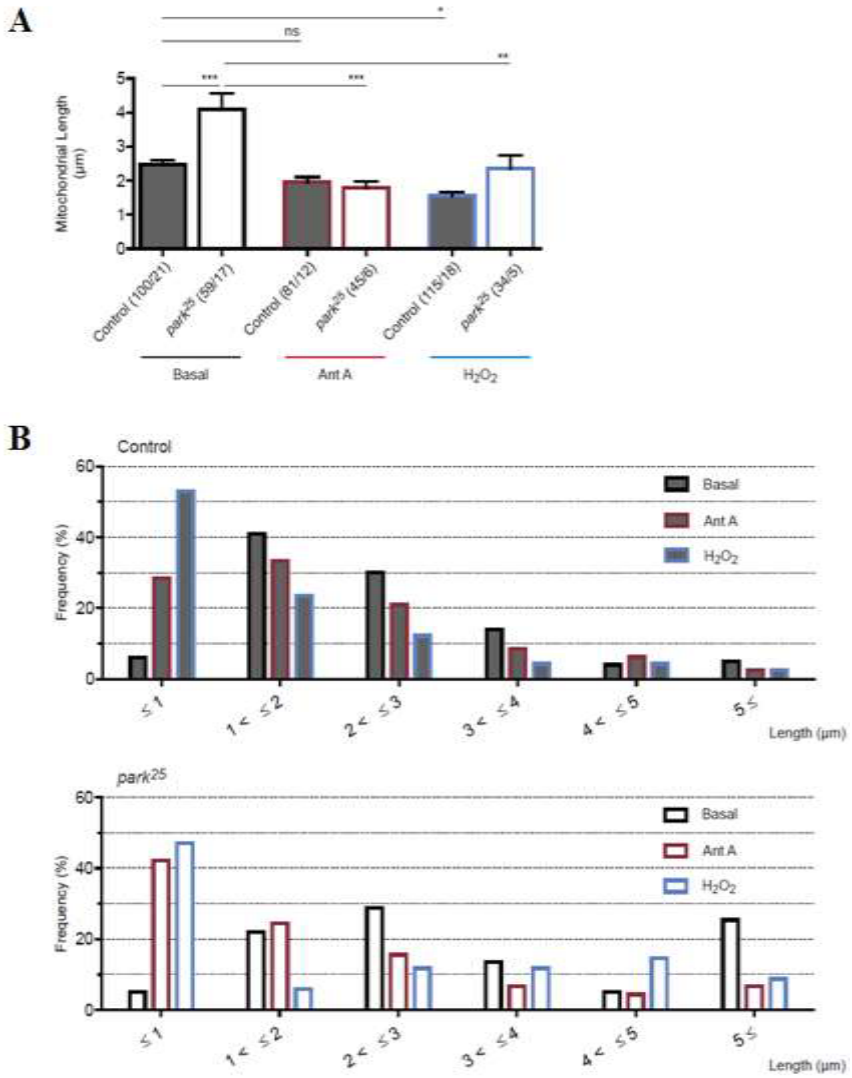

Figure 3.19 Elongated mitochondria are produced in *park*^{25} primary neurons *in vitro*. (A), Mean length of axonal mitochondria in different *parkin* genotypes in exposed conditions respectively. *park*^{25} mutant neurons show elongated axonal mitochondria. Axonal mitochondrial elongation in *park*^{25} neurons is inhibited by either treatment (Ant A or H_2O_2). (*n*/*n*) = number of mitochondria/number of cells. Error bars indicate mean ± SEM. Significance is determined by one-way ANOVA with Bonferroni correction (*p < 0.05, **p < 0.01 and ***p < 0.001). (B), Length distribution of axonal mitochondria in different *parkin* genotypes. Ant A or H_2O_2 treatment caused axonal mitochondrial fragmentation in both control and *park*^{25} mutant neurons *in vitro*. Data were assessed by a two-sample Kolmogorov-Smirnov test (mitochondrial fragmentation caused by Ant A or H_2O_2 treatments was significantly different from basal for both control and *park*^{25} animals: $D = 0.22 > critical\ D = 0.20$ for Ant A and $D = 0.47 > critical\ D = 0.19$ for H_2O_2 in control, $D = 0.40 > critical\ D = 0.27$ for Ant A and $D = 0.42 > critical\ D = 0.29$ for H_2O_2 in park^{25}).

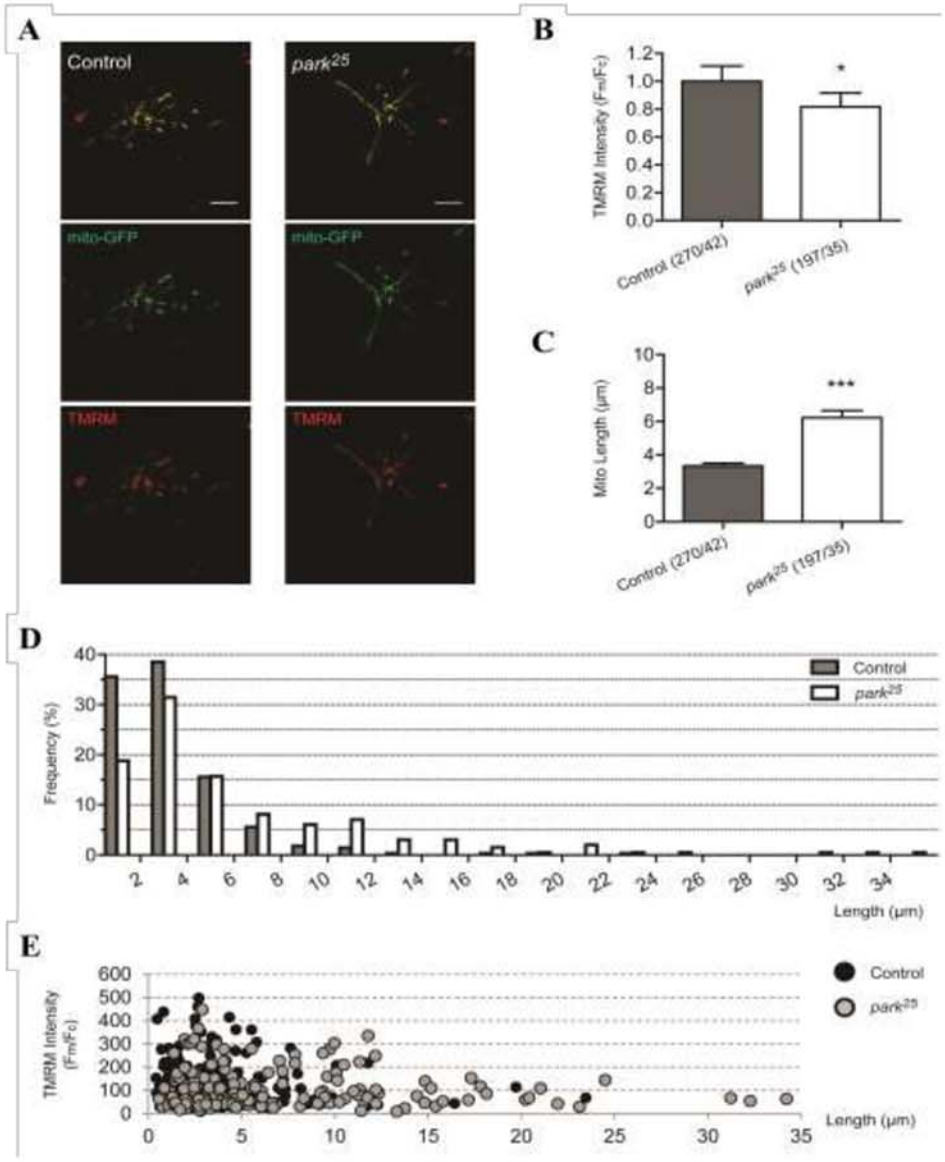

Figure 3. 20 Parkin perturbation produced elongated mitochondria with diminished $\Delta\Psi_m$ *in vitro*. (A), Representative images of motor neurons stained with TMRM *in vitro* after 96 hours in culture. Scale bars, 10 μm. (B), Mean F_m/F_c intensity ratio of TMRM from cultured neurons of different *parkin* genotypes. (C), Mean length of axonal mitochondria *in vitro*. (D), Length distribution of axonal mitochondria *in vitro*. (E), Relationship between mitochondrial $\Delta\Psi_m$ and length in axons *in vitro*. Correlation coefficients: control ($R^2 = 0.0049 \leq 0.65$) and *park*^{25} ($R^2 = 0.0004 \leq 0.65$). *park*^{25} mutant neurons *in vitro* showed decreased $\Delta\Psi_m$ and elongated axonal mitochondria. (*n*/*n*) = number of mitochondria/number of cells. Error bars indicate mean ± SEM. Significance is determined by Student's *t*-test (B and C) or by two-sample Kolmogorov-Smirnov test (D), K-S statistics show significant difference). $*p < 0.05$ and $***p < 0.001$.

3.10 Generation of *park*^{1} Mutant Fly Expressing *mito-GFP* in Motor Neurons

As described above, *park*^{25} mutant animals displayed dramatic defects of mitochondrial dynamics and morphology in larval motor neurons *in vivo*, and that were: 1) attenuated mitochondrial fluxes in axons (Figure 3.2); 2) reduced mitochondrial density in axons (Figure 3.4); 3) morphological defects of mitochondria in cell bodies (Figure 3.13). Since those defects were generally restored by *UAS-Parkin* expression; one exception was reduced mitochondrial axonal density from adult fly wing (Figure 3.6), I tried to further confirm the *in vivo* role of Parkin in mitochondrial dynamics and morphology by using another null mutant, *park*^{1} allele (J.C. Clemens, Purdue University). Genomic structure of *Drosophila parkin* contains 7 exons, and *park*^{1} null allele was generated by P-element insertion within the fifth exon (Cha et al., 2005) (Figure 3.21). I built *park*^{1} mutant animals that contains *D42>mito-GFP* transgene by genetic recombination because of the *park*^{1} locus in fly chromosomes; both *D42-Gal4>UAS-mitoGFP* (Table 2.1, #1) and *park*^{1} (Table 2.1, #19) localize within chromosome (III).

3.10.1 Genetic recombination

To build *park*^{1} mutant animals that contain *D42>mito-GFP* transgene, first I collected virgin females of *D42-Gal4>UAS-mitoGFP* (III) and crossed them with males of *park*^{1}/TM6B (III) to get the heterozygous animals of *D42-Gal4>UAS-mitoGFP*/*park*^{1} (III). Then virgin females from the generated heterozygous animals of *D42-Gal4>UAS-mitoGFP*/*park*^{1} (III) was crossed again with males that harbor double balancer of *TM2*/*TM6B* (III) (Table 2.1, #20). This crossbreeding basically produced four genotypes of progenies: *D42-Gal4>UAS-mitoGFP*/*TM2* (III), *D42-Gal4>UAS-mitoGFP*/*TM6B* (III), *park*^{1}/*TM2* (III) or *park*^{1}/*TM6B* (III), however, I could expect to get heterozygous of *park*^{1} allele animals that contain *D42-Gal4>UAS-mitoGFP* by chromosomal recombination in this step. By this reason, I collected adult males that eclosed from the first filial generation: the flies were selected by tubby with red eye, and cross them with females of *park*^{1}/TM6B (III) individually to confirm the genotype of male flies at the

second filial generation. 247 adult males were collected by two sets of crossbreeding (108 from set 1 and 139 from set 2) from the first filial generation, and 5 among 247 were confirmed by thoracic indentation penetrance (Poole et al., 2008) at the third filial generation (Figure 3.22). To finally obtain the heterozygous of *park*^{1}*, D42-Gal4>UAS-mitoGFP*/TM6B (III) animals, flies expressing tubby with red eye phenotypes that already confirmed by thoracic indentation were isolated and maintained.

3.10.2 *park*^{1}, *D42>mito-GFP* animals display loss of Parkin expression

The generated *park*^{1}*, D42-Gal4>UAS-mitoGFP*/TM6B (III) transgenic animals were first confirmed and isolated by the *Parkin* null fly phenotype of thoracic indentation. However, the observed phenotypic penetrance of *park*^{1} homozygous flies was ~ 30%. Thus, I checked the protein expression by western blot analysis to confirm further the null nature of *park*^{1} alleles. Here, adult head extracts from the male flies were prepared for the lysates, and anti-Parkin antiboby (278N 213.03) and mouse anti-α-tubulin were used for the Parkin and loading control detection respectively. Since the molecular weights of Parkin (~52 kDa) and α-tubulin (~50 kDa) were too close to identify on membrane separation, I washed the membrane with stripping buffer which contains β-mercaptoethanol to remove anti-Parkin antibody after the Parkin detection. Then, the membrane was used for α-tubulin detection. As expected, Parkin was not detected in *park*^{1} transgenic animals (Figure 3.23). Therefore, this result confirms that *park*^{1} flies expressing mito-GFP in motor neurons that I generated by genetic recombination are null alleles, and suggests that *park*^{1}*, D42-Gal4>UAS-mitoGFP* flies will display the loss of Parkin function for further understanding the *in vivo* role of Parkin in mitochondrial dynamics and morphology.

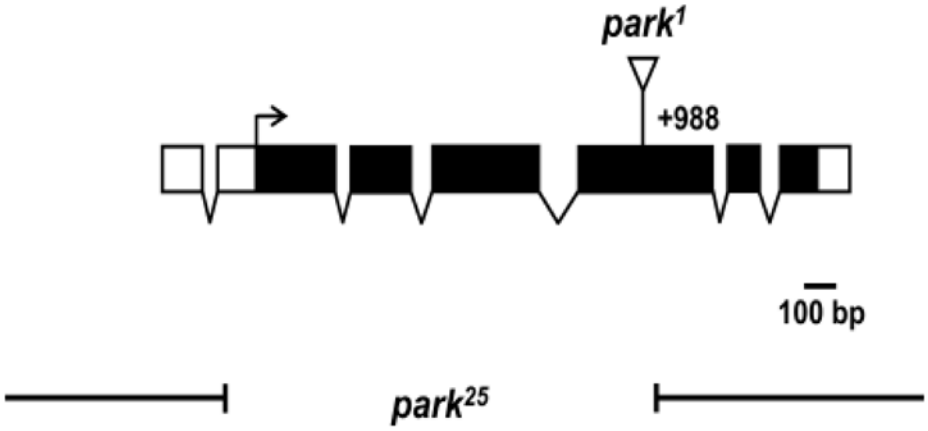

Figure 3.21 Genomic structures of *Drosophila parkin* and its mutants. *Drosophila parkin* contains 7 exons that form a 1.449 bp transcript encoding a protein of 482 amino acids from middle of the second exon to middle of the seventh exon. Exons are designated as boxes and Parkin protein-coding sequences are highlighted in black. The breakpoint describes the $park^{25}$ deletion allele. The P-element insertion site of $park^{1}$ in the fifth exon is located at +988 of the *parkin* open reading frame and indicated by arrowhead.

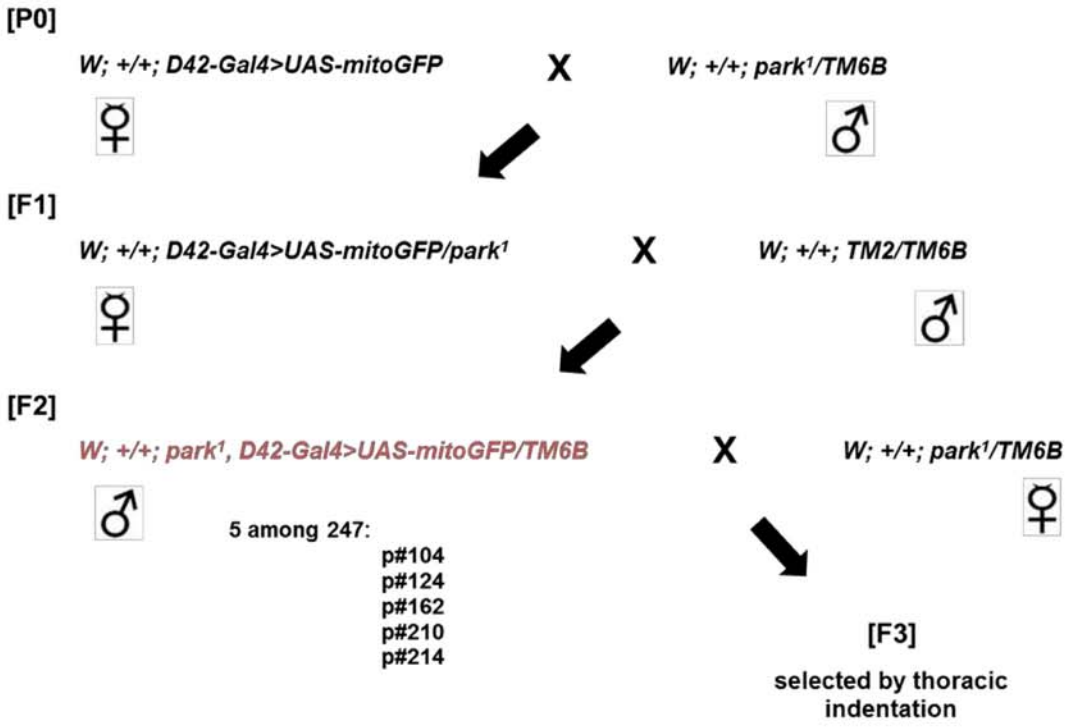

Figure 3.22 Fly crosses for building *park1*, *D42>mito-GFP* transgene. *park*^{1} flies that contain *D42-Gal4>UAS-mitoGFP* transgene are generated at the F2 generation, and confirmed by the phenotype of thoracic indentation penetrance at F3 generation.

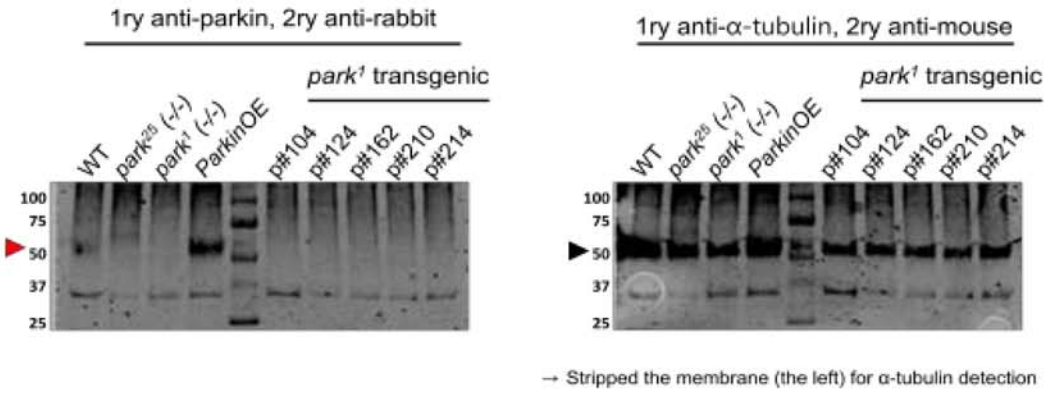

Figure 3.23 *park*^{1}, *D42-Gal4>UAS-mitoGFP* transgenic flies express the absence of Parkin. *park*^{1}, *D42-Gal4>UAS-mitoGFP* transgenic flies that generated by chromosomal recombination are confirmed by anti-Parkin. Western blot analysis shows the absence of Parkin in *park*^{1} transgenic mutants. After Parkin detection, membrane is washed by stripping buffer that contains β-mercaptoethanol to detect α-tubulin as the loading control. The red arrowhead indicates the size of Parkin (~52 kDa), and the black arrowhead indicates the size of α-tubulin (~50 kDa). 60 μg of proteins from adult heads are loaded. Size units are kDa.

CHAPTER 4. DISCUSSION

Mitochondria play critical roles in cellular function, homeostasis and survival. Since mitochondria display a dynamic life cycle, their maintenance and long-term survival highly require adequate organelle QC. Because of their increased energy demand, post-mitotic neurons are exemplary cell types that are more susceptible to defective mitochondrial QC. Therefore, mitochondrial quality should be well controlled to avoid neuronal defects as well as neuronal death. Many factors are likely to act to help maintain mitochondrial QC in neurons. First, axonal transport of mitochondria along the cytoskeleton is important for organelle distribution and turnover. This probably supports the traffic of dysfunctional mitochondria to a site of removal in neurons. Second, mitochondria can undergo a constant cycle of shape changes by fission-fusion that helps to accommodate the damaged components of the organelle. Thus, dysfunctional mitochondria can be segregated and isolated by preventing fusion, or the damaged material in the organelle can be diluted and exchanged by allowing fusion. Third, the dysfunctional mitochondria can be engulfed into autophagosomes to trigger their removal process through lysosomal digestion. In neurons, this mitophagy process may be regulated in a selective and/or non-selective manner. Because neurons are highly compartmentalized cells, with structurally and functionally distinct somatodendritic and axonal compartments, it is important to understand not just whether and how dysfunctional mitochondria are turned over, but also where this occurs.

In cells *in vitro*, the PINK1 and Parkin pathway has been proposed both to target dysfunctional mitochondria for turnover, and, in a related fashion, to regulate mitochondrial transport and fission-fusion dynamics. In this context, understanding the *in vivo* role of Parkin is important for better evaluating both mitochondrial dynamics

and their life cycle. In this study, I report important findings on Parkin-dependent mitochondrial QC from *in vivo* and *in vitro Drosophila* larval nervous systems: 1) Parkin deficient animals display a dramatically reduced amount of axonal mitochondria, while preserving normal axonal mitochondrial transport, morphology and $\Delta\Psi_m$; 2) the mitochondrial *in vivo* fission-fusion balance is compartmentally regulated in the cell body in a Parkin-dependent manner; 3) unlike *in vivo*, the mitophagy process is prominent in cultured neurons, and requires Parkin.

4.1 Role of Parkin in Mitochondrial Axonal Transport and Quality Control

Studies of mitochondrial transport in neurons have been critical for a better understanding of how organelle turnover works in compartmentalized cells. In neurons, axonal transport of mitochondria has long been held to be intimately related to other organelle functions such as fission-fusion, metabolism and turnover (Miller and Sheetz, 2004; Baloh et al., 2007; Pathak et al., 2010; Arduino et al., 2012; Saxton and Hollenbeck, 2012). A model for Parkin involvement in axonal mitochondrial motility is that PINK1/Parkin specifically dissociates kinesin, the MT-based anterograde motor, from the organelle surface through degradation of its linker protein, Miro (Wang et al., 2011). This proposed model, however, is inadequate to explain why and how the disruption of mitochondrial movement occurs in both directions, not only in anterograde also in retrograde, by PINK1 and Parkin modulations. Since disruptions targeted to one direction of MT-based axonal transport often alter organelle movement in both directions (Pilling et al., 2006; Park et al., 2009; Russo et al., 2009), it is possible that the regulation of MT-based axonal transport is intricately coupled between the motors for the two directions of movement, kinesin and dynein. In any case, contrary to the proposed model of PINK1/Parkin dependent mitochondrial arrest, here I observed nearly unchanged mitochondrial motility behavior *in vivo* when the Parkin expression was perturbed (Figure 3.3). Instead, I found dramatically reduced mitochondrial flux (Figure 3.2), producing by altered organelle density, in mutant SNs. Indeed, the unexpected finding of reduced organelle density from

in vivo Parkin-deficient SNs (Figure 3.4) raises the idea that the reduced mitochondrial flux, the main defect in axonal transport that I found in mutant motor axons, is mostly caused by diminution in organelle quantity. This is the opposite of the result expected for Parkin deletion, if this pathway was driving clearance of senescent mitochondria from the axon. It is however consistent with our previous demonstration that manipulation of PINK1 also fails to effect mitochondrial arrest (Devireddy et al., 2015).

Since the PINK1/Parkin pathway is proposed to be required for targeting damaged mitochondria (Narendra et al., 2008; Jin et al., 2010; Matsuda et al., 2010; Narendra et al., 2010; Lazarou et al., 2015), for local mitophagy (Ashrafi et al., 2014), and with promoting organelle fission (Clark et al., 2006; Deng et al., 2008; Poole et al., 2010; Ziviani et al., 2010), the contrary result of axonal mitochondrial diminution further causes me to investigate the *in vivo* role of Parkin in neuronal mitochondrial turnover with considering organelle morphology. In neurons (Ashrafi et al., 2014) as well as non-neuronal (Matsuda et al., 2010; Narendra et al., 2010) environments, mitochondria that undergo mitophagy mostly show an isolated and fragmented morphology. In this context, I asked whether those remaining mitochondria in mutant axons harbor any of morphologically and/or physiologically disrupted organelle state. Surprisingly, quantitative morphological analyses demonstrated that mutant animals preserved a normal state of axonal mitochondria despite their lower amount (Figure 3.8 and 3.9). This was further validated by measuring mitochondrial $\Delta\Psi_m$: neither elongated organelles nor diminished $\Delta\Psi_m$ were observed in the Parkin-deficient axons (Figure 3.10, B and C) as well as in their NMJs (Figure 3.11). Instead, I found a dramatic alteration of organelle morphology in mutant cell bodies (Figure 3.13) which consequently makes me to consider the compartmentalized *in vivo* role of Parkin in neurons. Thus, the collected results from *in vivo* larval motor neurons suggest that Parkin plays an important role in preserving the normal amount of mitochondria in axons and it seems to be critically associated with the modulation of organelle fission-fusion balance in cell bodies rather than the underlying adjustment of organelle arrest in axons.

4.2 Compartmentalized Role of Parkin in Mature Neurons

The morphological defects of mitochondria that I found specifically in *park*^{25} cell bodies raise the possibility of compartmentalized organelle QC regulated by Parkin in mature neurons. What could be restricting Parkin-dependent mitochondrial QC to cell bodies *in vivo*? Since mitochondria dynamically interact with other organelles, such as endoplasmic reticulum (ER), it is possible that the location of the ER network may contribute to the compartmentalized Parkin-dependent mitochondrial QC. In fact, ER tubules form membrane contact sites with a number of other organelles (Rowland and Voeltz, 2012; Rowland et al., 2014) and such contacts regulate diverse neuronal functions, including motor protein dependent organelle transport and neurite outgrowth (Raiborg et al., 2015). More important, it has been recently proposed that ER tubules also play a regulatory role in mitochondrial division by contacting mitochondria and causing their constriction prior to the recruitment of the mitochondrial fission protein Drp1 (Friedman et al., 2011). Because the neuronal ER network is mostly located adjacent to the outer layer of the nuclear envelope (Berridge, 1998; Verkhratsky and Petersen, 1998), it is plausible that mitochondrial morphology is particularly disrupted in cell body by Parkin perturbation. If the somatic compartment is the main location of neuronal mitochondrial turnover (Safiulina and Kaasik, 2013), the entry and exit of organelles between cell bodies and axons are critically important for regulating the neuronal mitochondrial life cycle. In this context, I propose another possibility: that mature neurons possess a physical barrier in-between the cell body and axon for restricting axonal entry of mitochondria to those of appropriate size, morphology and metabolic status. Thus, the disrupted fission-fusion balance caused by Parkin perturbation which produces inter-connected mitochondria in cell body may physically disrupt a “launching process” of dysfunctional organelles into axon. This proposal is consistent with recent evidence that the pre-axonal exclusion zone in the hillock provides a cytoplasmic boundary for the entry of vesicles into axonal domain (Farias et al., 2015).

The hypothesis that new mitochondria are generated in the cell body to meet axonal requirements underlies the importance of organelle axonal transport, especially

anterograde movement. Indeed, it is notable that the same reduced-axonal-density phenotype that I observed has previously been reported in motor axons of *Drosophila* SNs with disrupted motor protein expression (Pilling et al., 2006). In that study, it was remarkable that only kinesin heavy chain mutants displayed reduced mitochondrial density in SNs, while mutations in *dynein* retained the normal compliment of axonal mitochondria. Furthermore, our previous report demonstrated that Parkin selectively restored the abnormal mitochondria of *PINK1* mutants only in cell bodies, but not in axons (Devireddy et al., 2015). Taken together, these findings suggest a compartmentalized *in vivo* role of PINK1/Parkin in neuronal mitochondrial turnover and provide further evidence that the mitochondrial supply from the cell body is critically important for preserving organelle numbers and distribution in axons.

4.3 Mitochondrial Quality Control *In Vivo* and *In Vitro*

I did observe the morphological remodeling of mitochondria under stress conditions both *in vivo* and *in vitro*: 6 hours of starvation *in vivo* (Figure 3.15), as well as Ant A and H_2O_2 treatment *in vitro* (Figure 3.18) both produced fragmented mitochondria even in the absence of Parkin. It is likely that mitochondrial fission can be regulated independently of Parkin and/or up-regulated by stress conditions that overwhelm normal physiological fusion. However, I was surprised to observe several dramatic distinctions in the mitochondrial life cycle between motor neurons *in vivo* and *in vitro*. First, I barely observed the AVs that co-localized with mitochondria throughout *in vivo* motor neurons, whereas Parkin-dependent mitophagy was obvious in the same neurons *in vitro*. Second, the axonal mitochondria which were preserved in the normal state *in vivo* were elongated and displayed diminished $\Delta\Psi m$ *in vitro* in Parkin perturbation. Thus, unlike *in vivo*, my observations from *in vitro* neuronal culture system reasonably support the current proposed role of Parkin on mitochondrial QC, targeting senescent mitochondria and promoting mitochondrial fission.

What could explain these differences? One possibility is that the mature neurons possess a thorough mitochondrial network constructed via an established physical filter in-between the cell body and axon, are which remains less-developed *in vitro*. In support of this idea, I noted that the most axonal mitochondria *in vivo* were morphologically nearly uniform and ~2 times shorter than axonal mitochondria in cultured neurons (Figure 3.8 and 3.19). In addition, axonal mitochondria *in vitro* often extended continuously from the cell body into the axon (Figure 3.18 A), a feature that is rarely if ever seen *in vivo*, suggesting that the filter between the cell body and axon is absent or more permissive in isolated cultured neurons. In this case, mitochondria that enter into axon would be more restricted and scrutinized *in vivo* than *in vitro*. Indeed, possible idea is in accord with the down-regulated mitophagy events that I observed in the *in vivo* larval nervous system. Perhaps the role of Parkin in mitochondrial fission-fusion balance is compartmentalized in the mature cell body and this may reduce the need for local mitophagy process in axons *in vivo*. In addition, I cannot exclude another possibility: that the mature neurons *in vivo* are functionally associated with surrounding cells and tissues that contribute to mitochondrial turnover. Recent evidence from mouse optic nerve head *in vivo* (Davis et al., 2014) shows the extrusion and transcellular degradation of axonal mitochondria, “transmitophagy”, a process that could provide a different avenue for mitochondrial turnover in the periphery, and could contribute to the lack of axonal mitophagy that I observed *in vivo*.

In this study, I report the distinct and compartmentalized *in vivo* role of Parkin in mitochondrial QC. By comparing *Drosophila* motor neurons *in vivo* and *in vitro*, I find dramatic differences: despite their reduced amount, axonal mitochondria retain their normal state in Parkin-deficient mature neurons, whereas, in cultured axons the organelle morphology and inner membrane potential are critically affected by Parkin deletion. Instead, Parkin deficient animals display disrupted mitochondrial morphology specifically in the motor cell bodies. In addition, mitophagy is rarely observed in the mature *Drosophila* motor neurons, but it is regulated in a Parkin-dependent manner in the

in vitro cultured neurons. Unlike *in vitro* conditions, therefore, the *in vivo* role of Parkin does not appear obviously related to mitophagy, and is restricted to the cell body where it seems to modulate mitochondrial fission-fusion balance. Thus, these findings re-emphasize the intricate interdependence of mitochondrial dynamics and axonal transport, and further suggest the importance of mitochondrial network between cell body and axon for preserving organelle QC.

LIST OF REFERENCES

LIST OF REFERENCES

Amiri, M., and P.J. Hollenbeck. 2008. Mitochondrial biogenesis in the axons of vertebrate peripheral neurons. *Developmental neurobiology*. 68:1348-1361.

Arduino, D.M., A.R. Esteves, L. Cortes, D.F. Silva, B. Patel, M. Grazina, R.H. Swerdlow, C.R. Oliveira, and S.M. Cardoso. 2012. Mitochondrial metabolism in Parkinson's disease impairs quality control autophagy by hampering microtubule-dependent traffic. *Human molecular genetics*. 21:4680-4702.

Arnoult, D., N. Rismanchi, A. Grodet, R.G. Roberts, D.P. Seeburg, J. Estaquier, M. Sheng, and C. Blackstone. 2005. Bax/Bak-dependent release of DDP/TIMM8a promotes Drp1-mediated mitochondrial fission and mitoptosis during programmed cell death. *Current biology : CB*. 15:2112-2118.

Ashrafi, G., J.S. Schlehe, M.J. LaVoie, and T.L. Schwarz. 2014. Mitophagy of damaged mitochondria occurs locally in distal neuronal axons and requires PINK1 and Parkin. *The Journal of cell biology*. 206:655-670.

Bai, J., K.J. Sepp, and N. Perrimon. 2009. Culture of Drosophila primary cells dissociated from gastrula embryos and their use in RNAi screening. *Nature protocols*. 4:1502-1512.

Baloh, R.H., R.E. Schmidt, A. Pestronk, and J. Milbrandt. 2007. Altered axonal mitochondrial transport in the pathogenesis of Charcot-Marie-Tooth disease from mitofusin 2 mutations. *The Journal of neuroscience : the official journal of the Society for Neuroscience*. 27:422-430.

Berridge, M.J. 1998. Neuronal calcium signaling. *Neuron*. 21:13-26.

Cai, Q., H.M. Zakaria, A. Simone, and Z.H. Sheng. 2012. Spatial parkin translocation and degradation of damaged mitochondria via mitophagy in live cortical neurons. *Current biology : CB*. 22:545-552.

Caldwell, C.C., J. Yao, and R.D. Brinton. 2015. Targeting the prodromal stage of Alzheimer's disease: bioenergetic and mitochondrial opportunities. *Neurotherapeutics : the journal of the American Society for Experimental NeuroTherapeutics*. 12:66-80.

Carreira, V.P., I.M. Soto, J. Mensch, and J.J. Fanara. 2011. Genetic basis of wing morphogenesis in Drosophila: sexual dimorphism and non-allometric effects of shape variation. *BMC developmental biology*. 11:32.

Caviston, J.P., and E.L. Holzbaur. 2009. Huntingtin as an essential integrator of intracellular vesicular trafficking. *Trends in cell biology*. 19:147-155.

Cha, G.H., S. Kim, J. Park, E. Lee, M. Kim, S.B. Lee, J.M. Kim, J. Chung, and K.S. Cho. 2005. Parkin negatively regulates JNK pathway in the dopaminergic neurons of Drosophila. *Proceedings of the National Academy of Sciences of the United States of America*. 102:10345-10350.

Chada, S.R., and P.J. Hollenbeck. 2004. Nerve growth factor signaling regulates motility and docking of axonal mitochondria. *Current biology : CB*. 14:1272-1276.

Chan, D.C. 2006. Mitochondrial fusion and fission in mammals. *Annual review of cell and developmental biology*. 22:79-99.

Chang, D.T., G.L. Rintoul, S. Pandipati, and I.J. Reynolds. 2006. Mutant huntingtin aggregates impair mitochondrial movement and trafficking in cortical neurons. *Neurobiol Dis*. 22:388-400.

Chen, H., and D.C. Chan. 2009. Mitochondrial dynamics--fusion, fission, movement, and mitophagy--in neurodegenerative diseases. *Human molecular genetics*. 18:R169-176.

Chen, Y., and G.W. Dorn, 2nd. 2013. PINK1-phosphorylated mitofusin 2 is a Parkin receptor for culling damaged mitochondria. *Science*. 340:471-475.

Cheng, X.T., B. Zhou, M.Y. Lin, Q. Cai, and Z.H. Sheng. 2015. Axonal autophagosomes recruit dynein for retrograde transport through fusion with late endosomes. *The Journal of cell biology*. 209:377-386.

Clark, I.E., M.W. Dodson, C. Jiang, J.H. Cao, J.R. Huh, J.H. Seol, S.J. Yoo, B.A. Hay, and M. Guo. 2006. Drosophila pink1 is required for mitochondrial function and interacts genetically with parkin. *Nature*. 441:1162-1166.

Colin, E., D. Zala, G. Liot, H. Rangone, M. Borrell-Pages, X.J. Li, F. Saudou, and S. Humbert. 2008. Huntingtin phosphorylation acts as a molecular switch for anterograde/retrograde transport in neurons. *The EMBO journal*. 27:2124-2134.

Court, F.A., and M.P. Coleman. 2012. Mitochondria as a central sensor for axonal degenerative stimuli. *Trends in neurosciences*. 35:364-372.

Davis, A.F., and D.A. Clayton. 1996. In situ localization of mitochondrial DNA replication in intact mammalian cells. *The Journal of cell biology*. 135:883-893.

Davis, C.H., K.Y. Kim, E.A. Bushong, E.A. Mills, D. Boassa, T. Shih, M. Kinebuchi, S. Phan, Y. Zhou, N.A. Bihlmeyer, J.V. Nguyen, Y. Jin, M.H. Ellisman, and N. Marsh-Armstrong. 2014. Transcellular degradation of axonal mitochondria. *Proceedings of the National Academy of Sciences of the United States of America*. 111:9633-9638.

De Vos, K.J., A.L. Chapman, M.E. Tennant, C. Manser, E.L. Tudor, K.F. Lau, J. Brownlees, S. Ackerley, P.J. Shaw, D.M. McLoughlin, C.E. Shaw, P.N. Leigh, C.C. Miller, and A.J. Grierson. 2007. Familial amyotrophic lateral sclerosis-linked SOD1 mutants perturb fast axonal transport to reduce axonal mitochondria content. *Human molecular genetics*. 16:2720-2728.

Deng, H., M.W. Dodson, H. Huang, and M. Guo. 2008. The Parkinson's disease genes pink1 and parkin promote mitochondrial fission and/or inhibit fusion in Drosophila. *Proceedings of the National Academy of Sciences of the United States of America*. 105:14503-14508.

Devireddy, S., A. Liu, T. Lampe, and P.J. Hollenbeck. 2015. The Organization of Mitochondrial Quality Control and Life Cycle in the Nervous System In Vivo in the Absence of PINK1. *The Journal of neuroscience : the official journal of the Society for Neuroscience*. 35:9391-9401.

Devireddy, S., H. Sung, P.C. Liao, E. Garland-Kuntz, and P.J. Hollenbeck. 2014. Analysis of mitochondrial traffic in Drosophila. *Methods in enzymology*. 547:131-150.

Dodson, M.W., and M. Guo. 2007. Pink1, Parkin, DJ-1 and mitochondrial dysfunction in Parkinson's disease. *Current opinion in neurobiology*. 17:331-337.

Fang, Y., L. Soares, and N.M. Bonini. 2013. Design and implementation of in vivo imaging of neural injury responses in the adult Drosophila wing. *Nature protocols*. 8:810-819.

Fang, Y., L. Soares, X. Teng, M. Geary, and N.M. Bonini. 2012. A novel Drosophila model of nerve injury reveals an essential role of Nmnat in maintaining axonal integrity. *Current biology : CB*. 22:590-595.

Farias, G.G., C.M. Guardia, D.J. Britt, X. Guo, and J.S. Bonifacino. 2015. Sorting of Dendritic and Axonal Vesicles at the Pre-axonal Exclusion Zone. *Cell reports*. 13:1221-1232.

Fiskum, G., A.N. Murphy, and M.F. Beal. 1999. Mitochondria in neurodegeneration: acute ischemia and chronic neurodegenerative diseases. *Journal of cerebral blood flow and metabolism : official journal of the International Society of Cerebral Blood Flow and Metabolism*. 19:351-369.

Frezza, C., S. Cipolat, O. Martins de Brito, M. Micaroni, G.V. Beznoussenko, T. Rudka, D. Bartoli, R.S. Polishuck, N.N. Danial, B. De Strooper, and L. Scorrano. 2006. OPA1 controls apoptotic cristae remodeling independently from mitochondrial fusion. *Cell*. 126:177-189.

Friedman, J.R., L.L. Lackner, M. West, J.R. DiBenedetto, J. Nunnari, and G.K. Voeltz. 2011. ER tubules mark sites of mitochondrial division. *Science*. 334:358-362.

Fu, M.M., J.J. Nirschl, and E.L. Holzbaur. 2014. LC3 binding to the scaffolding protein JIP1 regulates processive dynein-driven transport of autophagosomes. *Developmental cell*. 29:577-590.

Gautier, C.A., T. Kitada, and J. Shen. 2008. Loss of PINK1 causes mitochondrial functional defects and increased sensitivity to oxidative stress. *Proceedings of the National Academy of Sciences of the United States of America*. 105:11364-11369.

Geisler, S., K.M. Holmstrom, D. Skujat, F.C. Fiesel, O.C. Rothfuss, P.J. Kahle, and W. Springer. 2010. PINK1/Parkin-mediated mitophagy is dependent on VDAC1 and p62/SQSTM1. *Nature cell biology*. 12:119-131.

Gelino, S., and M. Hansen. 2012. Autophagy - An Emerging Anti-Aging Mechanism. *Journal of clinical & experimental pathology*. Suppl 4.

Ghosh, D., J.L. Walton, P.D. Roepe, and A.P. Sinai. 2012. Autophagy is a cell death mechanism in Toxoplasma gondii. *Cellular microbiology*. 14:589-607.

Glater, E.E., L.J. Megeath, R.S. Stowers, and T.L. Schwarz. 2006. Axonal transport of mitochondria requires milton to recruit kinesin heavy chain and is light chain independent. *The Journal of cell biology*. 173:545-557.

Gomes, L.C., G. Di Benedetto, and L. Scorrano. 2011. During autophagy mitochondria elongate, are spared from degradation and sustain cell viability. *Nature cell biology*. 13:589-598.

Greene, J.C., A.J. Whitworth, I. Kuo, L.A. Andrews, M.B. Feany, and L.J. Pallanck. 2003. Mitochondrial pathology and apoptotic muscle degeneration in Drosophila parkin mutants. *Proceedings of the National Academy of Sciences of the United States of America*. 100:4078-4083.

Guo, X., G.T. Macleod, A. Wellington, F. Hu, S. Panchumarthi, M. Schoenfield, L. Marin, M.P. Charlton, H.L. Atwood, and K.E. Zinsmaier. 2005. The GTPase dMiro is required for axonal transport of mitochondria to Drosophila synapses. *Neuron*. 47:379-393.

Hara, T., K. Nakamura, M. Matsui, A. Yamamoto, Y. Nakahara, R. Suzuki-Migishima, M. Yokoyama, K. Mishima, I. Saito, H. Okano, and N. Mizushima. 2006. Suppression of basal autophagy in neural cells causes neurodegenerative disease in mice. *Nature*. 441:885-889.

Henchcliffe, C., and M.F. Beal. 2008. Mitochondrial biology and oxidative stress in Parkinson disease pathogenesis. *Nature clinical practice. Neurology*. 4:600-609.

Hirokawa, N., S. Niwa, and Y. Tanaka. 2010. Molecular motors in neurons: transport mechanisms and roles in brain function, development, and disease. *Neuron*. 68:610-638.

Hollenbeck, P.J. 1996. The pattern and mechanism of mitochondrial transport in axons. *Frontiers in bioscience : a journal and virtual library*. 1:d91-102.

Hollenbeck, P.J. 1993. Products of endocytosis and autophagy are retrieved from axons by regulated retrograde organelle transport. *The Journal of cell biology*. 121:305-315.

Hollenbeck, P.J., and W.M. Saxton. 2005. The axonal transport of mitochondria. *Journal of cell science*. 118:5411-5419.

James, D.I., P.A. Parone, Y. Mattenberger, and J.C. Martinou. 2003. hFis1, a novel component of the mammalian mitochondrial fission machinery. *J Biol Chem*. 278:36373-36379.

Jin, S.M., M. Lazarou, C. Wang, L.A. Kane, D.P. Narendra, and R.J. Youle. 2010. Mitochondrial membrane potential regulates PINK1 import and proteolytic destabilization by PARL. *The Journal of cell biology*. 191:933-942.

Kang, J.S., J.H. Tian, P.Y. Pan, P. Zald, C. Li, C. Deng, and Z.H. Sheng. 2008. Docking of axonal mitochondria by syntaphilin controls their mobility and affects short-term facilitation. *Cell*. 132:137-148.

Kiryu-Seo, S., N. Ohno, G.J. Kidd, H. Komuro, and B.D. Trapp. 2010. Demyelination increases axonal stationary mitochondrial size and the speed of axonal mitochondrial transport. *The Journal of neuroscience : the official journal of the Society for Neuroscience*. 30:6658-6666.

Larsen, K.E., and D. Sulzer. 2002. Autophagy in neurons: a review. *Histology and histopathology*. 17:897-908.

Lazarou, M., D.A. Sliter, L.A. Kane, S.A. Sarraf, C. Wang, J.L. Burman, D.P. Sideris, A.I. Fogel, and R.J. Youle. 2015. The ubiquitin kinase PINK1 recruits autophagy receptors to induce mitophagy. *Nature*. 524:309-314.

Lee, S., Y. Sato, and R.A. Nixon. 2011. Lysosomal proteolysis inhibition selectively disrupts axonal transport of degradative organelles and causes an Alzheimer's-like axonal dystrophy. *The Journal of neuroscience : the official journal of the Society for Neuroscience*. 31:7817-7830.

Lionaki, E., M. Markaki, K. Palikaras, and N. Tavernarakis. 2015. Mitochondria, autophagy and age-associated neurodegenerative diseases: New insights into a complex interplay. *Biochimica et biophysica acta*. 1847:1412-1423.

Liu, S., T. Sawada, S. Lee, W. Yu, G. Silverio, P. Alapatt, I. Millan, A. Shen, W. Saxton, T. Kanao, R. Takahashi, N. Hattori, Y. Imai, and B. Lu. 2012. Parkinson's disease-associated kinase PINK1 regulates Miro protein level and axonal transport of mitochondria. *PLoS genetics*. 8:e1002537.

Louie, K., G.J. Russo, D.B. Salkoff, A. Wellington, and K.E. Zinsmaier. 2008. Effects of imaging conditions on mitochondrial transport and length in larval motor axons of Drosophila. *Comparative biochemistry and physiology. Part A, Molecular & integrative physiology*. 151:159-172.

Macaskill, A.F., J.E. Rinholm, A.E. Twelvetrees, I.L. Arancibia-Carcamo, J. Muir, A. Fransson, P. Aspenstrom, D. Attwell, and J.T. Kittler. 2009. Miro1 is a calcium sensor for glutamate receptor-dependent localization of mitochondria at synapses. *Neuron*. 61:541-555.

Maday, S., and E.L. Holzbaur. 2014. Autophagosome biogenesis in primary neurons follows an ordered and spatially regulated pathway. *Developmental cell*. 30:71-85.

Maday, S., K.E. Wallace, and E.L. Holzbaur. 2012. Autophagosomes initiate distally and mature during transport toward the cell soma in primary neurons. *The Journal of cell biology*. 196:407-417.

Martinez-Vicente, M., Z. Talloczy, E. Wong, G. Tang, H. Koga, S. Kaushik, R. de Vries, E. Arias, S. Harris, D. Sulzer, and A.M. Cuervo. 2010. Cargo recognition failure is responsible for inefficient autophagy in Huntington's disease. *Nature neuroscience*. 13:567-576.

Matsuda, N., S. Sato, K. Shiba, K. Okatsu, K. Saisho, C.A. Gautier, Y.S. Sou, S. Saiki, S. Kawajiri, F. Sato, M. Kimura, M. Komatsu, N. Hattori, and K. Tanaka. 2010. PINK1 stabilized by mitochondrial depolarization recruits Parkin to damaged mitochondria and activates latent Parkin for mitophagy. *The Journal of cell biology*. 189:211-221.

McLelland, G.L., V. Soubannier, C.X. Chen, H.M. McBride, and E.A. Fon. 2014. Parkin and PINK1 function in a vesicular trafficking pathway regulating mitochondrial quality control. *The EMBO journal*. 33:282-295.

Miller, K.E., and M.P. Sheetz. 2004. Axonal mitochondrial transport and potential are correlated. *Journal of cell science*. 117:2791-2804.

Misko, A., S. Jiang, I. Wegorzewska, J. Milbrandt, and R.H. Baloh. 2010. Mitofusin 2 is necessary for transport of axonal mitochondria and interacts with the Miro/Milton complex. *The Journal of neuroscience : the official journal of the Society for Neuroscience*. 30:4232-4240.

Mizushima, N., B. Levine, A.M. Cuervo, and D.J. Klionsky. 2008. Autophagy fights disease through cellular self-digestion. *Nature*. 451:1069-1075.

Morris, R.L., and P.J. Hollenbeck. 1995. Axonal transport of mitochondria along microtubules and F-actin in living vertebrate neurons. *The Journal of cell biology*. 131:1315-1326.

Morris, R.L., and P.J. Hollenbeck. 1993. The regulation of bidirectional mitochondrial transport is coordinated with axonal outgrowth. *Journal of cell science*. 104 (Pt 3):917-927.

Mortiboys, H., K.J. Thomas, W.J. Koopman, S. Klaffke, P. Abou-Sleiman, S. Olpin, N.W. Wood, P.H. Willems, J.A. Smeitink, M.R. Cookson, and O. Bandmann. 2008. Mitochondrial function and morphology are impaired in parkin-mutant fibroblasts. *Annals of neurology*. 64:555-565.

Narendra, D., A. Tanaka, D.F. Suen, and R.J. Youle. 2008. Parkin is recruited selectively to impaired mitochondria and promotes their autophagy. *The Journal of cell biology*. 183:795-803.

Narendra, D.P., S.M. Jin, A. Tanaka, D.F. Suen, C.A. Gautier, J. Shen, M.R. Cookson, and R.J. Youle. 2010. PINK1 is selectively stabilized on impaired mitochondria to activate Parkin. *PLoS biology*. 8:e1000298.

Nascimento, A.A., J.T. Roland, and V.I. Gelfand. 2003. Pigment cells: a model for the study of organelle transport. *Annual review of cell and developmental biology*. 19:469-491.

Nicholls, D.G., and S.L. Budd. 2000. Mitochondria and neuronal survival. *Physiological reviews*. 80:315-360.

Ohno, N., G.J. Kidd, D. Mahad, S. Kiryu-Seo, A. Avishai, H. Komuro, and B.D. Trapp. 2011. Myelination and axonal electrical activity modulate the distribution and motility of mitochondria at CNS nodes of Ranvier. *The Journal of neuroscience : the official journal of the Society for Neuroscience*. 31:7249-7258.

Okamoto, K., and J.M. Shaw. 2005. Mitochondrial morphology and dynamics in yeast and multicellular eukaryotes. *Annual review of genetics*. 39:503-536.

Palacino, J.J., D. Sagi, M.S. Goldberg, S. Krauss, C. Motz, M. Wacker, J. Klose, and J. Shen. 2004. Mitochondrial dysfunction and oxidative damage in parkin-deficient mice. *J Biol Chem*. 279:18614-18622.

Park, J., S.B. Lee, S. Lee, Y. Kim, S. Song, S. Kim, E. Bae, J. Kim, M. Shong, J.M. Kim, and J. Chung. 2006. Mitochondrial dysfunction in Drosophila PINK1 mutants is complemented by parkin. *Nature*. 441:1157-1161.

Park, J.J., H. Koshimizu, and Y.P. Loh. 2009. Biogenesis and transport of secretory granules to release site in neuroendocrine cells. *Journal of molecular neuroscience : MN*. 37:151-159.

Pathak, D., K.J. Sepp, and P.J. Hollenbeck. 2010. Evidence that myosin activity opposes microtubule-based axonal transport of mitochondria. *The Journal of neuroscience : the official journal of the Society for Neuroscience*. 30:8984-8992.

Pickford, F., E. Masliah, M. Britschgi, K. Lucin, R. Narasimhan, P.A. Jaeger, S. Small, B. Spencer, E. Rockenstein, B. Levine, and T. Wyss-Coray. 2008. The autophagy-related protein beclin 1 shows reduced expression in early Alzheimer disease and regulates amyloid beta accumulation in mice. *The Journal of clinical investigation*. 118:2190-2199.

Pilling, A.D., D. Horiuchi, C.M. Lively, and W.M. Saxton. 2006. Kinesin-1 and Dynein are the primary motors for fast transport of mitochondria in Drosophila motor axons. *Molecular biology of the cell*. 17:2057-2068.

Pitts, K.R., Y. Yoon, E.W. Krueger, and M.A. McNiven. 1999. The dynamin-like protein DLP1 is essential for normal distribution and morphology of the endoplasmic reticulum and mitochondria in mammalian cells. *Molecular biology of the cell*. 10:4403-4417.

Poole, A.C., R.E. Thomas, L.A. Andrews, H.M. McBride, A.J. Whitworth, and L.J. Pallanck. 2008. The PINK1/Parkin pathway regulates mitochondrial morphology. *Proceedings of the National Academy of Sciences of the United States of America*. 105:1638-1643.

Poole, A.C., R.E. Thomas, S. Yu, E.S. Vincow, and L. Pallanck. 2010. The mitochondrial fusion-promoting factor mitofusin is a substrate of the PINK1/parkin pathway. *PloS one*. 5:e10054.

Raiborg, C., E.M. Wenzel, N.M. Pedersen, H. Olsvik, K.O. Schink, S.W. Schultz, M. Vietri, V. Nisi, C. Bucci, A. Brech, T. Johansen, and H. Stenmark. 2015. Repeated ER-endosome contacts promote endosome translocation and neurite outgrowth. *Nature*. 520:234-238.

Rambold, A.S., B. Kostelecky, N. Elia, and J. Lippincott-Schwartz. 2011. Tubular network formation protects mitochondria from autophagosomal degradation during nutrient starvation. *Proceedings of the National Academy of Sciences of the United States of America*. 108:10190-10195.

Ravikumar, B., C. Vacher, Z. Berger, J.E. Davies, S. Luo, L.G. Oroz, F. Scaravilli, D.F. Easton, R. Duden, C.J. O'Kane, and D.C. Rubinsztein. 2004. Inhibition of mTOR induces autophagy and reduces toxicity of polyglutamine expansions in fly and mouse models of Huntington disease. *Nature genetics*. 36:585-595.

Reis, K., A. Fransson, and P. Aspenstrom. 2009. The Miro GTPases: at the heart of the mitochondrial transport machinery. *FEBS letters*. 583:1391-1398.

Rogers, S.L., and V.I. Gelfand. 1998. Myosin cooperates with microtubule motors during organelle transport in melanophores. *Current biology : CB*. 8:161-164.

Rowland, A.A., P.J. Chitwood, M.J. Phillips, and G.K. Voeltz. 2014. ER contact sites define the position and timing of endosome fission. *Cell*. 159:1027-1041.

Rowland, A.A., and G.K. Voeltz. 2012. Endoplasmic reticulum-mitochondria contacts: function of the junction. *Nature reviews. Molecular cell biology*. 13:607-625.

Rugarli, E.I., and T. Langer. 2012. Mitochondrial quality control: a matter of life and death for neurons. *The EMBO journal*. 31:1336-1349.

Rui, Y., P. Tiwari, Z. Xie, and J.Q. Zheng. 2006. Acute impairment of mitochondrial trafficking by beta-amyloid peptides in hippocampal neurons. *The Journal of neuroscience : the official journal of the Society for Neuroscience*. 26:10480-10487.

Russo, G.J., K. Louie, A. Wellington, G.T. Macleod, F. Hu, S. Panchumarthi, and K.E. Zinsmaier. 2009. Drosophila Miro is required for both anterograde and retrograde axonal mitochondrial transport. *The Journal of neuroscience : the official journal of the Society for Neuroscience*. 29:5443-5455.

Safiulina, D., and A. Kaasik. 2013. Energetic and dynamic: how mitochondria meet neuronal energy demands. *PLoS biology*. 11:e1001755.

Sarkar, S., and D.C. Rubinsztein. 2008. Huntington's disease: degradation of mutant huntingtin by autophagy. *The FEBS journal*. 275:4263-4270.

Sasaki, S., and M. Iwata. 1996. Impairment of fast axonal transport in the proximal axons of anterior horn neurons in amyotrophic lateral sclerosis. *Neurology*. 47:535-540.

Saxton, W.M., and P.J. Hollenbeck. 2012. The axonal transport of mitochondria. *Journal of cell science*. 125:2095-2104.

Sheng, Z.H., and Q. Cai. 2012. Mitochondrial transport in neurons: impact on synaptic homeostasis and neurodegeneration. *Nature reviews. Neuroscience*. 13:77-93.

Shi, P., A.L. Strom, J. Gal, and H. Zhu. 2010. Effects of ALS-related SOD1 mutants on dynein- and KIF5-mediated retrograde and anterograde axonal transport. *Biochimica et biophysica acta*. 1802:707-716.

Shidara, Y., and P.J. Hollenbeck. 2010. Defects in mitochondrial axonal transport and membrane potential without increased reactive oxygen species production in a Drosophila model of Friedreich ataxia. *The Journal of neuroscience : the official journal of the Society for Neuroscience*. 30:11369-11378.

Slater, E.C. 1973. The mechanism of action of the respiratory inhibitor, antimycin. *Biochimica et biophysica acta*. 301:129-154.

Smirnova, E., L. Griparic, D.L. Shurland, and A.M. van der Bliek. 2001. Dynamin-related protein Drp1 is required for mitochondrial division in mammalian cells. *Molecular biology of the cell*. 12:2245-2256.

Song, Z., M. Ghochani, J.M. McCaffery, T.G. Frey, and D.C. Chan. 2009. Mitofusins and OPA1 mediate sequential steps in mitochondrial membrane fusion. *Molecular biology of the cell*. 20:3525-3532.

Soubannier, V., G.L. McLelland, R. Zunino, E. Braschi, P. Rippstein, E.A. Fon, and H.M. McBride. 2012. A vesicular transport pathway shuttles cargo from mitochondria to lysosomes. *Current biology : CB*. 22:135-141.

Stokin, G.B., C. Lillo, T.L. Falzone, R.G. Brusch, E. Rockenstein, S.L. Mount, R. Raman, P. Davies, E. Masliah, D.S. Williams, and L.S. Goldstein. 2005. Axonopathy and transport deficits early in the pathogenesis of Alzheimer's disease. *Science*. 307:1282-1288.

Stowers, R.S., L.J. Megeath, J. Gorska-Andrzejak, I.A. Meinertzhagen, and T.L. Schwarz. 2002. Axonal transport of mitochondria to synapses depends on milton, a novel Drosophila protein. *Neuron*. 36:1063-1077.

Strappazzon, F., F. Nazio, M. Corrado, V. Cianfanelli, A. Romagnoli, G.M. Fimia, S. Campello, R. Nardacci, M. Piacentini, M. Campanella, and F. Cecconi. 2015. AMBRA1 is able to induce mitophagy via LC3 binding, regardless of PARKIN and p62/SQSTM1. *Cell death and differentiation*. 22:419-432.

Tsukada, M., and Y. Ohsumi. 1993. Isolation and characterization of autophagy-defective mutants of Saccharomyces cerevisiae. *FEBS letters*. 333:169-174.

Van Humbeeck, C., T. Cornelissen, H. Hofkens, W. Mandemakers, K. Gevaert, B. De Strooper, and W. Vandenberghe. 2011. Parkin interacts with Ambra1 to induce mitophagy. *The Journal of neuroscience : the official journal of the Society for Neuroscience*. 31:10249-10261.

van Spronsen, M., M. Mikhaylova, J. Lipka, M.A. Schlager, D.J. van den Heuvel, M. Kuijpers, P.S. Wulf, N. Keijzer, J. Demmers, L.C. Kapitein, D. Jaarsma, H.C. Gerritsen, A. Akhmanova, and C.C. Hoogenraad. 2013. TRAK/Milton motor-adaptor proteins steer mitochondrial trafficking to axons and dendrites. *Neuron*. 77:485-502.

Verburg, J., and P.J. Hollenbeck. 2008. Mitochondrial membrane potential in axons increases with local nerve growth factor or semaphorin signaling. *The Journal of neuroscience : the official journal of the Society for Neuroscience*. 28:8306-8315.

Verkhratsky, A.J., and O.H. Petersen. 1998. Neuronal calcium stores. *Cell calcium*. 24:333-343.

Verstreken, P., C.V. Ly, K.J. Venken, T.W. Koh, Y. Zhou, and H.J. Bellen. 2005. Synaptic mitochondria are critical for mobilization of reserve pool vesicles at Drosophila neuromuscular junctions. *Neuron*. 47:365-378.

Vossel, K.A., K. Zhang, J. Brodbeck, A.C. Daub, P. Sharma, S. Finkbeiner, B. Cui, and L. Mucke. 2010. Tau reduction prevents Abeta-induced defects in axonal transport. *Science*. 330:198.

Wang, X., and T.L. Schwarz. 2009. The mechanism of Ca2+ -dependent regulation of kinesin-mediated mitochondrial motility. *Cell*. 136:163-174.

Wang, X., B. Su, S.L. Siedlak, P.I. Moreira, H. Fujioka, Y. Wang, G. Casadesus, and X. Zhu. 2008. Amyloid-beta overproduction causes abnormal mitochondrial dynamics via differential modulation of mitochondrial fission/fusion proteins. *Proceedings of the National Academy of Sciences of the United States of America*. 105:19318-19323.

Wang, X., D. Winter, G. Ashrafi, J. Schlehe, Y.L. Wong, D. Selkoe, S. Rice, J. Steen, M.J. LaVoie, and T.L. Schwarz. 2011. PINK1 and Parkin target Miro for phosphorylation and degradation to arrest mitochondrial motility. *Cell*. 147:893-906.

Weihofen, A., K.J. Thomas, B.L. Ostaszewski, M.R. Cookson, and D.J. Selkoe. 2009. Pink1 forms a multiprotein complex with Miro and Milton, linking Pink1 function to mitochondrial trafficking. *Biochemistry*. 48:2045-2052.

Wong, Y.C., and E.L. Holzbaur. 2014a. Optineurin is an autophagy receptor for damaged mitochondria in parkin-mediated mitophagy that is disrupted by an ALS-linked mutation. *Proceedings of the National Academy of Sciences of the United States of America*. 111:E4439-4448.

Wong, Y.C., and E.L. Holzbaur. 2014b. The regulation of autophagosome dynamics by huntingtin and HAP1 is disrupted by expression of mutant huntingtin, leading to defective cargo degradation. *The Journal of neuroscience : the official journal of the Society for Neuroscience*. 34:1293-1305.

Wood-Kaczmar, A., S. Gandhi, Z. Yao, A.Y. Abramov, E.A. Miljan, G. Keen, L. Stanyer, I. Hargreaves, K. Klupsch, E. Deas, J. Downward, L. Mansfield, P. Jat, J. Taylor, S. Heales, M.R. Duchen, D. Latchman, S.J. Tabrizi, and N.W. Wood. 2008. PINK1 is necessary for long term survival and mitochondrial function in human dopaminergic neurons. *PloS one*. 3:e2455.

Xie, Z., and D.J. Klionsky. 2007. Autophagosome formation: core machinery and adaptations. *Nature cell biology*. 9:1102-1109.

Yoon, Y., E.W. Krueger, B.J. Oswald, and M.A. McNiven. 2003. The mitochondrial protein hFis1 regulates mitochondrial fission in mammalian cells through an interaction with the dynamin-like protein DLP1. *Molecular and cellular biology*. 23:5409-5420.

Yu, Y., H.C. Lee, K.C. Chen, J. Suhan, M. Qiu, Q. Ba, and G. Yang. 2016. Inner membrane fusion mediates spatial distribution of axonal mitochondria. *Scientific reports*. 6:18981.

Yue, Z., L. Friedman, M. Komatsu, and K. Tanaka. 2009. The cellular pathways of neuronal autophagy and their implication in neurodegenerative diseases. *Biochimica et biophysica acta*. 1793:1496-1507.

Ziviani, E., R.N. Tao, and A.J. Whitworth. 2010. Drosophila parkin requires PINK1 for mitochondrial translocation and ubiquitinates mitofusin. *Proceedings of the National Academy of Sciences of the United States of America*. 107:5018-5023.

Zuchner, S., I.V. Mersiyanova, M. Muglia, N. Bissar-Tadmouri, J. Rochelle, E.L. Dadali, M. Zappia, E. Nelis, A. Patitucci, J. Senderek, Y. Parman, O. Evgrafov, P.D. Jonghe, Y. Takahashi, S. Tsuji, M.A. Pericak-Vance, A. Quattrone, E. Battaloglu, A.V. Polyakov, V. Timmerman, J.M. Schroder, and J.M. Vance. 2004. Mutations in the mitochondrial GTPase mitofusin 2 cause Charcot-Marie-Tooth neuropathy type 2A. *Nature genetics*. 36:449-451.

VITA

VITA

Hyun Sung

Graduate School, Purdue University

Education

May 2015	Ph.D. Department of Biological Science, Puedue University, IN, USA
February 2010	M.S. Department of Life Sciences, Hanyang University, Seoul, Korea
February 2008	B.S. Department of Life Sciences, Hanynag University, Seoul, Korea

Research Experience

Aug. 2010 - May 2015	Peter Hollenbeck's Laboratory (Purdue Univ.) : Axonal transport of mitochondria in *Drosophila* neurons
Mar. 2008 - Jul. 2010	Developmental Genetics Laboratory (Supervised by Dr. Joohong Ahnn, Hanyang Univ.) : Role of ESCRT protein in intracellular trafficking : Study of a calcium-binding protein in *C. elegans* : Genetic analysis of bacterial preference in *C. elegans*
Mar. 2007 - Feb. 2008	Endocrine system Laboratory (Supervised by Dr. Yongdal Yoon, Hanyang Univ.)

Teaching Experience

Fall / 2014 & 2015	Teaching Assistant for BIOL231, Purdue Univ. : Cell Structure and Function
Spring / 2014 & 2015	Teaching Assistant for BIOL241, Purdue Univ. : Introduction to Genetics and Molecular Biology
Mar. 2008 - Jun. 2009	Teaching Assistant for General Biology, Hanynag Univ. : General Biology & Experiment